

ADDITIVE MANUFACTURING OF GRAPHENE-BASED DEVICES FOR
FLEXIBLE HYBRID ELECTRONICS

by

Twinkle Pandhi



A dissertation

submitted in partial fulfillment

of the requirements for the degree of

Doctor of Philosophy in Materials Science and Engineering

Boise State University

December 2020

© 2020

Twinkle Pandhi

ALL RIGHTS RESERVED

BOISE STATE UNIVERSITY GRADUATE COLLEGE

DEFENSE COMMITTEE AND FINAL READING APPROVALS

of the dissertation submitted by

Twinkle Pandhi

Dissertation Title: Additive Manufacturing of Graphene-Based Devices for Flexible Hybrid Electronics

Date of Final Oral Examination: 30 October 2020

The following individuals read and discussed the dissertation submitted by student Twinkle Pandhi, and they evaluated their presentation and response to questions during the final oral examination. They found that the student passed the final oral examination.

David Estrada, Ph.D.	Chair, Supervisory Committee
Elton Graugnard, Ph.D.	Member, Supervisory Committee
Paul Simmonds, Ph.D.	Member, Supervisory Committee
Jessica E. Koehne, Ph.D.	Member, Supervisory Committee
Emily M. Heckman, Ph.D.	Member, Supervisory Committee

The final reading approval of the dissertation was granted by David Estrada, Ph.D., Chair of the Supervisory Committee. The dissertation was approved by the Graduate College.

DEDICATION

This dissertation is dedicated to my family and friends for their support and motivation over the years.

ACKNOWLEDGMENTS

First, I would like to express my gratitude to my academic advisor Dr. David Estrada for opening this door of opportunity for me at Boise State University. His support and guidance are much appreciated and have enhanced both my career and personal life. I would also like to extend my gratitude towards my committee members, Dr. Elton Graugnard, Dr. Paul Simmonds, Dr. Jessica Koehne, and Dr. Emily Heckman, to accomplish this milestone. I would also like to acknowledge my advisor Dr. Deji Akinwande and Dr. Avinash Nayak from the University of Texas at Austin, who led me to research graphene and Dr. David Estrada's research lab at Boise State University.

I would like to extend my gratitude to Dr. Claire Xiong and Peter Barnes for providing me access to their lab facilities and their help with decoding electrochemistry. Furthermore, Dr. Jessica Koehne, in creating NASA internship opportunities that helped me launch my research project, I very much appreciated it. Also, I sincerely appreciate all the resources and aid provided to us by Dr. Emily Heckman and her Air Force team. I am thankful to Peter Miranda and Travis Gabel for providing ongoing assistance throughout my work. Grateful to the MSE staff for their diligent work with travel, finances, and resources at Boise State, especially Chad Watson, Jessica Economy, Stephanie Moran, Jamie Hayward, Taylor Hartung, and Dr. Will Hughes.

My gratitude extends to Dr. Harish Subbaraman and notable people of the DREAM team. Kiyo Fujimoto and Dr. Tony Varghese for their endless support and motivation to keep moving forward. It was a great pleasure to work with all the people in

the ANML group, namely Dr. Josh Exienberger, Ashita Chandnani, Naqsh Mansoor, Nick Mckibben, Florent Muramutsa, Katie Yocham, Ricarrdo Torsi, Jasmine Cox, Lynn Karriem, Tyler Webb, Fataneh Jenabi, Fereshteh Rajabik, Cardre Francis, Angel Rodriguez, Katelyn Wada, Sarah Seva, Kyle Kramer, Bahareh Badamchi, Jerry Murphy, and Binay Joshi. I would also like to acknowledge my friends from both Boise and Austin group who have always been there for emotional and motivational support. Ann Delaney, one of my first friends at Boise State, genuinely thankful for all your help and support and for lending me your bicycle.

Lastly, I would like to thank my family, especially my mother, Charu Pandhi, who gave me all the world opportunities to be my best. Furthermore, I would like to thank my boyfriend Akash Gulleria for all the support and encouragement to get through ups and downs and being like my second family here in Boise.

ABSTRACT

In this work, I investigate and enhance the fundamental sensing properties of printed electronic nanomaterials (e.g., graphene) in real-world environments while decreasing weight, cost, and power consumption. The dissertation addresses this issue with the following foci in mind: (1) developing a straightforward and repeatable process to synthesize graphene ink which is also compatible with Inkjet-printing (IJP) and Aerosol Jet printing (AJP). (2) Tuning additive manufacturing printing (IJP and AJP) parameters to establish a repeatable manufacturing process and print high performing (graphene-based) electrodes and interconnects, compatible with the underlying substrate. (3) Investigate power dissipation and electrical breakdown in AJP printed graphene interconnects. (4) Investigate the IJP printed graphene electrodes' electrochemical sensitivity with pH and selectivity of Na⁺ ions and K⁺ ions. (5) Integrate printed electrochemical sensors with flexible silicon integrated circuits (Flex-ICs) for flexible hybrid electronics applications. Herein we demonstrate printed devices using graphene to enhance capabilities relative to sensitivity, conformability, and fast and repeatable responsivity while reducing the monitoring devices' mass. Understanding the structure-property-processing correlations of our graphene-based devices has helped us improve consistency, repeatability, and uniformity of the printed systems. This marks a significant step forward for designing flexible hybrid sensors as a platform to fabricate sensors for space, military, and commercial applications.

TABLE OF CONTENTS

DEDICATION	iv
ACKNOWLEDGMENTS	v
ABSTRACT	vii
LIST OF TABLES	xii
LIST OF FIGURES	xiii
LIST OF ABBREVIATIONS	xix
CHAPTER ONE: INTRODUCTION	1
1.1 Motivation.....	1
1.2 Graphene	2
1.3 Preparation of Graphene Ink.....	5
1.4 Inkjet Printing.....	7
1.5 Aerosol-Jet Printing.....	9
1.6 Graphene-Based Sensors	11
1.7 Flexible Hybrid Electronics	12
1.8 Conclusion	13
1.9 Dissertation Outline.....	14
1.10 References.....	15
CHAPTER TWO: A REVIEW OF INKJET PRINTED GRAPHENE AND CNT BASED GAS SENSORS	26
2.1 Abstract.....	27

2.2	Introduction.....	27
2.3	Graphene-Based Gas Sensors	31
2.4	Carbon Nanotubes-Based Gas Sensors.....	37
2.5	Role of Defects.....	46
	2.5.1 Graphene-Based sensors.....	46
	2.5.2 CNT-Based Sensors	48
2.6	Advanced Printing Techniques	50
	2.6.1 Aerosol-Jet Printing.....	50
	2.6.2 Plasma-Jet printing	52
2.7	Outlook	54
2.8	Conclusion	54
2.9	Acknowledgements	55
2.10	References.....	55
CHAPTER THREE: ELECTRICAL TRANSPORT AND POWER DISSIPATION IN AEROSOL-JET-PRINTED GRAPHENE INTERCONNECTS		68
3.1	Abstract.....	69
3.2	Introduction.....	69
3.3	Results and Discussion	72
	3.3.1 Graphene Ink Characterization	72
	3.3.2 Aerosol-Jet Printed Graphene Interconnects	74
	3.3.3 Electrical Scaling in AJP Graphene Interconnects	78
	3.3.4 Power Dissipation of AJP Graphene Interconnects	79
3.4	Discussion	88
3.5	Conclusion	92

3.6	Methods	92
3.6.1	Preparation and Characterization of Graphene Ink	92
3.6.2	SEM, AFM, and TEM Imaging	93
3.6.3	UV-VIS Spectroscopy	93
3.6.4	Thermogravimetric Analysis	94
3.6.5	AJP of Graphene Interconnects	94
3.6.6	Finite Element Model.....	95
3.7	Acknowledgements	95
3.8	Reference	96

CHAPTER FOUR: FULLY INKJET-PRINTED MULTILAYERED GRAPHENE-BASED FLEXIBLE ELECTRODES FOR ELECTROCHEMICAL PERFORMANCE
..... 101

4.1	Abstract.....	102
4.2	Introduction.....	103
4.3	Results and Discussions.....	106
4.3.1	Inkjet Printing of Graphene Electrodes.....	106
4.3.2	Electrochemical Response of MLG Electrodes	109
4.3.3	Stability of MLG Electrodes.....	117
4.3.4	pH Sensitivity of MLG Electrodes.....	120
4.3.5	Fully Printed Three-Electrode Devices	127
4.4	Conclusion	129
4.5	Methods	130
4.5.1	Preparation and Characterization of Graphene Ink.....	130
4.5.2	Thermogravimetric Analysis	131

4.5.3	Fabrication of MLG Electrodes	131
4.5.4	Fabrication of Platinum Inks and Platinum Electrodes	132
4.5.5	Fully IJP Three-Electrode Devices	133
4.5.6	Electrochemical Set-up.....	134
4.6	Acknowledgements	134
4.7	References.....	135
CHAPTER FIVE: FUTURE WORK-INTEGRATION OF GRAPHENE ELECTRODES WITH FLEXIBLE SILICON INTEGRATED CIRCUITS (Flex-ICs) FOR ION SELECTIVITY STUDY.....		144
5.1	Introduction.....	144
5.1.1	Flexible Hybrid Electronics	144
5.1.2	Ion-Selective Electrodes.....	145
5.2	Preliminary Results and Discussion	146
5.2.1	Construction of Ion-Selective Electrodes.....	146
5.3	Conclusion	150
5.4	References.....	150
CHAPTER SIX: SUMMARY		153

LIST OF TABLES

Table 2.1	Printed graphene gas sensors.	32
Table 2.2	Printed carbon nanotube (CNT) gas sensors.....	40
Table 4.1	SSM for Calculating Selectivity Coefficients of MLG sensors (H ⁺ ions against interfering ions)	122
Table 4.2	Comparison of the Ψ (kinetic parameter) of different material- and fabrication-based electrodes.....	124

LIST OF FIGURES

Figure 1.1	Schematic of the graphene crystal structure (a) unit cell (b) bonding (c) K and K' points, (d) band gap, and (e) density of states. ²²	3
Figure 1.2	Schematic of the exfoliation process from graphite to graphene ⁸²	6
Figure 1.3	Schematic of inkjet printing ⁹⁸	8
Figure 1.4	Schematic of aerosol jet printing ¹¹⁵	10
Figure 1.5	American Semiconductors Flex-ICs ¹²⁴	12
Figure 1.6	Optical image of a flexible hybrid sensor ¹²⁹	13
Figure 2.1	Flexisense, inkjet-printed graphene oxide and reduced graphene oxide for gas and vapor concentration detection [38]. (a) All-organic rGO-based flexible chemiresistor; (b) Resistance change versus time plot when the sensor was exposed to Cl ₂ vapor; (c) Change in resistance with exposed to other vapor; Reproduced with permission from John Wiley and Sons	33
Figure 2.2	(a) Inkjet-printed graphene oxide on LOVE wave device. (b–d) Ethanol (C ₂ H ₆ O), toluene (C ₇ H ₈) and H ₂ O responses respectively, of different sensing layers (GO, ZnO film/ZnO nanorods and PVP) [72]. Reproduced with permission from IEEE.	34
Figure 2.3	Flexible inkjet-printed GO/ PEDOT:PSS composite-based gas sensor for NH ₃ detection [84]. Reproduced with permission from Elsevier.....	36
Figure 2.4	(a) Flexible gas sensor, with inkjet-printed reduced graphene oxide (rGO) and silver (Ag) electrodes on treated Kapton. (b,c) Relative sensitivity response to DMMP and DEEP in N ₂ gas at room temperature [86,87]. Reproduced with permission from Spring Nature and Royal Society of Chemistry.....	37

Figure 2.5	<p>Raman shifts before (“a”, black) and after (“b”, red) exposure to 100 ppm Cl₂ vapor for (a) inkjet-printed CNT/PET, where the shift is partially reversible upon photoirradiation (to “c”, green); (b) inkjet-printed CNT/paper, where the shift is reversible. (c) Selectivity plot for an inkjet-printed CNT/PET film, sensor exposed to saturated organic vapors, NH₃ (100 ppm), NO₂ (100 ppm), and Cl₂ (100 ppm). Reproduced with permission from American Chemical Society [107].</p>	43
Figure 2.6	<p>Fully printed and flexible CNTs based gas sensor: (a) CNTs’ functionalization with carboxylic acid (O-CNTs) and PEDOT:PSS (P-CNTs); (b) printing of Ag electrodes; (c) printing of CNTs; (d) photograph of the sensor on flexible substrate; (e) optical microscope image shows the printed silver interdigitated electrodes and (f) SEM image shows the printed carbon nanotubes. (g) Sensitivity of the printed ethanol vapor sensor (operated at 5V) with different CNTs functionalization methods and different gas concentrations. Reproduced with permission from Elsevier [53].</p>	45
Figure 2.7	<p>(a) Measurement setup for paper-based sensors with silver and inkjet-printed SWNT-PABS. (b) Resistance of paper-based sensor exposed to different concentrations of NH₃. Reproduced with permission from Elsevier [54].</p>	45
Figure 2.8	<p>(a) Conductance (S) vs. filtration volume (mL) for the randomly stacked graphene flakes. (b) Normalized resistance vs. temperature (K) for various filtration volumes from 3 to 10 mL [18]. Reproduced with permission from AIP Publishing.</p>	48
Figure 2.9	<p>(a) Sensing mechanism in CNTs. Reproduced with permission from American Chemical Society [42]. (b) Calculations of the effects of changes in the components of the resistance on the overall resistance of the networks for perfect nanotubes and (c) defective nanotubes. Reproduced with permission from American Chemical Society [44]. (d) Detrapping mechanism of accumulated charges at the nanotube defects in PF regime. Reproduced with permission from AIP Publishing [131] (e) Clustering of acetone around the defect via intermolecular bonding. (f) Charge transfer between various analytes and the SWNT network as a function of oxidation. Reproduced with permission from American Chemical Society [132].</p>	49
Figure 2.10	<p>(a) Schematic of the atmospheric plasma jet. Photographs of aerosol flow with (b) no plasma and (c) plasma on. (d) MWCNTs on paper as a gas sensor exposed to ammonia in the range of 10–60 ppm. Reproduced with permission from AIP Publishing [106].</p>	53

Figure 3.1	Graphene ink characterization (a) optical image of solvent exfoliated graphene/ethyl cellulose (EC)paper and AJP compatible graphene ink solution (b) UV-Visible absorption spectra is employed for quantifying the graphene flake concentration using the Lambert-Beer Law. Typical Raman spectra is seen (inset) for graphene/EC flakes on SiO ₂ (c) TEM images and diffraction pattern of graphene flakes: to extract and compare lateral crystal dimensions we observed and calculated using Raman spectra and Cancado's equation.73
Figure 3.2	To characterize the graphene flakes, diluted graphene ink was drop-casted and annealed (at 100°C for 10 min) on Si/SiO ₂ wafer. (a) AFM scan of the dispersed graphene flakes was used to obtain particle statistics. Histogram of (b) flake thickness was extrapolated by using ImageJ.74
Figure 3.3	Investigating power dissipation of printed graphene interconnects with a combination of electrical breakdown and IR imaging. (a) Schematic of TLM experimental test structures of AJP graphene interconnects (increasing number of passes n=5 to n=50) with silver contact pads on Si/SiO ₂ (b,c) SEM images of the AJP printed/annealed graphene interconnects and a magnified SEM image to show the uniformity of the printed graphene.76
Figure 3.4	a) Height profile of the graphene interconnect on Si/SiO ₂ is seen as a function of increasing number of print passes n=5 to n=50, shows a uniform deposition rate. (b) Full-width-half-max (FWHM) and peak height data extracted from the height profile provides additional support for the height correlation. (c) The electrical conductance of the graphene interconnects on Si/SiO ₂ , for n=50 pass line, with increasing length (L1=200µm to L5=1000µm). (d) Temperature-dependent measurements: normalized resistance inversely proportional to temperature.77
Figure 3.5	Stylus profilometry was used to extract height profile of the graphene interconnect was monitored as a function of increasing number of print passes on Kapton TM (a, c) and on Al ₂ O ₃ (b, d)78
Figure 3.6	Conductance of the graphene interconnect was monitored as a function of increasing number of print passes on Kapton TM (a) and on Al ₂ O ₃ (b)79
Figure 3.7	Power Dissipation investigation of AJP graphene interconnects: Infrared (IR) thermal images of printed graphene interconnects with n = 20 print passes. (a) Kapton TM , (b) SiO ₂ , and (c) Al ₂ O ₃ (d - f) COMSOL simulation IR images to support the correlating experimental IR images seen above. The temperature scale bar is identical for both experimental and simulated results (g - i) Current vs. Voltage characteristics of AJP printed graphene interconnects on various substrates to extract power breakdown values. .81

Figure 3.8	Current vs. Voltage characteristics of AJP graphene interconnects on various substrates where a-b) breakdown of Kapton TM , c-d) Al ₂ O ₃ , and e-f) breakdown of Si/SiO ₂	83
Figure 3.9	TGA (Netzsch instrument, at a heating rate of 5°C/min in the air) of the dried graphene flakes (black), showing mass as a function of temperature and (blue) the differential mass loss. The decomposition peak of surfactant, ethylcellulose, is around 250°C, and oxidation/decomposition of the graphene around 550°C	85
Figure 3.10	Investigating porosity and breakdown of the printed graphene interconnects: (a-b) and (c-d) Cross-section TEM images of the printed graphene interconnects on Si/SiO ₂ for n=50 and (e and f) SEM images of different breakdown patterns of the printed graphene interconnects on Si/SiO ₂	88
Figure 3.11	SEM images of the printed graphene interconnects on Al ₂ O ₃ (a) and the corresponding breakdown image (b). Similarly, printed graphene interconnect SEM on Kapton TM (c) and the corresponding breakdown image (d).....	91
Figure 3.12	Optical images of an AJP graphene interconnect on Kapton TM (a) and a similar device after breakdown (b).....	91
Figure 4.1	Inkjet-printed graphene layer characterization. a) Optical image of inkjet-printed graphene (15-30 printed passes) structure on the glass. b) SEM image of the 25-pass printed line (left) and TEM image of the multilayer graphene flakes (right) on Kapton HN. c) TGA and DSC data of the graphene/ethylcellulose ink. d) Sheet resistance vs. temperature for 15 to 30 printed passes on the glass. e) Typical Raman spectra (532 nm excitation) for 15 to 30 printed passes MLG films.	108
Figure 4.2	a) Sketch of the Dimatix inkjet printer printing graphene on Kapton. b) Design and layers of the graphene electrode. c) Contact angle measurements of graphene ink on Kapton. d) Optical image of the printed graphene electrode, where the yellow ring indicates the surface area of the electrode exposed to the electrolyte. e) Photograph of the electrochemical experimental setup of the graphene electrode in aqueous ferricyanide redox couple with Ag/AgCl as the reference electrode and platinum wire as the counter electrode.	110

Figure 4.3	Graphene electrode cyclic voltammetry (CV) scan rate data for 1 mM $[\text{Fe}(\text{CN})_6]^{-3/4}$ in 1M KCl as the supporting electrolyte with increasing scan rate 10mV/s-100mV/s for a) 25 printed passes of graphene and b) 30 printed passes of graphene. E-labs CV-Sim fitted data for c) 25 printed passes of graphene and d) 30 printed passes of graphene. Cross-section TEM images of e) 25 printed passes graphene and f) 30 printed passes graphene.....	111
Figure 4.4	(a) 15 printed passes and (b) 20 printed passes cyclic voltammetry (CV) scans for 5 mM $[\text{Fe}(\text{CN})_6]^{-3/4}$ in 1 M KCl as the supporting electrolyte with increasing scan rate from 10 to 100 mV/s.....	112
Figure 4.5	Extracted peak current (I_p) versus square root of scan rate (V/s) ^{1/2} data from the CV measurements of (a) 25 printed passes and (b) 30 printed passes.	113
Figure 4.6	AFM scanned image of a) MLG 30 printed passes on Kapton and b) 25 printed passes on Kapton	113
Figure 4.7	Graphene electrode cyclic voltammetry (CV) scan rate data for 1 mM $\text{C}_{11}\text{H}_{12}\text{FeO}$ in 1M KCl as the supporting electrolyte with increasing scan rate 10mV/s-100mV/s for 25 printed passes of graphene.	116
Figure 4.8	Graphene electrode CV dilution data for 1 mM - 5 mM $[\text{Fe}(\text{CN})_6]^{-3/4}$ in 1M KCl as the supporting electrolyte for 25 printed passes at scan rates of a) 10mV/s, b) 50mV/s, and c) 100mV/s. d)-f) are corresponding data for 30 printed passes, with scan rates of d) 10mV/s, e) 50mV/s, and f) 100mV/s.....	118
Figure 4.9	a) Time-dependent CV scans for 25 IJP printed passes, 1mM $\text{K}_3\text{Fe}(\text{CN})_6$ in 1 M KCl as the supporting electrolyte at a scan rate of 100mV/s. b) CV repeatability data for 25 IJP printed passes (3 graphene electrodes), 1 mM dilution $[\text{Fe}(\text{CN})_6]^{-3/4}$ in 1 M KCl as the supporting electrolyte at a scan rate of 10 mV/s. c) CV dilution data showing peak current (I_{pca}) vs. concentration from 5 mM to 0.01 mM of $[\text{Fe}(\text{CN})_6]^{-3/4}$ in 1 M KCl as the supporting electrolyte for 25 IJP printed passes, one graphene electrode at scan rate from 10mV/s. d) Static linear pH data vs. potential (potassium phosphate monobasic with sodium hydroxide commercial pH buffer solutions: 4-10 pH) using the 25 passes graphene printed electrode. Error bars represents the interelectrode standard variation in slope compared to the theoretical values based on the Nernst equation. ⁹⁴⁻⁹⁶ e) Time vs. potential data with changing pH from 2 to 10 for a single 25 printed passes graphene electrode. The error bar represents the standard deviation of potential across three independent samples. f) Bending cycles (1, 10, 100, and 1000) conducted on the electrodes with radius of curvature either 7.5 mm (orange) or 14.5 mm (black) vs. peak to peak separation potential.	119

Figure 4.10	Static linear pH data vs. potential (potassium phosphate monobasic with sodium hydroxide commercial pH buffer solutions: 1-10 pH) using the 3 identical 25 passes graphene printed electrodes.....	121
Figure 4.11	a) TEM image of the platinum nanoparticles (PtNP) with an optical image of the platinum ink (inset) b) Resistivity vs. temperature for 4 printed passes of platinum lines on Kapton (inset). c) Optical image of IJP all three electrodes (Ag/AgCl as the reference electrode, platinum as the counter electrode, and MLG as the working electrode). d) optical picture of the electrochemical setup for the fully printed three electrode sensors. e) Cyclic voltammetry (CV) data of IJP MLG (black) compared to all three electrodes (orange) in 1 mM $[\text{Fe}(\text{CN})_6]^{-3/4}$ and 1 M KCl as the supporting electrolyte with scan rate 10mV/s and f) CV scans of all three printed electrodes with increasing scan rate from 10 mV/s-100 mV/s.	128
Figure 5.1	Direct Bonding Process	145
Figure 5.2	Potentiometric Response a) Potential response with varying NaCl concentration and b) timed response of ISM on graphene electrodes.....	148
Figure 5.3	Example of Flex ICs with IJP silver interconnects ²³	149

LIST OF ABBREVIATIONS

Equations/Units

cP	Centipoise
T	Temperature
GPa	Giga Pascals
P	Power
R	Resistance
I	Current
V	Voltage
FWHM	Full Width Half Max
RPM	Rotations Per Minute
TLM	Transmission Line Method
VRH	Variable range hopping
°C	Degree Celsius
Ψ	Dimensionless Kinetic Parameter
Δ	Change

Tools

CVD	Chemical Vapor Deposition
TGA	Thermal Gravimetric Analysis
SEM	Scanning Electronic Microscopy
TEM	Transmission Electron Microscopy

AFM	Atomic Force Microscopy
U-Vis	Ultraviolet-Visible Spectroscopy
IR	Infrared
CA	Contact angle
CV	Cyclic Voltammetry
OCP	Open circuit potential

Materials

G	Graphene
CNT	Carbon Nanotubes
MoS ₂	Molybdenum Disulfide
h-BN	Hexagonal Boron Nitride
2D	Two dimensional
3D	Three dimensional
SiC	Silicon Carbide
NMP	N-Methyl-2-pyrrolidone
DMF	Dimethylformamide
EC	Ethyl Cellulose
Ag	Silver
Cu	Copper
NaCl	Sodium Chloride
CNF	Carbon nanofiber
GNR	Graphene nanoribbons
MLG	Multi-Layered Graphene

Pt	Platinum
PvP-Ptnp	Polyvinyl pyrrolidone capped Pt nanoparticle
ISE	Ion-selective electrode
ISM	Ion-selective membrane

Techniques

AM	Additive Manufacturing
IJP	Inkjet Printing
AJP	Aerosol Jet Printing
MDP	Micro dispense printing
ACA	Anisotropic conductive adhesives
NCA	Non-conductive adhesive

Applications

IoT	Internet of things
Flex-ICs	Flexible integrated circuits
ASI	American Semiconductors Inc.

CHAPTER ONE: INTRODUCTION

1.1 Motivation

Electronics play an essential role in our lives, from performing multifaceted tasks like driving a car to relatively simple sensing with motion detectors. Such applications have created a high demand for electronics to be low-cost, lightweight, flexible, and stretchable to enable a high degree of integration with the internet of things (IoT). Hence, the market for printed and flexible electronics has seen rapid advancement with the potential to develop into a multi-billion-dollar wearable electronics industry.^{1,2} For example, there is widespread interest in the Department of Defense and space industries for flexible sensors to provide a low-cost solution that can perform measurements for structure analysis and human performance monitoring.³⁻⁵ Health monitoring systems for the vehicle and astronauts are vital to the support of planetary exploration. Currently, the fundamental reasoning limiting such monitoring systems' capabilities is stability, sensitivity, and selectivity. Recently, NASA has developed and launched a zero-gravity 3D printer to the International Space Station (ISS), which transformed the concept of in-space manufacturing.⁶ New components, systems, and subsystems are being developed in space rather than on Earth. By expanding the manufacturing toolset to inkjet or aerosol jet printers, coupled with the development of multifunctional nanomaterial inks, in-space manufacturing can move from a design of structural systems towards the fabrication of circuitry and electronic components on 3D substrates.^{5,6}

One of the main challenges limiting high volume manufacturing of printed and flexible electronics is the lack of high performance and multifunctional inks compatible with existing direct write technologies such as inkjet printing (IJP), aerosol jet printing (AJP), and micro dispense printing (MDP).^{7,8} The emergence of two-dimensional (2D) materials (e.g., graphene, phosphorene, h-BN, and MoS₂) has opened new design spaces for multifunctional inks. These inks can target chemical and biological analytes and monitor state variables such as temperature and pressure.⁹⁻¹² However, much work remains to develop a thorough understanding of such nanomaterial inks' performance in electronic devices and their fundamental interactions with their 3-dimensional (3D) environments. The following chapter introduces graphene, the process of exfoliation, additive manufacturing tools, graphene-based sensors, and flexible hybrid electronics.

1.2 Graphene

In general, 2D materials are one to three atomic layers thick and have modified band structures compared to the material's bulk forms.¹³ This quantum confinement gives rise to unique physical and chemical properties. Graphene, a monolayer of sp² hybridized carbon in a 2-dimensional hexagonal lattice structure (**Figure 1.1a**), has received much attention in the research community due to its unique electrical, mechanical, and chemical properties.^{14,15} The sp² bonding with high binding energy (615 kJ/mol) between the carbon atoms (**Figure 1.1b**) in graphene creates three σ -bonds responsible for its high in-plane mechanical strength and thermal conductivity.¹⁶⁻²⁰ Graphene's high conductivity is associated with overlapping p_z orbitals above and below the molecular plane, which creates a delocalized π – electron system (**Figure 1.1b**) to allow for free movement of

electrons.²¹ These unique bonding characteristics give rise to a linear band structure with a zero-band gap near the K and K'

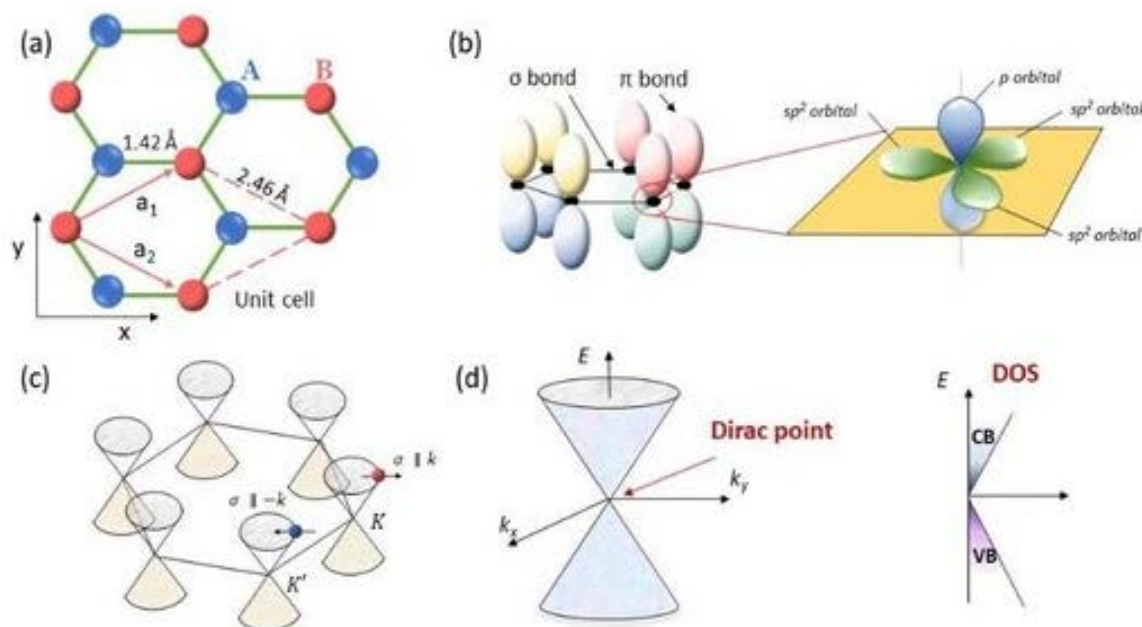


Figure 1.1 Schematic of the graphene crystal structure (a) unit cell (b) bonding (c) K and K' points, (d) band gap, and (e) density of states.²²

points (**Figure 1.1c-d**), leading to graphene's high electrical conductivity ($\sim 10^6$ S/cm).^{10,17} Standard semiconductor theory suggests electrons in graphene have an infinite effective mass due to the linear dispersion relationship (**Figure 1.1e**).²³ However, electrons in graphene actually behave as massless Dirac Fermions with a Fermi velocity of $\sim 10^6$ m/s.²³ This gives graphene a high charge carrier mobility with reported values up to 200,000 cm²/Vs near room temperature (140 times higher than that of silicon), which can be limited by scattering due to defects, impurities, and phonons.^{24,25} Moreover, graphene's mobility can be tuned by electrical and chemical doping.²⁶⁻²⁸

Graphene is known to have high thermal conductivity (~ 3000 Wm⁻¹K⁻¹)²⁹, making it a desirable material for high temperature and high power applications such as

temperature sensors or heat spreaders.^{29–31} Nevertheless, the overall performance of graphene devices can be limited by power dissipation.^{30,32,33} Effects of Joule heating are influenced by device structure, thermal transport across material interfaces, and the substrate material.^{30,34–36} Several studies have examined the impact of Joule heating in graphene devices fabricated using graphene obtained by various synthesis techniques such as mechanical exfoliation, epitaxial growth on silicon carbide (SiC), and CVD growth on transition metal substrates.^{29–32,34,37–39} While these are widely used synthesis techniques; they are known to introduce defects to the graphene structure detrimental to electrical and thermal transport properties.^{20,40–46}

The spacing between each pair of carbon atom is about 1.42 Å and linked through strong intra-layer covalent bonds responsible for pristine graphene with high mechanical strength (Young's modulus of 1100 *GPa*).⁴⁷ Pristine monolayer of graphene is known to be the strongest material (stronger than Diamond), which has been studied on freestanding graphene by nanoindentation of the surface using an Atomic Force Microscopy (AFM) tip.⁴⁷ In contrast, the forces between different graphene layers are van der Waals with a spacing in the order of 3.35 Å. Bulk graphite, which is the most common allotrope of carbon, consists of thousands of interconnected layers of graphene with low binding energy and can be separated by applying small forces (i.e., mechanical exfoliation of graphene using a scotch tape).¹⁵ Consequently, the isolation of a single sheet of graphene can be easily achieved through exfoliation techniques.

To understand the phonon dispersion of the graphene is essential to interpret the Raman spectra of graphene.^{48,49,50} Raman spectroscopy is a useful tool for observing and understanding the atomic in-plane or out-of-plane vibrations present with varying layers

and quality of graphene.⁵¹ The prominent features in the Raman spectra of monolayer graphene are G-band (graphite), D-band (disorder and defects), and 2D-band (two-dimensionality). The increased impurity and defect density due to the environment or the fabrication/transfer process can influence phonon scattering which appears as unique features in the Raman spectrum of graphene.

Moreover, graphene makes for an ideal candidate for electrochemical applications due to its large surface area (2630 m²/g), unique heterogeneous electron transfer rate, and stability under extreme temperatures compared to traditional carbon electrodes.^{11,52-55} Carbon material has been widely used for electrochemical applications due to its inert electrochemistry, rich surface chemistry, and electro-catalytic activities for various redox reactions.⁵⁶⁻⁵⁹ The edge plane and basal plane-defect sites of the highly ordered pyrolytic graphite greatly favors electrochemical activity.^{56,57} Research shows that a high proportion of edge plane sites in graphene layers to improve electron transfer rates compared to reactivity sites of the basal plane.⁶⁰⁻⁶⁵ Graphene's surface can adsorb gas/vapor molecules, which act as electron donors/ acceptors, changing graphene's electrical conductivity.^{66,67} Furthermore, graphene is biocompatible, making graphene a desired material for biomedical applications for biological sensing, bioimaging, to drug delivery.^{56,68-70}

1.3 Preparation of Graphene Ink

Common techniques to obtain graphene are through exfoliation, chemical vapor deposition, and epitaxial growth.^{55,71-76} The advantage of using the exfoliation technique is a high yield, tunability, and it allows us to process in solution (**Figure 1.2**). Separation of layers from the bulk material graphite is achieved by either chemical modification of

graphite or directly intercalating between the layers with small molecules via the liquid exfoliation method.^{74,77,78} Quality and yield of the graphene are very much dependent on the technique used for exfoliation. For this project, the graphene inks were synthesized via liquid exfoliation. Liquid exfoliation can be done with organic solvents. The enthalpy of mixing is affected by the balance of surface energies between graphene and the solvent.^{78,79} Studies show that the solvent should have a surface tension withing 40-50 mJ/m² and the enthalpy of mixing should be close to zero to achieve efficient exfoliation of the graphene layers. N-Methyl-2-pyrrolidone (NMP) and Dimethylformamide (DMF) are suitable solvents for exfoliation, but these solvents can be toxic, expensive, and difficult to remove once the exfoliation process is done.^{78,80,81} A more desirable method is using ethanol as the solvent, but this requires the addition of stabilizing polymers/surfactants.

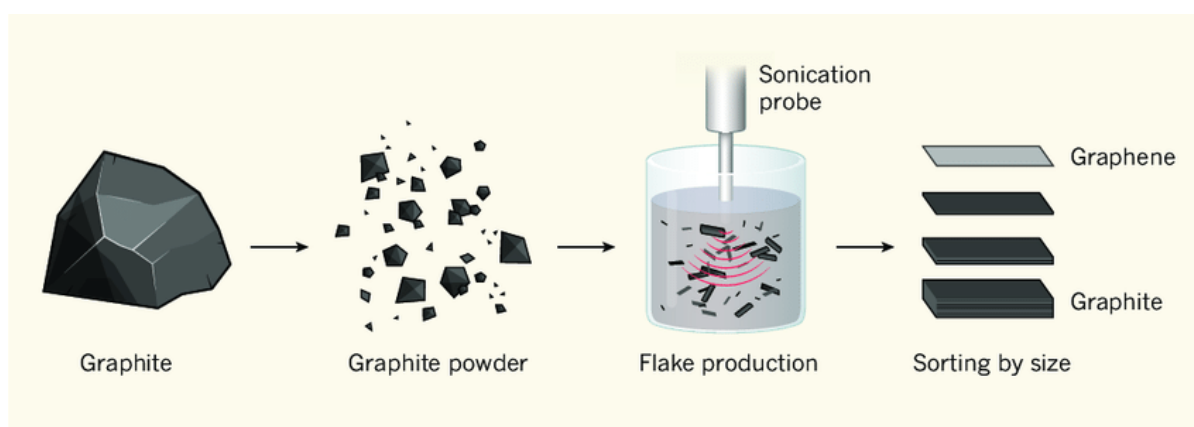


Figure 1.2 Schematic of the exfoliation process from graphite to graphene⁸²

Surfactants are essential to match the surface tension needed to exfoliate the graphene layers in ethanol. Surfactants lower the surface tension of the solution, increasing the dispersion of graphene layers.⁷⁷ Several reports have recently shown a high yield of graphene layers exfoliated using ethanol and ethyl cellulose (EC) as a surfactant

and a stabilizing polymer.^{77,83–85} Using high powered probe tip ultra-sonicators have extensively lowered the sonication time from 400 hours to a couple of hours.⁸⁶ The ultrasound in this sonication process travels through the medium, creating microbubbles. The pressure outside these microbubbles is so much greater than inside that the bubbles implode. These microbubbles' microsecond implosions generate localized hotspot regions comprising high temperatures up to 5000K and pressure up to 1000 bars. This energy causes the breakup of the graphene layers held together by weak van der Waal bonds. Sonication time and amplitude affect the flakes' lateral size; the longer the sonication times smaller the flakes' size.^{77,79,80,86,87}

1.4 Inkjet Printing

Conventional fabrication processes for flexible sensor development, such as vacuum deposition, photolithography, and epitaxial growth of electronic materials, tend to be complicated and expensive, often requiring lithographic patterning and high-temperature processing.⁸⁸ As a result, additive electronics manufacturing techniques, such as inkjet printing (IJP), aerosol jet printing (AJP), and micro-dispense printing (MDP), are being explored as potential low-cost scalable fabrication methods for flexible sensor systems.^{5,89–92} IJP is a promising route towards achieving the above-desired gas sensor characteristics. IJP provides several advantages over other deposition techniques, such as dip-coating, spray coating, and electrophoretic deposition^{93–95}. With inkjet printing, the process is rapid as no prefabricated masks or templates are required, and the cost of printing is low. Inkjet printing is a drop-on-demand process with four stages: drop ejection, drop flight, drop spreading, and drop solidification (**Figure 1.3**).^{96,97}

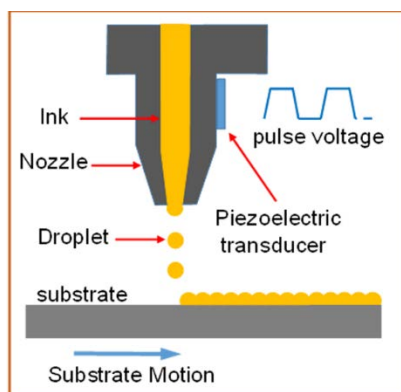


Figure 1.3 Schematic of inkjet printing⁹⁸

The feature resolution depends on drop volume, placement accuracy, and substrate-ink interaction. Droplet resolution is characterized by the size, shape, and volume of the drops affected by the nozzle size, fluid viscosity, and surface tension.⁹³ Viscosity, particle size, and solvent system of the ink are critical parameters for inkjet printing. Inkjet printing provides the advantages of rapid prototyping and on-demand digital printing in areas only where the material needs to be deposited. Constraints arise when dealing with the viscosity of the inks and particle size/concentration. The recommended viscosity values for printable inks should be below 20 mPa·s and 3 mPa·s for piezoelectric print heads and thermal print heads, respectively.⁹⁹ Higher boiling point temperature solvents are also preferred when using an inkjet printer to avoid droplet jetting inconsistencies and coffee staining effects.^{100,101} When using water-based inks, tuning the viscosity and modifying the substrate surface energy (adding a water-soluble sacrificial layer or oxygen plasma) can help obtain higher resolution features^{102,103}. Moreover, one can print multiple layers with ease and control the material's deposition with great precision.

Inkjet printing of graphene has been well established, and several groups have demonstrated inkjet-printed graphene chemical and biological sensors.^{84,92,94,101,104–109}

Graphene inks are typically produced through liquid-phase exfoliation of graphite or chemical or thermal reduction of graphene oxide.^{78,110} These processes usually result in submicron graphene crystal domains and give rise to numerous point defects within the lattice and closed-contour defects around the flake's edge.⁴⁴ Under applied electrical bias, these defects result in highly localized electric fields, which can be modified by absorbed molecules/target analytes. Combined with the high electrical conductivity and specific surface area of graphene, these defects enable highly sensitive graphene-based sensors to detect target molecules with parts per billion sensitivity in controlled environments.⁴⁴ Inkjet printing demonstrates the potential for next-generation printable and flexible sensors; several challenges remain before feature resolution and gas sensitivities can be compared to the conventional vacuum-based fabrication process. Moreover, further work is needed to improve consistency, repeatability, and uniformity of inkjet-printed devices.

1.5 Aerosol-Jet Printing

Aerosol jet printing (AJP) is another relatively new printing method where the droplet size is much smaller than inkjet printing, resulting in refined features and higher resolution. The aerosol jet micro-scale printing system consists of three major parts: an ultrasonic/pneumatic actuator, a deposition nozzle, and a moveable stage to place the substrate.^{8,111-114} AJP introduces new direct-write capabilities with consistent deposition, allows a broader range of ink viscosities (1 to 1000 cP), and higher feature resolution (~10 μm).⁹⁴ A typical AJP system consists of two modes of aerosolization: pneumatic and ultrasonic.

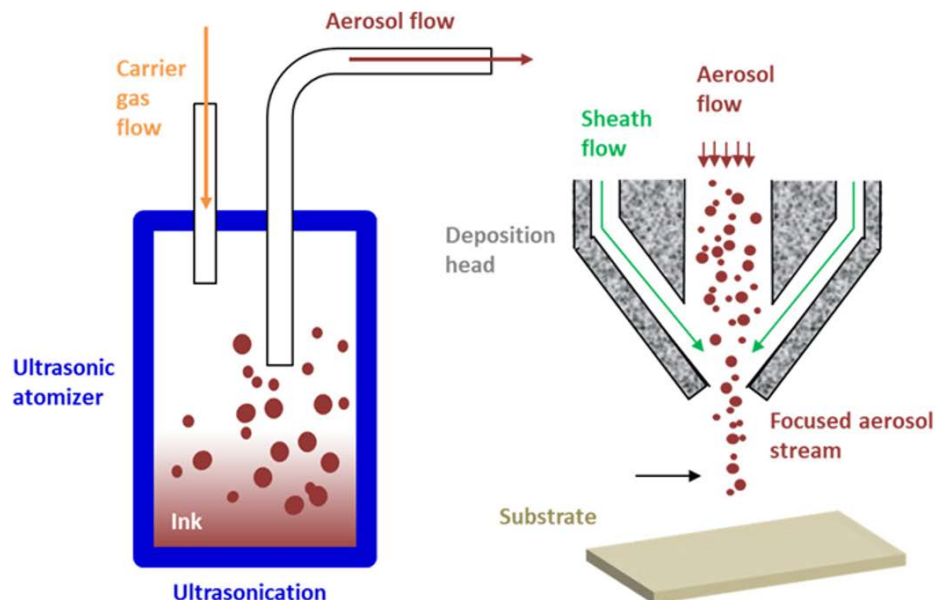


Figure 1.4 Schematic of aerosol jet printing¹¹⁵

A representation of the AJP in **Figure 1.4** shows the ink atomized (aerosol) using an ultrasonic atomizer; high-pressure gas is injected into the chamber to create a capillary action assisted spraying of the inks. Pneumatic atomizers can magnetically stir the ink mixture allowing for better atomization of the ink having non-homogeneously suspended particles in the dispersion medium. The ultrasonic atomizer creates a mist of atomized droplets by the particles' atomization on the ink's surface. The mist is then introduced into a gas flow, carried through a tube, and delivered to the deposition nozzle. The atomized gases are protected by a sheath of N_2 gas, creating a clog-resistant nozzle and high-density microdroplets. The inks' continuous stream tightly focuses the jetting to the substrate, creating line features as small as $10\mu m$ in width and a few hundred nanometers to micrometer thickness. The ultrasonic atomizer and the multi-axis positioning stage enables conformal printing on non-planar surfaces, such as on a golf ball. AJP allows for rapid integration when compared to other additive technologies.⁸⁹ For optimal print, vital parameters such as atomizer power, atomizer gas, sheath gas flow

rate, the ink's viscosity are needed to be tuned. Moreover, the substrate's temperature and deposition velocity should also be carefully adjusted to achieve a repeatable outcome. AJP requires tuning of several parameters to achieve optimal print resolution; therefore, it's challenging to print devices with AJP compared to Inkjet printing. AJP is a novel technique; therefore, further investigations are required to achieve fully optimize and high-performing printed devices.

1.6 Graphene-Based Sensors

Graphene, due to its electrical and mechanical properties, makes an ideal candidate for sensor application. Graphene-based electrodes include wide potential windows, large specific surface area, and good electrochemical activity for many redox reactions.^{55,58,116} The number of publications on graphene-based sensors (e.g., gas/vapor, biosensor, pH, etc.) has increased (> 1000) over the period from 2007.^{11,44,53,68,105,117-119} From all the different forms for functionality, chemiresistor is most widely used to construct the sensor. The chemiresistor approach is when the voltage is applied to the device's electrodes and detects the current fluctuation over time with composition changes.^{120,121} Realistic detections can be achieved with real-time monitoring and analysis of the sensing devices' response curves.¹²⁰ Surface modification of graphene by integrating it with other functional nanomaterials produces versatile electrochemical sensing performance.¹²² Compared to other materials (metal or carbon electrodes), graphene shows high conductivity, simple fabrication, biocompatible, and inexpensive material.^{57,123} Critical parameters to evaluate the performance include resistance, sensitivity, detection limit, response time, recovery time, and selectivity.¹²⁰ Chapter 2 in this dissertation outlines a review of inkjet-printed graphene and CNT-based sensors to

understand and apply these techniques to fabricate the graphene electrodes. Chapter 3 focuses on investigating AJP graphene interconnects' power dissipation, highlighting the limitation of high temperature and high-powered sensor applications fabricated on a low thermally conductive flexible substrate. Moreover, Chapter 4 evaluates electrochemical performance of the inkjet printed graphene electrodes developed here compared to other printed/fabricated electrodes.

1.7 Flexible Hybrid Electronics

The recent development of heterogeneous integration platform allows us to integrate the printed devices with American Semiconductor Inc.'s (ASI) flexible silicon-on-polymer CMOS integrated circuits (Flex-ICs) (**Figure 1.5**) to develop a conceptual design for a flexible hybrid sensor (**Figure 1.6**).¹²⁴ The flexible hybrid sensor system includes microcontrollers, A/D converters, memory, flexible RFID/NFC/Bluetooth communications chips, and a power source to integrate with the printed devices on polyimide substrates. This system will provide a computational backbone to the sensor system developed here. Four primary connection techniques widely used include wire

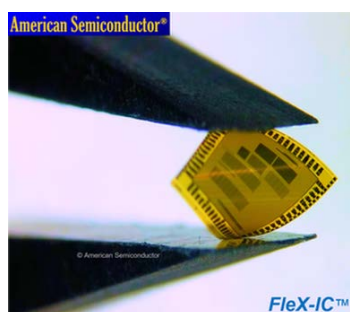


Figure 1.5 American Semiconductors Flex-ICs¹²⁴

bonding, tape automated bonding, anisotropic conductive adhesives (ACA) for flip-chip bonding, and printing for direct bonding to Flex-IC pads.^{125–128} The direct bonding technique includes four steps: dispensing a non-conductive adhesive (NCA), placing the

components with the contact part facing upward and curing the NCA, MDP the circuit patterns, as well as the interconnects, and sintering.¹²⁸ Compared to other techniques, direct bonding method allows for a stable



Figure 1.6 Optical image of a flexible hybrid sensor¹²⁹

and robust mechanical connection between the components and the flexible substrate without compromising the performance. The preliminary work on this project is discussed in Chapter 5.

1.8 Conclusion

This chapter introduces additive manufacturing techniques such as aerosol jet and inkjet printing fabrication of graphene-based printed structures for the conceptual development of a flexible hybrid sensor. As discussed earlier, graphene has excellent mechanical, electrical, thermal, and optical properties. Graphene-based sensors have also shown great potential to target chemical and biological analytes and monitor state variables, such as temperature, humidity, and pressure. Properties of graphene mentioned above, have opened a new possibility to synthesize countless graphene-based composites in many different applications. Furthermore, the need for flexible and portable sensors

that show high sensitivity and selectively in real-time is growing significantly. This hybrid integration is needed for a develop next-generation flexible hybrid system desired for portable and wearable applications in space, military, and commercial applications.

1.9 Dissertation Outline

A review is presented in Chapter 2 to understand state of the art on using additive manufacturing tools to fabricate conformal gas sensors based on graphene and carbon nanotube materials. This review is a critical first step in thoroughly observing the rheology of ink synthesis, printing procedures, and sensors' performance. This review allows us to understand the advantages and limitations of fabricating such sensors.

Aerosol Jet Printing is a novel technique compared to inkjet printing; and, limited studies have been done on Joule heating of AJP printed devices. Investigation on power dissipation of printed graphene interconnects fabricated on low thermal conductive substrate such as polyimide is described in Chapter 3. To analyze the performance of AJP graphene interconnects, rheological, mechanical, electrical, and power dissipation measurements, along with their background knowledge and further discussion, are all included.

Chapter 4 comprises the rheological requirements of the graphene ink to enable successful inkjet printing. This chapter investigates the electrochemical performance of inkjet-printed graphene-based electrodes for conformal sensors application. The electrodes' performance was characterized by assessing their electrical conductivity, thermal properties, cyclic voltammetry scans, pH sensitivity, and mechanical stability.

Future work on integrating flexible inkjet printed graphene-based electrodes with Flex-ICs using a heterogeneous integration platform to design a prototype of a flexible

hybrid ion-selective sensor is described in Chapter 5. Preliminary results on the integration process and Na⁺ ion-selective are included as well.

Finally, in Chapter 6, the summary of the results obtained is discussed, and the outlook is proposed to advance the outcomes of this study.

1.10 References

1. Lam Po Tang, S. Recent developments in flexible wearable electronics for monitoring applications. *Trans. Inst. Meas. Control* **29**, 283–300 (2007).
2. Printed and Flexible Sensors 2017-2027: Technologies, Players, Forecasts: IDTechEx. Available at: <http://www.idtechex.com/research/reports/printed-and-flexible-sensors-2017-2027-technologies-players-forecasts-000504.asp>. (Accessed: 23rd January 2017)
3. Yatsenko, V. A. The development of nanosensors for space applications. in *Proceedings of CAOL 2008: 4th International Conference on Advanced Optoelectronics and Lasers* 210–212 (2008). doi:10.1109/CAOL.2008.4671994
4. Agosteo, S. Overview of novel techniques for radiation protection and dosimetry. in *Radiation Measurements* (2010). doi:10.1016/j.radmeas.2010.06.042
5. Clinton, R. G. *NASA's In Space Manufacturing Initiative and Additive Manufacturing Development for Rocket Engine Space Flight Hardware*. (2016).
6. Thryft, Ann R. (senior Technical Editor, M. & A. NASA Builds 3D Printer for Space. *Des. News* **68**, p27-28 (2013).
7. Gibson, I., Rosen, D. W. & Stucker, B. Additive Manufacturing Technologies: Rapid Prototyping to Direct Digital Manufacturing. *Media* 193–198 (2010). doi:10.1595/205651315X688406
8. Seifert, T. *et al.* Additive manufacturing technologies compared: Morphology of deposits of silver ink using inkjet and aerosol jet printing. *Ind. Eng. Chem. Res.* **54**, 769–779 (2015).
9. Hossain, R. F., Deaguero, I. G., Boland, T. & Kaul, A. B. Biocompatible, large-format, inkjet printed heterostructure MoS₂-graphene photodetectors on conformable substrates. *npj 2D Mater. Appl.* **1**, 28 (2017).

10. Mas-Ballesté, R., Gómez-Navarro, C., Gómez-Herrero, J. & Zamora, F. 2D materials: to graphene and beyond. *Nanoscale* **3**, 20–30 (2011).
11. Yang, S., Jiang, C. & Wei, S. huai. Gas sensing in 2D materials. *Applied Physics Reviews* (2017). doi:10.1063/1.4983310
12. Mannix, A. J., Kiraly, B., Hersam, M. C. & Guisinger, N. P. Synthesis and chemistry of elemental 2D materials. *Nature Reviews Chemistry* **1**, (2017).
13. Novoselov, K. S., Mishchenko, A., Carvalho, A., Neto, A. H. C. & Road, O. 2D materials and van der Waals heterostructures. *Science (80-.)*. **353**, aac9439 (2016).
14. Terrones, M. *et al.* Graphene and graphite nanoribbons: Morphology, properties, synthesis, defects and applications. *Nano Today* **5**, 351–372 (2010).
15. Novoselov, K. S. *et al.* Unconventional quantum Hall effect and Berry's phase of 2π in bilayer graphene. *Nat. Phys.* **2**, 177–180 (2006).
16. Castro Neto, A. H., Guinea, F., Peres, N. M. R., Novoselov, K. S. & Geim, A. K. The electronic properties of graphene. *Rev. Mod. Phys.* **81**, 109–162 (2009).
17. Geim, A. K. & Novoselov, K. S. The rise of graphene. *Nat. Mater.* **6**, 183–191 (2007).
18. Lewandowski, C. M., Co-investigator, N. & Lewandowski, C. M. *Carbon Nanotube and Graphene Device Physics. Cambridge* **1**, (2015).
19. Chen, H. Y., Maiti, S. & Son, D. H. Doping location-dependent energy transfer dynamics in Mn-doped CdS/ZnS nanocrystals. *ACS Nano* **6**, 583–591 (2012).
20. Estrada, D. *et al.* Thermal transport in layer-by-layer assembled polycrystalline graphene films. *npj 2D Mater. Appl.* (2019). doi:10.1038/s41699-019-0092-8
21. Xia, F., Wang, H., Xiao, D., Dubey, M. & Ramasubramaniam, A. Two-dimensional material nanophotonics. *Nat. Photonics* **8**, 899–907 (2014).
22. (PDF) Irradiation-induced metal-insulator transition in monolayer graphene.
23. Novoselov, K. S. *et al.* Two-dimensional gas of massless Dirac fermions in graphene. *Nature* (2005). doi:10.1038/nature04233
24. Dorgan, V. E., Bae, M. H. & Pop, E. Mobility and saturation velocity in graphene on SiO₂. *Appl. Phys. Lett.* **97**, (2010).

25. Basu, S. & Bhattacharyya, P. Recent developments on graphene and graphene oxide based solid state gas sensors. *Sensors and Actuators, B: Chemical* (2012). doi:10.1016/j.snb.2012.07.092
26. Pantelides, S. T., Puzyrev, Y., Tsetseris, L. & Wang, B. Defects and doping and their role in functionalizing graphene. *MRS Bull.* (2012). doi:10.1557/mrs.2012.187
27. Mishra, A. K. & Ramaprabhu, S. Functionalized graphene sheets for arsenic removal and desalination of sea water. *DES* **282**, 39–45 (2011).
28. Gao, W. The chemistry of graphene oxide. in *Graphene Oxide: Reduction Recipes, Spectroscopy, and Applications* 61–95 (2015). doi:10.1007/978-3-319-15500-5_3
29. Balandin, A. a *et al.* Superior thermal conductivity of single-layer graphene 2008. *Nano Lett.* **8**, 902–907 (2008).
30. Xu, Z. & Buehler, M. J. Heat dissipation at a graphene–substrate interface. *J. Phys. Condens. Matter* **24**, 475305 (2012).
31. Ghosh, S. *et al.* Extremely high thermal conductivity of graphene: Prospects for thermal management applications in nanoelectronic circuits. *Appl. Phys. Lett.* **92**, 1–4 (2008).
32. Bae, M. H., Ong, Z. Y., Estrada, D. & Pop, E. Imaging, simulation, and electrostatic control of power dissipation in graphene devices. *Nano Lett.* **10**, 4787–4793 (2010).
33. Freitag, M. *et al.* Energy dissipation in graphene field-effect transistors. *Nano Lett.* **9**, 1883–1888 (2009).
34. Pop, E. Energy dissipation and transport in nanoscale devices. *Nano Research* **3**, 147–169 (2010).
35. Pop, E. The role of electrical and thermal contact resistance for Joule breakdown of single-wall carbon nanotubes. *Nanotechnology* **19**, (2008).
36. Liao, A. D. *et al.* Thermally limited current carrying ability of graphene nanoribbons. *Phys. Rev. Lett.* **106**, (2011).

37. Prakash Gupta, M. *et al.* Impact of thermal boundary conductances on power dissipation and electrical breakdown of carbon nanotube network transistors. *J. Appl. Phys.* **112**, (2012).
38. Li, X., Kong, B. D., Zavada, J. M. & Kim, K. W. Strong substrate effects of Joule heating in graphene electronics. *Appl. Phys. Lett.* **99**, 10–14 (2011).
39. Lee, K., Moon, J.-S., Oh, T., Kim, S. & Asbeck, P. Analysis of heat dissipation of epitaxial graphene devices on SiC. *Solid. State. Electron.* **101**, 44–49 (2014).
40. Grosse, K. L. *et al.* Direct observation of resistive heating at graphene wrinkles and grain boundaries. *Appl. Phys. Lett.* **105**, (2014).
41. Yasaei, P. *et al.* Bimodal Phonon Scattering in Graphene Grain Boundaries. *Nano Lett.* (2015). doi:10.1021/acs.nanolett.5b01100
42. Koepke, J. C. *et al.* Atomic-scale evidence for potential barriers and strong carrier scattering at graphene grain boundaries: A scanning tunneling microscopy study. *ACS Nano* **7**, 75–86 (2013).
43. Kumar, B. *et al.* The role of external defects in chemical sensing of graphene field-effect transistors. *Nano Lett.* **13**, 1962–1968 (2013).
44. Salehi-Khojin, A. *et al.* Chemical sensors based on randomly stacked graphene flakes. *Appl. Phys. Lett.* 9–12 (2012).
45. Banerjee, S. *et al.* Electrochemistry at the edge of a single graphene layer in a nanopore. *ACS Nano* **7**, 834–43 (2013).
46. Valota, A. T. *et al.* Electrochemical behavior of monolayer and bilayer graphene. *ACS Nano* (2011). doi:10.1021/nn202878f
47. Novoselov, K. S. *et al.* A roadmap for graphene. *Nature* **490**, 192–200 (2012).
48. Bonaccorso, F., Sun, Z., Hasan, T. & Ferrari, A. C. Graphene Photonics and Optoelectronics. *Nat. Photonics* **4**, 611–622 (2010).
49. Ferrari, A. C. *et al.* Raman spectrum of graphene and graphene layers. *Phys. Rev. Lett.* (2006). doi:10.1103/PhysRevLett.97.187401
50. Jorio, A., Martins Ferreira, E. H., G., L., A., C. & B., R. Measuring Disorder in Graphene with Raman Spectroscopy. in *Physics and Applications of Graphene - Experiments* (2011). doi:10.5772/15374

51. Cañado, L. G. *et al.* General equation for the determination of the crystallite size la of nanographite by Raman spectroscopy. *Appl. Phys. Lett.* **88**, (2006).
52. Latif, U. & Dickert, F. L. Graphene hybrid materials in gas sensing applications. *Sensors (Switzerland)* (2015). doi:10.3390/s151229814
53. Yavari, F. & Koratkar, N. Graphene-based chemical sensors. *Journal of Physical Chemistry Letters* (2012). doi:10.1021/jz300358t
54. Hill, E. W., Vijayaraghavan, A. & Novoselov, K. Graphene sensors. *IEEE Sens. J.* (2011). doi:10.1109/JSEN.2011.2167608
55. Huang, X., Zeng, Z., Fan, Z., Liu, J. & Zhang, H. Graphene-based electrodes. *Advanced Materials* **24**, 5979–6004 (2012).
56. Shao, Y. *et al.* Graphene based electrochemical sensors and biosensors: A review. *Electroanalysis* **22**, 1027–1036 (2010).
57. Pumera, M. *et al.* Graphene for electrochemical sensing and biosensing. *TrAC - Trends Anal. Chem.* **29**, 954–965 (2010).
58. Martin, P. Electrochemistry of gaphene: New horizons for sensing and energy storage. *Chem. Rec.* **9**, 211–223 (2009).
59. Chen, D. *et al.* Graphene-based materials in electrochemistry. *Chem. Soc. Rev.* **39**, 3157 (2010).
60. Randviir, E. P. *et al.* Electrochemistry of Q-Graphene. *Nanoscale* (2012). doi:10.1039/c2nr31823g
61. Ambrosi, A., Bonanni, A. & Pumera, M. Electrochemistry of folded graphene edges. *Nanoscale* (2011). doi:10.1039/c1nr10136f
62. Brownson, D. A. C. *et al.* Electrochemistry of graphene: not such a beneficial electrode material? *RSC Adv.* **1**, 978 (2011).
63. Loh, K. P., Bao, Q., Eda, G. & Chhowalla, M. Graphene oxide as a chemically tunable platform for optical applications. *Nat. Chem.* (2010). doi:10.1038/nchem.907
64. Vedala, H., Sorescu, D. C., Kotchey, G. P. & Star, A. Chemical sensitivity of graphene edges decorated with metal nanoparticles. *Nano Lett.* (2011). doi:10.1021/nl2006438

65. Yuan, W. *et al.* The edge- and basal-plane-specific electrochemistry of a single-layer graphene sheet. *Sci. Rep.* **3**, 2248 (2013).
66. Dan, Y., Lu, Y., Kybert, N. J., Luo, Z. & Johnson, A. T. C. Intrinsic response of graphene vapor sensors. *Nano Lett.* **9**, 1472–1475 (2009).
67. Toda, K., Furue, R. & Hayami, S. Recent progress in applications of graphene oxide for gas sensing: A review. *Analytica Chimica Acta* (2015).
doi:10.1016/j.aca.2015.02.002
68. Choi, W. & Alwarappan, S. Graphene-Based Biosensors and Gas Sensors. in *Graphene* (2018). doi:10.1201/b11259-11
69. Bollella, P., Fusco, G., Tortolini, C., Sanzò, G. & Favero, G. Biosensors and Bioelectronics Beyond graphene : Electrochemical sensors and biosensors for biomarkers detection. *Biosens. Bioelectron.* **89**, 152–166 (2017).
70. Kuila, T. *et al.* Recent advances in graphene-based biosensors. *Biosensors and Bioelectronics* (2011). doi:10.1016/j.bios.2011.05.039
71. Paredes, J. I. *et al.* Environmentally friendly approaches toward the mass production of processable graphene from graphite oxide. *J. Mater. Chem.* **21**, 298–306 (2011).
72. Zhao, Z. & Qiu, J. Graphene: Synthesis, properties, and applications. in *Carbon Nanomaterials, Second Edition* (2013). doi:10.1201/b15591
73. Zhang, Y. *et al.* Characterization and simulation of liquid phase exfoliated graphene-based films for heat spreading applications. *Carbon N. Y.* **106**, 195–201 (2016).
74. Xu, Y., Cao, H., Xue, Y., Li, B. & Cai, W. Liquid-phase exfoliation of graphene: An overview on exfoliation media, techniques, and challenges. *Nanomaterials* (2018). doi:10.3390/nano8110942
75. Campbell, S. A. *The Science and Engineering of Microelectronic Fabrication.* Oxford University Press **476**, (2001).
76. Westervelt, R. M. & Westervelt, R. M. Graphene nanoelectronics. *Science (80-)*. **322**, 2007–2008 (2008).
77. Coleman, J. N. Liquid exfoliation of defect-free graphene. *Acc. Chem. Res.* **46**, 14–22 (2013).

78. Hernandez, Y. *et al.* High-yield production of graphene by liquid-phase exfoliation of graphite. *Nat. Nanotechnol.* **3**, 563–568 (2008).
79. Khan, U. *et al.* Size selection of dispersed, exfoliated graphene flakes by controlled centrifugation. *Carbon N. Y.* **50**, 470–475 (2012).
80. Bourlinos, A. B., Georgakilas, V., Zboril, R., Sterioti, T. A. & Stubos, A. K. Liquid-Phase Exfoliation of Graphite Towards Solubilized Graphenes. *Small* **5**, 1841–1845 (2009).
81. Lee, K. *et al.* Electrical characteristics of molybdenum disulfide flakes produced by liquid exfoliation. *Adv. Mater.* **23**, 4178–4182 (2011).
82. Penney, J. & Tsai, L. H. Elimination of senescent cells prevents neurodegeneration in mice. *Nature* (2018). doi:10.1038/d41586-018-06677-7
83. Gao, Y., Shi, W., Wang, W., Leng, Y. & Zhao, Y. Inkjet printing patterns of highly conductive pristine graphene on flexible substrates. *Ind. Eng. Chem. Res.* **53**, 16777–16784 (2014).
84. Secor, E. B., Prabhumirashi, P. L., Puntambekar, K., Geier, M. L. & Hersam, M. C. Inkjet printing of high conductivity, flexible graphene patterns. *J. Phys. Chem. Lett.* **4**, 1347–1351 (2013).
85. Ye, J., Li, X., Zhao, J., Mei, X. & Li, Q. A Facile Way to Fabricate High-Performance Solution-Processed n-MoS₂/p-MoS₂ Bilayer Photodetectors. *Nanoscale Res. Lett.* **10**, 454 (2015).
86. Gharibzahedi, S. M. T. & Jafari, S. M. Fabrication of Nanoemulsions by Ultrasonication. in *Nanoemulsions: Formulation, Applications, and Characterization* (2018). doi:10.1016/B978-0-12-811838-2.00009-6
87. Zhu, L. *et al.* High-quality production of graphene by liquid-phase exfoliation of expanded graphite. *Mater. Chem. Phys.* **137**, 984–990 (2013).
88. He, Q., Wu, S., Yin, Z. & Zhang, H. Graphene-based electronic sensors. *Chem. Sci.* **3**, 1764 (2012).
89. Jabari, E. & Toyserkani, E. Micro-scale aerosol-jet printing of graphene interconnects. *Carbon N. Y.* **91**, 321–329 (2015).
90. Zhan, Z. *et al.* Inkjet-printed optoelectronics. *Nanoscale* **9**, 965–993 (2017).

91. Renn, M. J. Aerosol-jet printed thin film transistors. *WHITEPAPER - Optomec* 3–5 (2010).
92. Torrisi, F. *et al.* Inkjet-printed graphene electronics. *ACS Nano* **6**, 2992–3006 (2012).
93. Singh, M., Haverinen, H. M., Dhagat, P. & Jabbour, G. E. Inkjet printing-process and its applications. *Adv. Mater.* **22**, 673–685 (2010).
94. Deiner, L. J. & Reitz, T. L. Inkjet and aerosol jet printing of electrochemical devices for energy conversion and storage. *Advanced Engineering Materials* **19**, (2017).
95. Sridhar, a, Blaudeck, T. & Baumann, R. Inkjet Printing as a Key Enabling Technology for Printed Electronics. *Mater. Matters* **6**, 1–8 (2009).
96. Cummins, G. & Desmulliez, M. P. Y. Inkjet printing of conductive materials: A review. *Circuit World* (2012). doi:10.1108/03056121211280413
97. Tekin, E., Smith, P. J. & Schubert, U. S. Inkjet printing as a deposition and patterning tool for polymers and inorganic particles. *Soft Matter* (2008). doi:10.1039/b711984d
98. Inkjet printing process for kesterite solar cells. Available at: <https://phys.org/news/2015-05-inkjet-kesterite-solar-cells.html>. (Accessed: 8th October 2020)
99. Dybowska-Sarapuk, L. *et al.* Efficient inkjet printing of graphene-based elements: Influence of dispersing agent on ink viscosity. *Nanomaterials* (2018). doi:10.3390/nano8080602
100. Li, J., Lemme, M. C. & Östling, M. Inkjet printing of 2D layered materials. *ChemPhysChem* **15**, 3427–3434 (2014).
101. Li, J. *et al.* Efficient inkjet printing of graphene. *Adv. Mater.* **25**, 3985–3992 (2013).
102. Sun, J. *et al.* Fabricating High-Resolution Metal Pattern with Inkjet Printed Water-Soluble Sacrificial Layer. *ACS Appl. Mater. Interfaces* (2020). doi:10.1021/acsami.0c01138

103. Nguyen, P. Q. M., Yeo, L. P., Lok, B. K. & Lam, Y. C. Patterned surface with controllable wettability for inkjet printing of flexible printed electronics. *ACS Appl. Mater. Interfaces* (2014). doi:10.1021/am4054546
104. Komuro, N., Takaki, S., Suzuki, K. & Citterio, D. Inkjet printed (bio)chemical sensing devices. *Analytical and Bioanalytical Chemistry* (2013). doi:10.1007/s00216-013-7013-z
105. Cinti, S. & Arduini, F. Graphene-based screen-printed electrochemical (bio)sensors and their applications: Efforts and criticisms. *Biosensors and Bioelectronics* **89**, 107–122 (2017).
106. Guo, Y., Patanwala, H. S., Bognet, B. & Ma, A. W. K. Inkjet and inkjet-based 3D printing: Connecting fluid properties and printing performance. *Rapid Prototyp. J.* (2017). doi:10.1108/RPJ-05-2016-0076
107. Pandhi, T., Chandnani, A., Subbaraman, H. & Estrada, D. A review of inkjet printed graphene and carbon nanotubes based gas sensors. *Sensors (Switzerland)* (2020). doi:10.3390/s20195642
108. Dua, V. *et al.* All-organic vapor sensor using inkjet-printed reduced graphene oxide. *Angew. Chemie - Int. Ed.* **49**, 2154–2157 (2010).
109. Hondred, J. A. *et al.* Printed Graphene Electrochemical Biosensors Fabricated by Inkjet Maskless Lithography for Rapid and Sensitive Detection of Organophosphates. *ACS Appl. Mater. Interfaces* **10**, 11125–11134 (2018).
110. Stankovich, S. *et al.* Synthesis of graphene-based nanosheets via chemical reduction of exfoliated graphite oxide. *Carbon N. Y.* **45**, 1558–1565 (2007).
111. Pennebaker, W. B. Aerosol Jet Printing. *Proc Soc Inf Disp* **17**, 160–168 (1976).
112. Secor, E. B. & Hersam, M. C. Emerging carbon and post-carbon nanomaterial inks for printed electronics. *J. Phys. Chem. Lett.* **6**, 620–626 (2015).
113. Rodriguez, J. *et al.* Dielectric Patterning Using Aerosol Jet Printing. *J. Imaging Sci. Technol.* **56**, 1–7 (2012).
114. Hedges, M. & Marin, A. B. 3D Aerosol Jet® Printing - Adding Electronics Functionality to RP/RM. *WHITEPAPER - Optomec* 14–15 (2012). doi:10.1002/adma.201504958

115. Aerosol Jet Prints Skin-Friendly “Tattoos” with Active Electronics | Machine Design. Available at: <https://www.machinedesign.com/medical-design/article/21122059/aerosol-jet-prints-skinfriendly-tattoos-with-active-electronics>. (Accessed: 8th October 2020)
116. Kang, X. *et al.* A graphene-based electrochemical sensor for sensitive detection of paracetamol. *Talanta* **81**, 754–759 (2010).
117. Amin, K. R. & Bid, A. Graphene as a sensor. *Curr. Sci.* **107**, 430–436 (2014).
118. Pumera, M., Ambrosi, A., Bonanni, A., Chng, E. L. K. & Poh, H. L. Graphene for electrochemical sensing and biosensing. *TrAC - Trends Anal. Chem.* **29**, 954–965 (2010).
119. Meng, F. L., Guo, Z. & Huang, X. J. Graphene-based hybrids for chemiresistive gas sensors. *TrAC - Trends in Analytical Chemistry* (2015). doi:10.1016/j.trac.2015.02.008
120. Wang, T. *et al.* A Review on Graphene-Based Gas/Vapor Sensors with Unique Properties and Potential Applications. *Nano-Micro Letters* (2016). doi:10.1007/s40820-015-0073-1
121. Zhang, T., Mubeen, S., Myung, N. V. & Deshusses, M. A. Recent progress in carbon nanotube-based gas sensors. *Nanotechnology* (2008). doi:10.1088/0957-4484/19/33/332001
122. Kuila, T. *et al.* Chemical functionalization of graphene and its applications. *Progress in Materials Science* **57**, 1061–1105 (2012).
123. Singh, E., Meyyappan, M. & Nalwa, H. S. Flexible Graphene-Based Wearable Gas and Chemical Sensors. *ACS Appl. Mater. Interfaces* **9**, 34544–34586 (2017).
124. FleX-ICs - American Semiconductor, Inc. Available at: <https://www.americansemi.com/flex-ics.html>. (Accessed: 26th September 2020)
125. Rodriguez, A., Estrada, D., Subbaraman, H. & Wilson, D. Anisotropic Conductive Adhesives on Flexible Hybrid Electronics. *Idaho Conf. Undergrad. Res.* (2018).
126. Mäntysalo, M. *et al.* System integration of smart packages using printed electronics. in *Proceedings - Electronic Components and Technology Conference* (2012). doi:10.1109/ECTC.2012.6248957

127. Stoppa, M. & Chiolerio, A. Wearable electronics and smart textiles: A critical review. *Sensors (Switzerland)* **14**, 11957–11992 (2014).
128. Zheng, L.-R., Tenhunen, H. & Zou, Z. *Smart Electronic Systems. Smart Electronic Systems* (2018). doi:10.1002/9783527691685
129. AFRL, NextFlex leverage open-source community to create flexible circuit system > U.S. Air Force > Article Display. Available at: <https://www.af.mil/News/Article-Display/Article/1435616/afrl-nextflex-leverage-open-source-community-to-create-flexible-circuit-system/>. (Accessed: 23rd October 2020)

CHAPTER TWO: A REVIEW OF INKJET PRINTED GRAPHENE AND CNT BASED GAS
SENSORS

Twinkle Pandhi ^{1,†}, Ashita Chandnani ^{2,†}, Harish Subbaraman ² and David Estrada ^{1,3,*}

¹ Micron School of Materials Science and Engineering, Boise State University, Boise, ID 83725, USA;

² Department of Electrical and Computer Engineering, Boise State University, Boise, ID 83725, USA;

³ Idaho National Laboratory, Idaho Falls, ID 83402, USA

*Correspondence: daveestrada@boisestate.edu

†These authors contribute equally to this manuscript.

This is an open access article distributed under the **Creative Commons Attribution License** which permits unrestricted use, distribution, and reproduction in any medium, provided the original work is properly cited.

Sensors **2020**, *20*(19), 5642;

<https://doi.org/10.3390/s20195642>

No significant changes were made to this publication.

2.1 Abstract

Graphene and carbon nanotube (CNT)-based gas/vapor sensors have gained much traction for numerous applications over the last decade due to their excellent sensing performance at ambient conditions. Inkjet printing various forms of graphene (reduced graphene oxide or modified graphene) and CNT (single-wall nanotubes (SWNTs) or multiwall nanotubes (MWNTs)) nanomaterials allows fabrication onto flexible substrates which enable gas sensing applications in flexible electronics. This review focuses on their recent developments and provides an overview of the state-of-the-art in inkjet printing of graphene and CNT based sensors targeting gases, such as NO₂, Cl₂, CO₂, NH₃, and organic vapors. Moreover, this review presents the current enhancements and challenges of printing CNT and graphene-based gas/vapor sensors, the role of defects, and advanced printing techniques using these nanomaterials, while highlighting challenges in reliability and reproducibility. The future potential and outlook of this rapidly growing research are analyzed as well.

Keywords: graphene; carbon nanotubes; inkjet printing; additive manufacturing; gas sensors; flexible electronics

2.2 Introduction

Early detection of gases and harmful vapors has become increasingly important in many fields, such as environmental pollution monitoring,¹⁻³ national defense,^{4,5} industrial emission monitoring,^{1,6,7} and medical diagnosis.^{5,8} The fundamental sensing mechanism focuses on how well the gas sensors respond to the changes in the local environment. Furthermore, the need for flexible and portable gas sensors that show high sensitivity and selectively to gas analytes in real-time is growing significantly.^{9,10} The emergence of

materials such as carbon nanotubes (CNTs) and two-dimensional (2D) materials (e.g., graphene and MoS₂) have shown great potential in targeting chemical and biological analytes, as well as in monitoring state variables, such as temperature, humidity, and pressure.^{11–13} The exemplary electrical and structural properties of these materials allow for the design of highly sensitive and selective systems while also limiting the cost, weight, and energy consumption of electronic devices.

Graphene is an attractive sensing material for printed and flexible gas sensing device development due to its flexible nature, high surface to volume ratio, unique band structure, and high electrochemical activity at defect sites.^{12,14–17} Due to its high specific surface area, high carrier mobility, and tunable crystal defect density, graphene has shown extraordinary properties and created tremendous breakthroughs in related electronics applications, particularly when it comes to trace gas/vapor sensing.^{18–23} Synthesis of graphene by chemical vapor deposition (CVD), segregation by heat treatment of silicon carbide, and liquid/chemical solvent-based exfoliation are currently areas of intense research.^{24–31} Among these, solvent exfoliation is highly compatible with printable graphene ink formulation. Moreover, the synthesis of graphene oxide (GO) is first achieved by liquid exfoliation, following the Hummers method.^{32,33} The introduction of carboxylic and carbonyl groups at the edge of the graphene sheets allows graphene to readily disperse in water. However, the disadvantage of introducing these groups is that the active layer becomes electrically insulating despite several attempts by researchers to reduce GO (rGO).³⁴ Inkjet printing of rGO based gas/vapor sensors has been reported by several groups, which we will discuss further in this review.^{35–40}

Carbon nanotubes (CNTs) are another widely used material for gas sensing due to their unique electrical and mechanical properties⁴¹. They possess very high surface area to volume ratio and very high sensitivity towards target analytes at room temperature.^{7,42} Target analytes transfer charge upon adsorption on the nanotube sidewalls or at the junctions, which leads to changes in the conductance of the CNT network. Depending upon the density of the CNT mats used for performing detection, the charge transfer leads to changes in the conductance of the CNT network. This is the key sensing mechanism for CNT gas sensors.^{43,44} CNTs are of two types: Single-walled (SWNTs) and multi-walled (MWNTs). SWNTs are analogous to a single sheet of graphene rolled up with about a nanometer diameter while MWNTs are concentric graphene rolls with diameters on the order of hundreds of nanometers⁴¹. CNTs are synthesized by arc discharge,⁴⁵ pulsed laser deposition,⁴⁶ and chemical vapor deposition,⁴⁷ which introduce different defect densities, and hence varying electrical and mechanical properties.^{41,48} CNT synthesis techniques typically produce both metallic and semiconducting nanotubes which can be separated by density gradient ultracentrifugation (DGU).^{49,50} The separated CNTs can then be dispersed in a solution to be printed by inkjet printing, allowing for rapid prototyping of printed gas sensors. Of the many challenges to printing carbon nanotubes inks, the predominant ones relate to the dispersion of CNTs in solvents and elimination of CNT bundles.^{51,52} Functionalization of CNTs with various materials that change the chemical structure and enhance the sensing performance, has allowed researchers to solve some of the dispersion related limitations of pristine CNTs.^{53,54} Inkjet printing of CNT based inks for gas sensing applications have been reported by several groups,⁵³⁻⁵⁵ which we will further discuss in this paper.

An ideal gas sensor needs to provide the following features: (i) high sensitivity to detect low concentrations of gas, (ii) rapid response, (iii) reversible operation, (iv) good selectivity to different gases of interest, (v) low-manufacturing cost, (vi) stable operation over multiple cycles of usage, and (vii) low power consumption during the operation.

Inkjet printing (IJP) is a promising route towards achieving the above desired gas sensor characteristics. IJP provides several advantages over other deposition techniques, such as dip-coating, spray coating, and electrophoretic deposition.⁵⁶⁻⁵⁸ With inkjet printing, the process is rapid as no prefabricated masks or templates are required, and the cost of printing is low. Inkjet printing is a drop-on-demand process with five stages: drop ejection, drop flight, drop spreading, and drop solidification.^{59,60} The feature resolution depends on drop volume, placement accuracy, and substrate-ink interaction. Droplet resolution is characterized by the size, shape, and volume of the drops affected by the nozzle size, fluid viscosity, and surface tension.⁵⁶ Viscosity, particle size, and solvent system of the ink are critical parameters for inkjet printing. Inkjet printing provides the advantages of rapid prototyping and on-demand digital printing in areas only where the material needs to be deposited. Constraints arise when dealing with the viscosity of the inks and particle size/concentration. Higher boiling point temperature solvents are also preferred when using an inkjet printer to avoid droplet jetting inconsistencies and coffee staining effects. When using water-based inks, tuning the viscosity and modifying the substrate surface energy (adding water-soluble sacrificial layer or oxygen plasma) can aid in obtaining higher resolution features.^{61,62} Moreover, multiple layers can be printed with ease and the deposition of the material can be controlled with great precision. There is a

great deal of research reported on inkjet printing using CNT and graphene for gas/vapor sensor applications, which we will further discuss.

In this paper, we discuss the recent developments in the area of inkjet printed gas sensors using graphene and carbon nanotubes. The outline of the paper is as follows. First, in section 1, we provide a brief overview of Graphene and CNT nanomaterials along with the introduction to inkjet printing technique. In section 2, we provide an overview of the recent experimental demonstrations in the area of inkjet printed graphene-based gas sensors. In section 3, we discuss important developments in the field of inkjet printed carbon nanotubes-based sensors for gas detection with emphasis on the impact of device geometry, the role of substrate engineering as well as the importance of chemical functionalization for printed CNT based sensors. Section 4 describes some of the newer developments like Plasma Jet Printing and Aerosol Jet Printing for fabrication of graphene and CNT based gas detectors. Section 5 discusses in detail the role of defects on the performance of graphene and CNT devices, and finally in section 6, we summarize important conclusions and scope for future research.

2.3 Graphene-Based Gas Sensors

Graphene has gained much interest of researchers since 2004 due to its remarkable electrical, mechanical, and thermal properties.^{63,64} A high mobility, near-ballistic transport and stability at room temperature, makes graphene an ideal material for sensing applications, particularly gas/vapor detection.⁶⁵ Thus, graphene-based gas sensing device development has increased exponentially, and the number of published papers has sharply increased since 2007.^{9,10,14,17,19,39,40,66–78} In this section, we will focus on inkjet printing of graphene-based gas/vapor sensor and their performance. The

performance of a sensor is measured by its sensitivity, limit of detection, response time, recovery time and selectivity. **Table 2.1** summarizes the sensing performance of recent reports on inkjet-printed graphene-based sensors for gas/vapor detection at room temperature.

Table 2.1 Printed graphene gas sensors.

Sensing Material	Printed Method	Target Gases	Detection Range/ Sensitivity (Room-Temp)	Reference
Reduce Graphene Oxide	Inkjet	NO ₂ and several vapors	100 ppm to 500 ppb	[38]
Graphene/PEDOT-PSS	Inkjet	CO ₂	100 ppm/45 μ Ohm/ppm @ 30 °C	[79]
Reduce Graphene Oxide	Inkjet	NH ₃	500 ppm	[80]
Reduce Graphene Oxide	Inkjet	NH ₃	10 ppm/2.80%	[76]
Reduce Graphene Oxide	Inkjet	NH ₃	500 ppm/6%	[81]
Graphene Oxide	Inkjet	NH ₃ and NO ₂	200–30 ppm, 150–2800 ppb	[82]
Graphene/PEDOT-PSS	Inkjet	NH ₃	5–1000 ppm	[83]
Graphene	Inkjet	NO ₂ and NH ₃	100 ppm/6.9% @ 250 °C	[78]
Graphene Oxide	Inkjet	C ₂ H ₆ O, C ₇ H ₈ and RH	30, 24, 2.4 Hz/ppm	[84]
Graphene Oxide	Inkjet	DMMP	2.5 ppm/27%	[85]
Reduced Graphene Oxide/Ag	Inkjet	DEEP	2.0 ppm/1%	[86]

Inkjet printing of an all organic rGO-based chemiresistor to detect chemical vapors in parts per million (ppm) to parts per billion (ppb) range at room temperature was first reported by Dua et al.³⁸ The rGO ink was obtained by liquid phase exfoliation of graphite and dispersing the resulting flakes in aqueous surfactant solution. Furthermore, the exfoliated graphite oxide was reduced by a green chemistry alternative, ascorbic acid (vitamin C), than using aggressive reducing agents such as hydrazine. A fewer covalently

linked C-N species observed in X-ray photoelectron (XPS) spectra of rGO films makes it evident that ascorbic acid is an effective reducing agent compared to hydrazine. The rGO dispersion was inkjet printed with controlled uniformity of the sensing layers over a 3M overhead transparency PET film, seen in **Figure 2.1a**. A plot for resistance versus time when the sensor was exposed to Cl_2 vapor is seen in **Figure 2.1b** with the signal response consistent with the photodesorption of the absorbed gases upon UV irradiation. The sensor shows a notable response to various aggressive vapors in a 100 ppm to 500 ppb concentration range and gas in a 10 ppm to 12 ppm concentration range, all at room temperature (**Figure 2.1c**). This work demonstrated that the use of very thin films shows a fast signal response and recovery compared to large films with a slow response/recovery time (minutes) for the inkjet-printed rGO-based gas/vapor sensors.

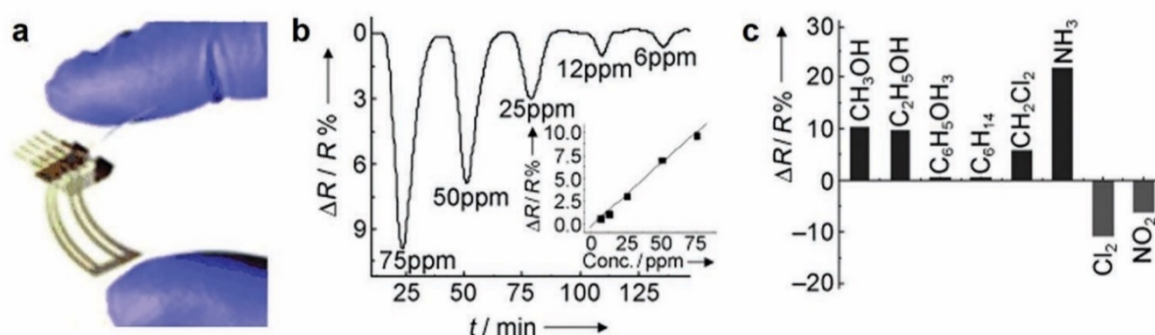


Figure 2.1 Flexisense, inkjet-printed graphene oxide and reduced graphene oxide for gas and vapor concentration detection [38]. (a) All-organic rGO-based flexible chemiresistor; (b) Resistance change versus time plot when the sensor was exposed to Cl_2 vapor; (c) Change in resistance with exposed to other vapor; Reproduced with permission from John Wiley and Sons

Building on Dua et al.'s work, Nikolaou et al. reported inkjet printing GO layers on Shear Horizontal Surface Acoustic Wave (SH-SAW) or known as a Love wave sensor, wherein the performance of this platform enhances the trace-gas detection.⁸⁴ The sensing mechanism for this high performing sensor is dependent on the changes in

electronic gain and the phase of the surface-confined acoustic wave propagation. **Figure 2.2a** displays the inkjet-printed GO coating on Love wave devices with different numbers of inkjet-printed passes (from 1 to 4 printed passes, corresponding to 5–8 devices seen in **Figure 2.2a**). **Figure 2.2b–d** compare the responses of different sensing materials with respect to GO material. Ethanol, toluene and H₂O all show higher response to GO than the other sensing materials studied, such as silica mesoporous, TiO₂ and molecular imprinted polymer. The layer-by-layer study of GO sensing material with the Love wave sensing platform offers a stable and reproducible solution for various gas sensing applications.

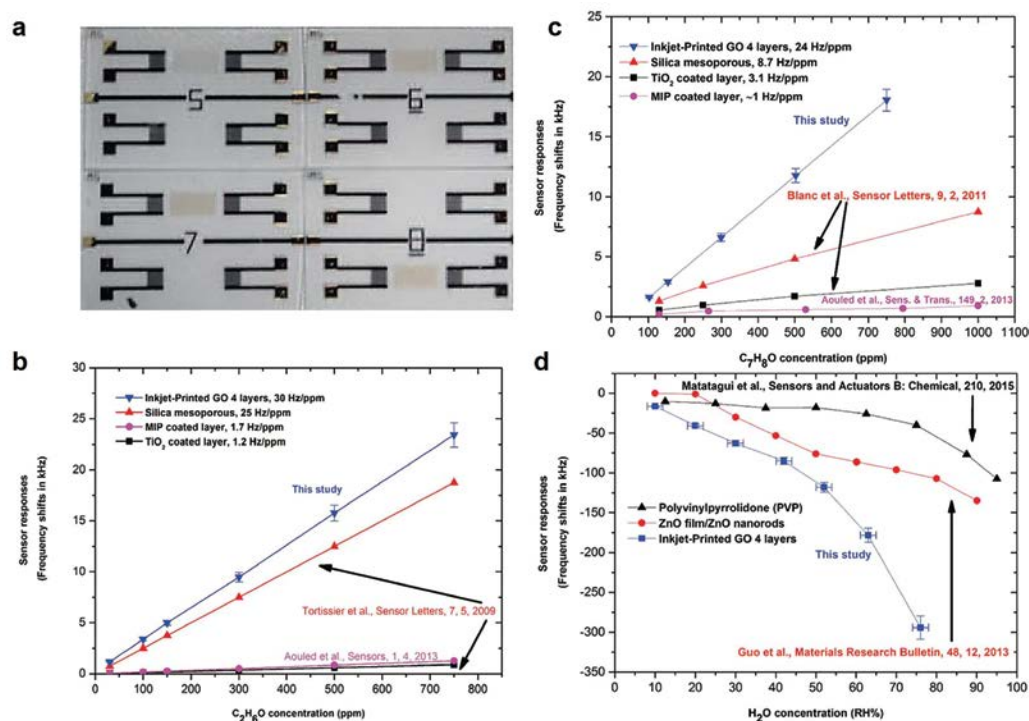


Figure 2.2 (a) Inkjet-printed graphene oxide on LOVE wave device. (b–d) Ethanol (C₂H₆O), toluene (C₇H₈) and H₂O responses respectively, of different sensing layers (GO, ZnO film/ZnO nanorods and PVP) [72]. Reproduced with permission from IEEE.

Moreover, Seekaew et al. reported a low cost and flexible inkjet printed graphene/ PEDOT: PSS composite based gas sensor targeting ammonia.⁸³ Much like with Dua et al.'s work, inkjet printing technique is used to achieve uniform layers over a large area. PEDOT: PSS, a conductive polymer is used with graphene to enhance sensor response and selectivity. **Figure 2.3** captures the essence of the research in its entirety. The figure shows inkjet-printed graphene/ PEDOT:PSS sensing layer on top of the interdigitated screen-printed silver electrode on a flexible and transparent substrate. The figure also shows the excellent selectivity and sensing response time ($S (\%) = \text{percentage change of the gas response}$) of ammonia gas to be in a range of 0.9–3.7% with a low concentration range of 25 to 1000 ppm at room temperature. With the addition of graphene to the PEDOT:PSS, the charge carrier concentration increased, and conduction channels of graphene enhanced the charge transport. The composite of graphene/ PEDOT:PSS based gas/vapor sensor showed much better performance than just PEDOT:PSS as the sensing material. The report suggests that a smooth surface of PEDOT:PSS film could lower the diffusion, and the short penetration depth of gas molecules may be the cause of a decrease in the sensor's performance. Innovative composite materials and the low-cost fabrication technique of this gas sensor would provide a valuable solution to large-scale manufacturing of gas detectors.

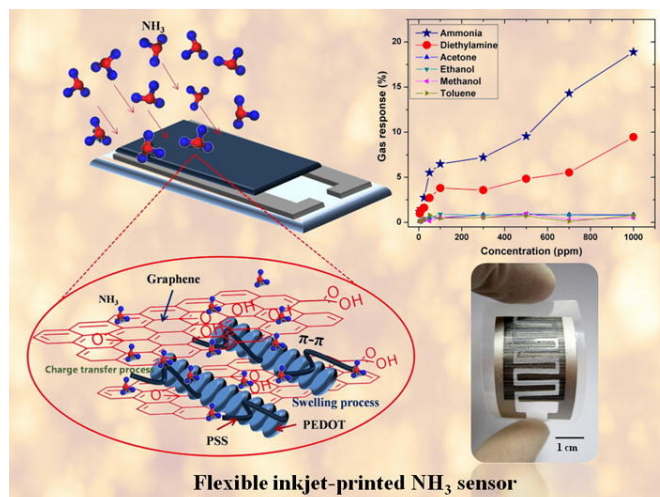


Figure 2.3 Flexible inkjet-printed GO/ PEDOT:PSS composite-based gas sensor for NH₃ detection [84]. Reproduced with permission from Elsevier.

With further fabrication enhancement, Fang et al. and group reported on a flexible, bio-enabled, all inkjet printed, rGO-based vapor sensor on modified Kapton substrate.⁸⁵ **Figure 2.4a** displays an optical image of the fully inkjet-printed rGO-based gas sensor. This work reported a sensing response of 2.5 ppm of dimethylmethylphosphonate (DMMP) vapor in N₂ carrier stream (**Figure 2.4b**). Over 1000 bend cycles, with varying radii of curvature, there were no detectable changes in the conductivity. Furthermore, this group demonstrated that modifying Kapton with polyelectrolyte multilayers (PEMs) significantly reduces the water contact angle and allows for good adhesion for the inkjet printing of the water-based rGO inks.⁸⁶ As a proof of concept, an inkjet-printed water-based rGO sensor on PEMs modified Kapton was fabricated to test the sensitivity of diethyl ethylphosphonate (DEEP) seen in **Figure 2.4c**. This novel approach offers a fully inkjet-printed, flexible, robust and lightweight solution for biosensing applications at room temperature. Herein, we summarized recent developments about inkjet-printed graphene-based gas sensors/vapor detection sensors.

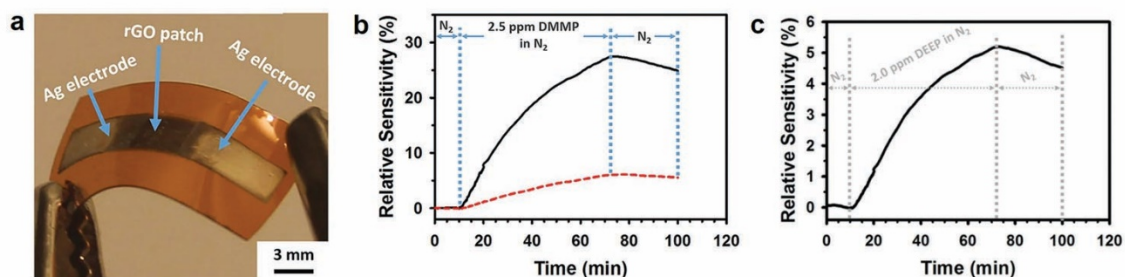


Figure 2.4 (a) Flexible gas sensor, with inkjet-printed reduced graphene oxide (rGO) and silver (Ag) electrodes on treated Kapton. (b,c) Relative sensitivity response to DMMP and DEEP in N₂ gas at room temperature [86,87]. Reproduced with permission from Spring Nature and Royal Society of Chemistry.

2.4 Carbon Nanotubes-Based Gas Sensors

Carbon nanotubes (CNTs) and CNT composites are ideal candidates for gas sensing because of their extremely large surface area to volume ratio making them intrinsically sensitive to any surface perturbations. Consequently, CNTs have been identified to being electrically sensitive to extremely small quantities of gases, electron acceptor and donor molecules such as humidity, oxygen, ammonia, nitrogen oxide and DMMP.^{2,7,43,51,87–91} The sensitivity and selectivity can be further improved easily by suitable chemical functionalization of CNTs e.g. oxygen containing functional groups (-COOH and -OH) at the surface of CNTs lead to much higher response than pristine CNTs^{92,93}. In order to improve upon the sensitivity to specific gases, Starr et al. fabricated an array of CNTFETs with different metal contacts and observed specific transistor response for each FET as a function of metal contacts and target gas.^{94,95} P. Bondavalli et al. demonstrated the use of SWCNT mats as channels for transistors in place of individual SWNTS fabricated with a dynamic spray gun technique to obtain highly controlled SWCNT densities.⁴³ Transistors were fabricated with different metals as S/D electrodes to demonstrate difference in interaction of gases with the metal/SWCNTs junction on the Schottky barrier. However, unlike the classical Schottky barrier between metal and semiconductor, these contacts were

unconventional because the SWCNT were directly deposited on the metal without annealing. This model was originally presented by Yamada et al. for Au/SWCNT contacts.^{96,97} Cui et al. studied the effects of adsorbed gases on the behavior of CNTFETs and showed that the gas molecule adsorption strongly influences metal/SWCNT junction changing the metal electrode work function and thus the fermi level alignment.⁹⁸ These works were all important contributions in understanding the effects of gas adsorption on CNTFETs based gas sensors.

Kong et al. reported one of the earliest works on metal decorated SWCNTs for H₂ sensing.⁹⁹ In their work, Pd was deposited on individual SWCNT by electron beam lithography, resulting in measurable reduction in conductance upon expose to ppm levels of H₂.⁹⁹ In order to obtain high performance from a SWCNT sensor, it is imperative to have a percolative network of semiconducting tubes which are mainly responsible for changes in conductance due to the presence of adsorbed molecules.¹⁰⁰ Hybridization of CNTs with metal nanoparticles, metal oxides, and conducting polymers have shown significant performance improvements.^{101, 102} Several groups have successfully demonstrated integration of CNTs into inkjet printed antenna systems for developing wireless gas sensing modules for detecting gases, such as ammonia and nitrogen dioxide.^{103,104,105} A considerable amount of scientific reports and several excellent reviews on gas sensing properties of CNTs, multiwalled carbon nanotubes (MWNTs), and modified CNTs have been published.^{7,42,87,2} The motivation for this section is to provide the status of inkjet printed carbon nanotube sensors in delivering ideally desired characteristics for gas sensing. In particular, the impact of device geometry, substrate engineering and surface functionalization are discussed. Along with the existing state of

the art, the goal is also to identify key future directions to deepen the fundamental understanding of chemical sensitivity of inkjet printed CNTs and accelerate innovation towards devices/sensors utilizing these materials. For a broader more general review on CNT gas sensors covering other fabrication methods we direct the reader to the review paper by Meyyapan et al.⁷ **Table 2.2** sums up the sensing performance of recent reports on inkjet-printed CNT-based sensors for gas/vapor detection at room temperature.

Table 2.2 Printed carbon nanotube (CNT) gas sensors.

Sensing Material	Printing Method	Target Gas	Detection Range/Sensitivity (Room-Temp)	Reference
MWNT on paper	Plasma Jet	NH ₃	10–60 ppm/4%	[106]
SWNT on acid free paper	Inkjet	NO ₂ , Cl ₂	NO ₂ 250 ppb, Cl ₂ 500 ppb	[107]
SWNT-PABS on paper	Inkjet	NH ₃	250 ppm	[54]
COOH/PEDOT:PSS-MWCNT on PET	Inkjet	C ₂ H ₅ OH	13 ppm	[53]
CNT	Inkjet	DMMP	10 ppm/20%	[76]
SWNT on Kapton	Inkjet	CO ₂	20,000 ppm	[105]
CNT on glass	Inkjet	NH ₄ OH, Ethanol, Acetone	50–1000 ppm	[108][109]
SWNT-COOH on Si	Inkjet	H ₂ S	100 ppm	[110]
Polymer(PVC/Cumene-PSMA/PSE/PVP)—CNTs on PEN	Inkjet	NH ₃	100 ppm/17%	[111]
PABS-SWCNT on paper	Inkjet	NH ₃	50 ppm	[104]
SWCNT on paper	Inkjet	NH ₃	-	[103]
Functionalized CNT on paper	Inkjet	NO ₂	30% at 10 ppm	[112]
SWCNT on Si/SiO ₂	Aerosol jet	NO ₂	96% at 60 ppm	[113]
SWCNT on Si/SiO ₂	Inkjet	NO ₂	5.7% at 10 ppb	[114]
MWCNTs/PEDOT: PSS	Inkjet	HCHO	30% at 10 ppm	[55]
Pt-SWCNTs	Aerosol jet	H ₂	1.5% at 40 ppm	[115]

One of the earliest works on CNT based chemical sensors was reported by Kong et al. for the detection of NH₃ and NO₂.⁹⁰ The individual semiconducting SWNTs (S-SWNTs) were grown by CVD on SiO₂/Si substrates and demonstrated molecular gating effects leading to shifting of fermi level of S-SWNTs thereby modulating the resistance

of the channel by orders of magnitude.⁹⁰ The chosen target gases resulted in two opposite electronic behaviors because of their chemical affinity: NO₂ being an electron-acceptor gas (induced p-type doping of the SWNT) and NH₃ being an electron-donor gas (induced n-type doping). The earliest inkjet printed CNT gas sensor was reported by Jani Mäklin et al. for detecting H₂S gas.¹¹⁰ The active channel material was carboxyl functionalized nanotube film inkjet deposited between Ti/Pt based S/D electrodes with a PECVD grown SiO₂ layer as a gate dielectric. The sensor platform had embedded heating circuit used to reset the sensor for rapid measurements. In this work, both a two terminal resistive and three terminal (p-type) Chem-FET device configuration was fabricated and tested. The Chem-FET sensor operated as p-channel transistor both for air and the H₂S gas with increase/decrease channel conductivity at negative/positive gate bias. It was shown that H₂S vapor induced an increased channel conductivity compared to the reference gas, demonstrating sensing capability of 100 ppm for these sensors. However, an order of magnitude higher change was observed for Chem-FET at low S/D bias and high positive gate bias compared to resistive sensors. The key mechanism was reported to be modulation of junctions between semiconducting and metallic tubes in the network and Schottky barriers between CNTs and metal electrodes. This work highlights the importance of optimum device geometry for improvement of inkjet printed CNT gas sensors. The sensors in this work, however, did not recover reversibly after exposure to vapors was stopped and needed recovery achieved by heating the sensor up to 130 °C with the integrated Pt heating circuit for ~10 min.

The key advance in self-reversible sensors was made by Ammu et al. in demonstrating a reversible sensor for Cl₂ and NO₂ using inkjet-printed CNT films on

cellulosic substrates (and plastics) that did not require thermal or photoirradiation for signal recovery.¹⁰⁷ In this work, NO₂ was detected at concentrations as low as 125 ppb in ambient air for both PET and paper-based devices and the signal self-recovered upon removal of NO₂. The physical mechanism behind this reversible response was attributed to the formation of a weak charge-transfer complex between NO₂ and the CNTs that stops short of irreversible covalent bond formation. The behavior, however, was different for Cl₂ vapors. Both PET and paper-based sensors demonstrated the detection capability of Cl₂ vapor with concentrations as low as 500 ppb. For the PET substrate, the signal response did not recover spontaneously when Cl₂ was removed, and it required additional photoirradiation for ~3 min. Even after this photoirradiation, the signal did not fully recover. However, a key finding was that for Cl₂ detection, paper-based sensors showed reversible operation and self-recovered in ~7min. This was further validated by an irreversible Raman shift for PET-based sensors, which only partially recovered with photoirradiation (**Figure 2.5b**) compared to paper-based sensors (**Figure 2.5a**) that show reversible Raman shift. The authors hypothesized that in the case of Cl₂, with increased residence time, the vapors penetrate the interior of the CNT bundles and/or to the inter-bundle crossover points. This required additional external energy to recover signal or reset the sensor. Since the vapor residence time is significantly reduced on porous cellulosic substrates (as the vapor can desorb from all sides, as opposed to plastic substrates, where desorption is possible only from the top of the film), the paper-based sensors show reversible operation while PET-based sensors were irreversible. This work highlights the importance of substrate engineering for improved inkjet-printed CNT gas

sensors. This work produced fully inkjet-printed and self-reversible sensors which were highly selective to target gases, as shown in **Figure 2.5c**.

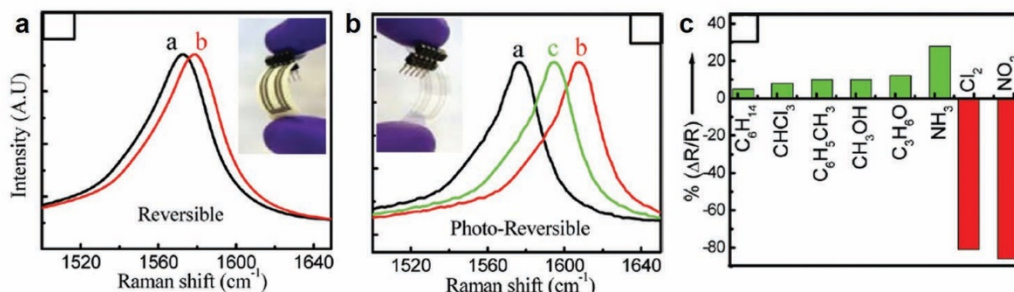


Figure 2.5 Raman shifts before (“a”, black) and after (“b”, red) exposure to 100 ppm Cl_2 vapor for (a) inkjet-printed CNT/PET, where the shift is partially reversible upon photoirradiation (to “c”, green); (b) inkjet-printed CNT/paper, where the shift is reversible. (c) Selectivity plot for an inkjet-printed CNT/PET film, sensor exposed to saturated organic vapors, NH_3 (100 ppm), NO_2 (100 ppm), and Cl_2 (100 ppm). Reproduced with permission from American Chemical Society [107].

One promising direction to improve the sensitivity and selectivity of CNT based sensors is in the functionalization of CNTs with different chemical groups, metal nanoparticles and organic molecules^{93, 101, 102}. A recent experiment by Alshammari et al. shows the strong influence of functionalization on device performance.⁵³ In this work, three different CNT channels were investigated: (a) pristine CNTs with no functionalization; (b) CNTs functionalized with carboxylic acid (O-CNTs) and CNTs functionalized with conductive polymer PEDOT: PSS(P-CNTs). The method of fabrication and final inkjet-printed sensors are shown in **Figure 2.6a–f**. The sensitivity and the response time of the sensor for different functionalizations are shown in **Figure 2.6g**. Functionalization with carboxylic acid results in 1.7× enhancement in sensitivity compared to pristine CNTs while that with PEDOT:PSS results in 2.53× improvement in sensitivity. Similarly, Huang et al., demonstrated inkjet-printed NH_3 gas sensors based on CNTs functionalized with poly (m-aminobenzene sulfonic acid) (PABS). **Figure 2.7**

shows the measurement setup and sensor response with a sensitivity of 10 ppm with these functionalized CNT based NH_3 sensors on paper.⁵⁴ The sensor followed a step response, with a fast response time ($\sim 3\text{sec}$), was reversible and stable in outdoor environments for up to 3 months. Similarly Timsorn et al.⁵⁵ demonstrated the impact of functionalization by fabricating a highly sensitive and extremely selective MWNTS-PEDOT:PSS-based sensor for formaldehyde in concentration range of 10–200 ppm at room temperature for food monitoring applications. The enhanced response in the nano-composite network-based sensors are the result of combining the sensing properties of both the constituent materials. The conducting polymers such as PEDOT PSS offer additional vapor attachment sites to the CNT network and also help in obtaining rapid response rates. This is because of the weak interaction between polymers and vapor molecules which can be easily desorbed upon exposure to air flow. Similarly, the performance enhancement in carboxyl-functionalized nanotubes is because oxygen is more electronegative than carbon and attracts more electrons from electron donating vapors like ethanol, contributing to an increased change in the resistance of the sensor networks and improved sensitivity.

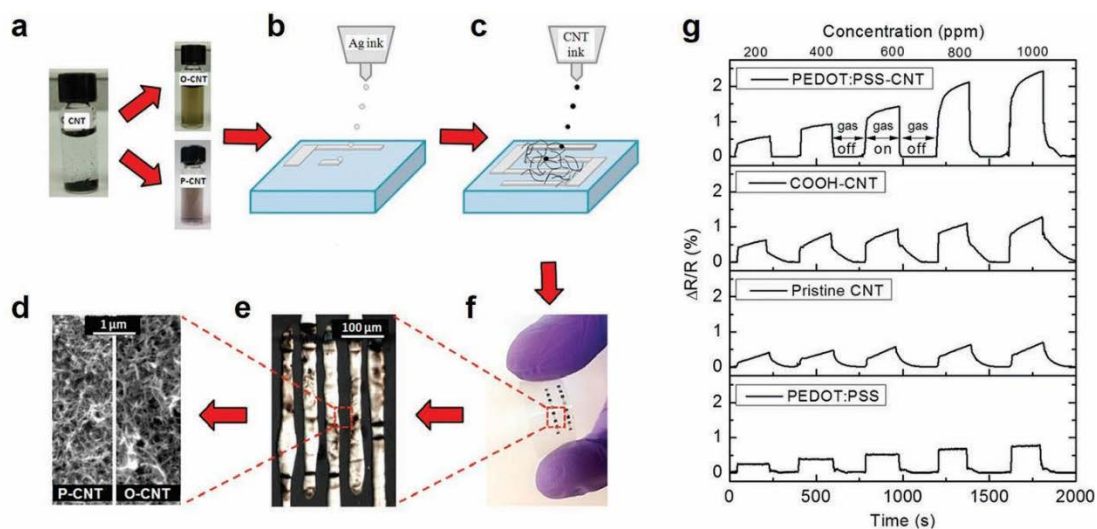


Figure 2.6 Fully printed and flexible CNTs based gas sensor: (a) CNTs' functionalization with carboxylic acid (O-CNTs) and PEDOT:PSS (P-CNTs); (b) printing of Ag electrodes; (c) printing of CNTs; (d) photograph of the sensor on flexible substrate; (e) optical microscope image shows the printed silver interdigitated electrodes and (f) SEM image shows the printed carbon nanotubes. (g) Sensitivity of the printed ethanol vapor sensor (operated at 5V) with different CNTs functionalization methods and different gas concentrations. Reproduced with permission from Elsevier [53].

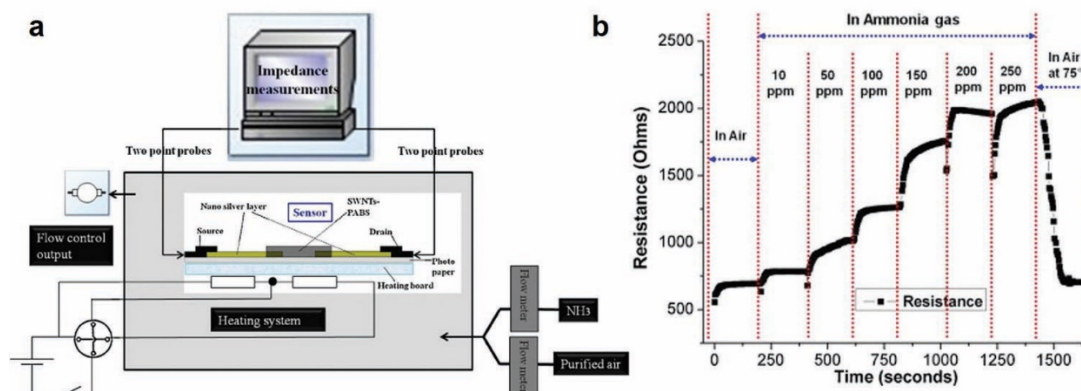


Figure 2.7 (a) Measurement setup for paper-based sensors with silver and inkjet-printed SWNT-PABS. (b) Resistance of paper-based sensor exposed to different concentrations of NH_3 . Reproduced with permission from Elsevier [54].

2.5 Role of Defects

2.5.1 Graphene-Based sensors

Graphene has proven to be an excellent nanomaterial for application in chemical sensing, and the fundamental sensing performance is greatly affected by the role of defects that are induced by various fabrication processes. There have been several groups that have extensively studied the role of defects on the sensing mechanism of the graphene-based devices.^{18–20,27,31,36,116–122} Defects such as film thickness, crystalline structure, porosity, wrinkles, grain boundaries, and external substrate defects all greatly affect the sensing performance of the sensor.^{19,20,22,23,74,75,119,123}

To explore these point and linear defects, Salehi-Khojin et al. demonstrated sensing performance of polycrystalline graphene ribbons compared to nearly pristine graphene.²² CVD fabricated graphene ribbons displayed higher sensitivity than of the pristine graphene due to the linear defects that are present, allowing for easy conduction pathways. Engineering line defects and edges allows for improved sensitivity for graphene-based sensor. Moreover, Banerjee et al. and his team studied the electrochemical performance at the edge of the graphene nanopores fabricated by a TEM electron beam, isolated from the electrochemical contributions of the basal plane.²³ They observed that the electrochemical current densities were 3x higher than those reported for CNTs and for pristine graphene. Manufacturing arrays of these nanopores could allow for superior sensing performance of gas sensors. Kumar et al.'s research shows that the defective CVD graphene-based gas sensors control the sensing characteristic of the device.¹⁹ Moreover, their study showed that the defects on the SiO₂ substrate were needed to modulate the electrical properties and are responsible for the sensing

characteristics of the pristine graphene chemFETs. Another paper by Salehi-Khojin et al. analysed the sensing performance of surfactant-assisted exfoliated graphene chemiresistor.¹⁸ The sensing performance of the randomly stacked graphene flakes was characterized by controlling the filtration volume seen in **Figure 2.8**. The low filtration volume of the randomly stacked graphene flake sensor showed excellent sensitivity response, while the increase in filtration volume decreased in sensitivity as the electric transport regime switched from 2D electron hopping to phonon-limited (metallic) conduction. This sensor performed superiorly compared to other sensing materials such as polycrystalline graphene, graphene microribbon, and CNT-based chemical sensors. The review paper by Carbone et al. discussed that for graphene inks for inkjet printing, defects of different types are induced from the dispersing and stabilizing agents.¹²⁴ The dispersant and the stabilizing agents reduce the conductivity in the oxygenated species. Improvement regarding non-graphene components, such as using a proper conductivity polymer or even starch in the ink solution, tends to promote the performance of the overall sensor.⁷⁴

While the focus is to create defect-free nanomaterials, the next goal is to control/make defects in the materials (e.g., pores, edges, or replacing atoms) to self-repair, or engineer materials for catalytic or selectivity applications.^{117,125-127} Zang et al., and their group demonstrated how defective graphene showed much stronger adsorption of different gas vapors than in pristine graphene.¹²⁷ Hajati et al. improved sensing in graphene material by gently inducing defects (reconstructed vacancies) in the lattice. This defect-controlled technique by Ga⁺ ion irradiation ($\sim 10^{12}$ ions cm⁻²) allows for improvements in transport properties in the graphene layer, in turn improving sensing and

response time.¹²⁸ These studies showed that the defects induced by morphology, fabrication and different substrates play a significant role in sensing performance.

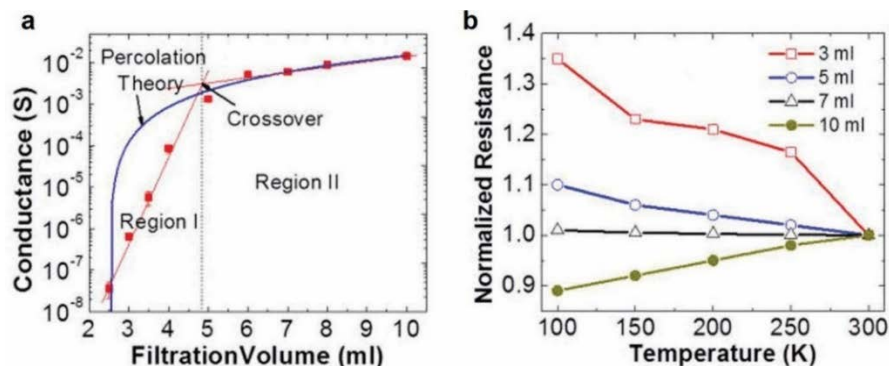


Figure 2.8 (a) Conductance (S) vs. filtration volume (mL) for the randomly stacked graphene flakes. (b) Normalized resistance vs. temperature (K) for various filtration volumes from 3 to 10 mL [18]. Reproduced with permission from AIP Publishing.

2.5.2 CNT-Based Sensors

The pristine intrinsic properties of CNTs can be perturbed at various stages of the ink synthesis and printing process, for example during colloid formation, chemical functionalization, and oxidation. As such, a fundamental understanding of the impact of the defects on changes in CNT properties and corresponding change in sensing properties is imperative to designing CNT gas sensors. The sensing mechanism in CNTs can be explained according to interactions over three sections—along the length of tubes, at the junction between the tubes, or at the junction between the nanotubes and metal contacts, as shown in **Figure 2.9a**⁴². Fuhrer et al., proved that the contact resistance at the metal semiconducting junctions was two orders of magnitude larger than the resistance between two semiconducting or metallic SWCNTs, resulting in the current flowing preferably through either semiconducting or metallic tubes.¹²⁹ Khojin et al., did numerical computations and experiments to determine the change in the sensing mechanism of the

chemiresistor upon addition of defects in the nanotubes.⁴⁴ They showed that in the case of perfect nanotubes, since the resistance of tubes is very small, the overall response of the chemiresistor mainly depends on the resistance changes at the junctions between the nanotubes as well as at the metal contacts to nanotubes junctions. Meanwhile, in the case of highly defective nanotubes, the resistance of the tubes is very high. Therefore, the overall sensor response is dominated by the resistance changes at the tubes themselves as compared to the other junctions. The key conclusion was that the main sensing mechanism is dependent on and changes according to the level of defects on the nanotubes, as shown in **Figure 2.9b,c**.

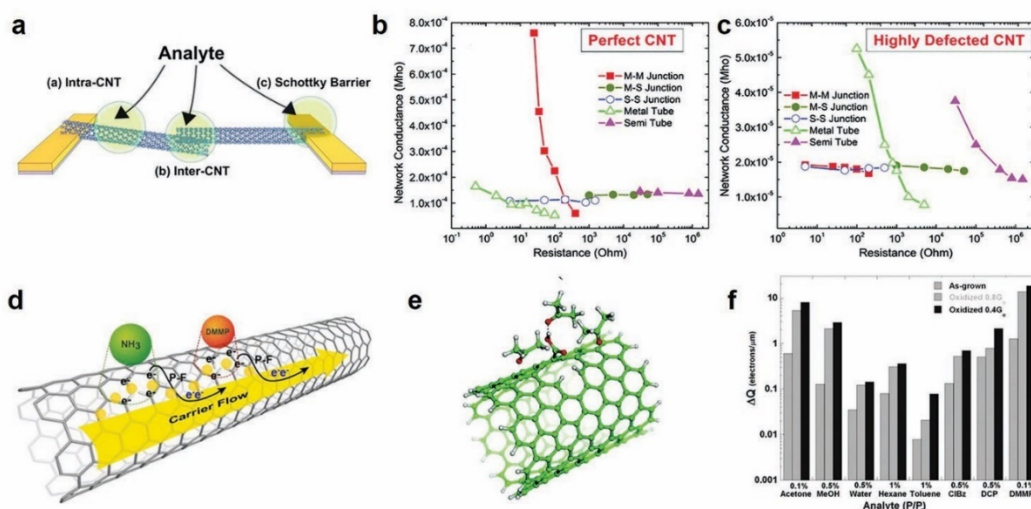


Figure 2.9 (a) Sensing mechanism in CNTs. Reproduced with permission from American Chemical Society [42]. (b) Calculations of the effects of changes in the components of the resistance on the overall resistance of the networks for perfect nanotubes and (c) defective nanotubes. Reproduced with permission from American Chemical Society [44]. (d) Detrapping mechanism of accumulated charges at the nanotube defects in PF regime. Reproduced with permission from AIP Publishing [131] (e) Clustering of acetone around the defect via intermolecular bonding. (f) Charge transfer between various analytes and the SWNT network as a function of oxidation. Reproduced with permission from American Chemical Society [132].

In another work, Khojin et al., showed that the conduction mechanism in the nanotubes is also related to the amount of defects.¹³⁰ They did measurements to show that at

high electric fields, the Poole Frenkel mode of conduction dominates, wherein the electrons tunnel through the defects leading to an injection of trapped charge carriers in the conduction band resulting in a higher response¹³⁰. In other words, the Poole Frenkel regime effectively samples the defects, leading to higher sensitivity, as shown in **Figure 2.9d**. To understand and quantify the impact of defects on the overall sensitivity, Robinson et al. controllably introduced carboxylic acid sites through oxidation on the SWNTs (<2% of the total sites) and studied the impact on sensor response over a wide variety of gas vapors.¹³¹ The samples that received more oxidation (0.4 G0) showed an enhanced response compared to samples with less oxidation (0.8 G0). An increase in both the capacitance and conductance response for a broad spectrum of analytes on SWNT was observed. The physical mechanism was attributed to defect sites serving as both low energy adsorption sites and nucleation sites for additional condensation of the gas species on CNT surface, as shown in **Figure 2.9e–f**. Once the analyte adsorbs at a defect site, charge transfer takes place between the analyte and CNTs, resulting in the resistance change. These works highlight a more general role of defects in sensing a wide variety of analytes and their implication on the design of printed gas sensors using carbon nanotubes.

2.6 Advanced Printing Techniques

In this section (Advanced Printing Techniques), we review the other state-of-the-art print modalities that are also being actively employed for printing gas sensors.

2.6.1 Aerosol-Jet Printing

Aerosol jet printing (AJP) is another relatively new method of printing where the droplet size is much smaller than that of inkjet printing, resulting in finer features and

higher resolution. AJP introduces new direct write capabilities with consistent deposition, allows a wider range of ink viscosities (1 to 1000cP) and finer feature resolution ($\sim 10\mu\text{m}$). A typical AJP system consists of two modes of aerosolization: pneumatic and ultrasonic. The ultrasonic atomizer and the multi-axis positioning stage enables conformal printing on non-planar surfaces, such as on a golf ball. AJP allows for rapid integration when compared to other additive technologies.¹³² However, AJP requires tuning of several parameters, such as gas flow (or sheath gas N_2), nozzle diameter, stage speed and substrate temperature, to achieve optimal print resolution. Therefore, it has been a challenge to print CNTs with AJP successfully. In an earlier work, Liu et al. successfully demonstrated Pt functionalized SWNTs printed with AJP towards 40ppm H_2 detection without coffee ring effect in the printed structures with N_2 for carrier gas.¹¹⁵ A recent work by Liang et al. further optimized the process and demonstrated high print resolution for alignment of CNTs for flexible electronics applications using AJP.¹³³

In a novel technique, Zhou et al. demonstrated a highly efficient method of sorting semiconducting nanotubes by a new isoindigo-based copolymer to act as channel material to construct aerosol jet printed (with N_2 carrier gas) thin film transistors (TFTs) on Si/SiO_2 substrates.¹¹³ TFTs based on these sorted semiconducting SWNTs showed superior device performance with high on/off ratios ($10^6:1$) and mobility (up to $29.8 \text{ cm}^2 \text{ V}^{-1} \text{ s}^{-1}$) and small hysteresis. Gas sensors based on above TFTs exhibited one of the best performances reported for NO_2 sensors at room temperature with respect to sensitivity, stability and response rate.

In our research, we investigated power dissipation and electrical breakdown in aerosol jet printed graphene (with N_2 carrier gas) interconnects on Kapton, SiO_2/Si , and

Al₂O₃ substrates.¹³⁴ Our study indicated that the power dissipation in AJP graphene is dominated by the graphene interconnect morphology for high thermal conductivity substrates, but can be limited by the substrate properties. Furthermore, our study showed that the porosity of the AJP printed graphene induces a high thermal resistance of the graphene interconnects. An AJP printed (N₂ carrier gas) metal oxide gas sensor reported by Cho et al. exhibits good sensitivity and fast response time (1.2 seconds).¹³⁵ Although, to our knowledge, there haven't been any reports on AJP printed graphene- or CNT-based gas sensors thus far.

2.6.2 Plasma-Jet printing

Although inkjet printing is a promising route towards printed CNT and graphene gas sensors, there are a few shortcomings including rigorous ink synthesis, nozzle clogging and the need for post-printing thermal treatment to remove dispersants (solvents, surfactants). Plasma jet printing (PJP) has shown promise in overcoming these challenges by enabling deposition of an aerosol at atmospheric pressure and at under 40 °C with no postprocessing required.¹⁰⁶ The setup for plasma jet printing is shown in **Figure 2.10a**. The printer consists of a quartz nozzle (diameter 5 mm) containing two copper electrodes (~2 cm apart) and connected to a high-voltage (1 to 15 kV AC power supply).¹⁰⁶ A helium plasma is generated upon applying a potential between the electrodes. An ultrasonic nebulizer is used to atomize the colloidal material to create aerosol to be deposited. This aerosol is then carried to the print nozzle by a helium carrier gas into a quartz tube which contains the plasma. While the primary gas flow is at 2000 ccm, the secondary flow into the nebulization is at 50 ccm to aid in the transportation of the aerosol to the print head. The operation of the system with a fixed aerosol flow is shown

in **Figure 2.10b** (plasma off) and **Figure 2.10c** (plasma on). This work used commercial MWCNTs and carboxyl functionalization to form the colloidal ink for plasma jet printing. The printed carbon nanotubes on paper showed a detection limit of 10 ppm towards NH_3 (**Figure 2.10d**) and this work shows a promising direction for plasma jet printing for room temperature gas sensing. Moreover, PJP has shown potential to enhance conductivity in GO films by using a low-temperature He and H_2 gas mixture to reduce a highly acidic GO suspension ($\text{pH} < 2$) in situ during deposition confirmed by XPS and NEXAFS (near-edge X-ray absorption fine structure spectroscopy). The reduction of carboxylic acid functional groups with the extended exposure to the plasma jet aids in yielding conductive GO patterns useful in gas sensing applications.¹³⁶

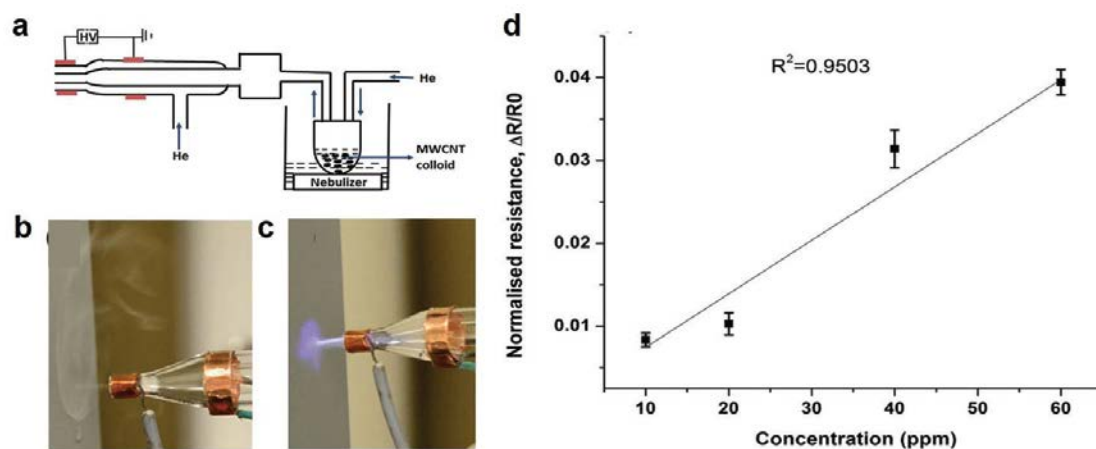


Figure 2.10 (a) Schematic of the atmospheric plasma jet. Photographs of aerosol flow with (b) no plasma and (c) plasma on. (d) MWCNTs on paper as a gas sensor exposed to ammonia in the range of 10–60 ppm. Reproduced with permission from AIP Publishing [106].

2.7 Outlook

The market for gas sensors is predicted to exceed USD 3 billion by 2027.¹³⁷ There are innumerable applications for gas sensors ranging from environmental monitoring, wearable products, smart packaging of perishable food products, RFID tags and healthcare monitoring.^{111,138-143} The motivation for making them flexible is to potentially increase the application areas of these sensors. Additive manufacturing techniques, such as inkjet printing allow for large scale, low cost, portable sensor fabrication, without generating a lot of hazardous chemical waste as compared to traditional fabrication methods. Moreover, additive manufacturing allows for enhancing sustainability by using the resources efficiently and enable closed-loop material flows.¹⁴⁴ The inkjet printing method is less complex and provides higher throughput of devices than other traditional methods of fabricating sensors. The recent number of publications in the area of inkjet-printed graphene and carbon nanotube-based gas sensors shows an exponential rise, and thus needs further research.

2.8 Conclusion

Although CNT- and graphene-based gas sensors demonstrate great potential for next-generation printable and flexible sensing materials, several challenges remain before feature resolution and gas sensitivities can be compared to the conventional vacuum-based fabrication process. Many efforts to improve the inkjet printing process of CNTs and graphene for gas sensing applications are made by decorating CNTs or graphene with conductive oxides, polymers, or metals, improving the rheology of the ink, and substrate surface modification. With ongoing research in the area of ink synthesis, tuning printing

process, and development of new printing methods, printed CNT- and graphene-based sensors will soon offer better control and resolution.

2.9 Acknowledgements

Author Contributions: D.E. and H.S. conceived the idea of the work. T.P. investigated graphene-based gas sensors and A.C. worked on carbon-nanotubes-based gas sensors.

T.P and A.C worked on investigating research on other printing techniques and role of defects. All authors made substantial contributions in editing of the manuscript.

Funding: This research was funded by NASA EPSCoR, #ID-80NSSC17M0029.

Acknowledgments: D.E. also acknowledges career development support by Institutional Development Awards (IDeA) from the National Institute of General Medical Sciences of the National Institutes of Health under Grants #P20GM103408 and P20GM109095

Conflicts of Interest: The authors declare no conflict of interest.

2.10 References

1. Lee, D. D. Environmental gas sensors. *IEEE Sens. J.* (2001). doi:10.1109/JSEN.2001.954834
2. Yeow, J. T. W. & Wang, Y. A review of carbon nanotubes-based gas sensors. *Journal of Sensors* (2009). doi:10.1155/2009/493904
3. Kohl, D. Function and applications of gas sensors. *Journal of Physics D: Applied Physics* (2001). doi:10.1088/0022-3727/34/19/201
4. Korotcenkov, G. *Handbook of Gas Sensor Materials. Book* (2014). doi:10.1007/978-1-4614-7388-6
5. James, D., Scott, S. M., Ali, Z. & O'Hare, W. T. Chemical sensors for electronic nose systems. *Microchimica Acta* (2005). doi:10.1007/s00604-004-0291-6
6. Yang, S., Jiang, C. & Wei, S. huai. Gas sensing in 2D materials. *Applied Physics Reviews* (2017). doi:10.1063/1.4983310

7. Meyyappan, M. Carbon Nanotube-Based Chemical Sensors. *Small* **12**, 2118–29 (2016).
8. Ryabtsev, S. V., Shaposhnick, A. V., Lukin, A. N. & Domashevskaya, E. P. Application of semiconductor gas sensors for medical diagnostics. *Sensors Actuators, B Chem.* (1999). doi:10.1016/S0925-4005(99)00162-8
9. Wang, T. *et al.* A Review on Graphene-Based Gas/Vapor Sensors with Unique Properties and Potential Applications. *Nano-Micro Letters* (2016). doi:10.1007/s40820-015-0073-1
10. Basu, S. & Bhattacharyya, P. Recent developments on graphene and graphene oxide based solid state gas sensors. *Sensors and Actuators, B: Chemical* (2012). doi:10.1016/j.snb.2012.07.092
11. Pumera, M. *et al.* Graphene for electrochemical sensing and biosensing. *TrAC - Trends Anal. Chem.* **29**, 954–965 (2010).
12. Chen, D. *et al.* Graphene-based materials in electrochemistry. *Chem. Soc. Rev.* **39**, 3157 (2010).
13. Cinti, S. & Arduini, F. Graphene-based screen-printed electrochemical (bio)sensors and their applications: Efforts and criticisms. *Biosensors and Bioelectronics* **89**, 107–122 (2017).
14. Amin, K. R. & Bid, A. Graphene as a sensor. *Curr. Sci.* **107**, 430–436 (2014).
15. Shao, Y. *et al.* Graphene based electrochemical sensors and biosensors: A review. *Electroanalysis* **22**, 1027–1036 (2010).
16. Meyyappan, M. *et al.* Nanoelectronics and nanosensors for space exploration. *MRS Bull.* **40**, 822–828 (2015).
17. Schedin, F. *et al.* Detection of individual gas molecules adsorbed on graphene. *Nat. Mater.* **6**, 652–655 (2007).
18. Salehi-Khojin, A. *et al.* Chemical sensors based on randomly stacked graphene flakes. *Appl. Phys. Lett.* 9–12 (2012).
19. Kumar, B. *et al.* The role of external defects in chemical sensing of graphene field-effect transistors. *Nano Lett.* **13**, 1962–1968 (2013).
20. Grosse, K. L. *et al.* Direct observation of resistive heating at graphene wrinkles and grain boundaries. *Appl. Phys. Lett.* **105**, (2014).

21. Bae, M. H., Ong, Z. Y., Estrada, D. & Pop, E. Imaging, simulation, and electrostatic control of power dissipation in graphene devices. *Nano Lett.* **10**, 4787–4793 (2010).
22. Salehi-Khojin, A. *et al.* Polycrystalline graphene ribbons as chemiresistors. *Adv. Mater.* **24**, 53–57 (2012).
23. Banerjee, S. *et al.* Electrochemistry at the edge of a single graphene layer in a nanopore. *ACS Nano* **7**, 834–43 (2013).
24. Zhu, Y. *et al.* Graphene and graphene oxide: Synthesis, properties, and applications. *Adv. Mater.* **22**, 3906–3924 (2010).
25. Stankovich, S. *et al.* Synthesis of graphene-based nanosheets via chemical reduction of exfoliated graphite oxide. *Carbon N. Y.* **45**, 1558–1565 (2007).
26. Ciesielski, A. & Samorì, P. Graphene via sonication assisted liquid-phase exfoliation. *Chem. Soc. Rev.* **43**, 381–98 (2014).
27. Paton, K. R. *et al.* Scalable production of large quantities of defect-free few-layer graphene by shear exfoliation in liquids. *Nat. Mater.* **13**, 624–30 (2014).
28. Bae, S. *et al.* Roll-to-roll production of 30-inch graphene films for transparent electrodes. *Nat. Nanotechnol.* **5**, 574–578 (2010).
29. Bao, J. *et al.* Synthesis of Freestanding Graphene on SiC by a Rapid-Cooling Technique. *Phys. Rev. Lett.* **117**, 205501 (2016).
30. Wu, Y. *et al.* High-frequency, scaled graphene transistors on diamond-like carbon. *Nature* **472**, 74–78 (2011).
31. Coleman, J. N. Liquid exfoliation of defect-free graphene. *Acc. Chem. Res.* **46**, 14–22 (2013).
32. Dikin, D. A. *et al.* Preparation and characterization of graphene oxide paper. *Nature* (2007). doi:10.1038/nature06016
33. Moon, I. K., Lee, J., Ruoff, R. S. & Lee, H. Reduced graphene oxide by chemical graphitization. *Nat. Commun.* (2010). doi:10.1038/ncomms1067
34. Llobet, E. Gas sensors using carbon nanomaterials: A review. *Sensors and Actuators, B: Chemical* (2013). doi:10.1016/j.snb.2012.11.014

35. Huang, L. *et al.* Fully Printed, Rapid-Response Sensors Based on Chemically Modified Graphene for Detecting NO₂ at Room Temperature. *ACS Appl. Mater. Interfaces* **6**, 7426–7433 (2014).
36. Vedala, H., Sorescu, D. C., Kotchey, G. P. & Star, A. Chemical sensitivity of graphene edges decorated with metal nanoparticles. *Nano Lett.* (2011). doi:10.1021/nl2006438
37. Lu, G., Ocola, L. E. & Chen, J. Reduced graphene oxide for room-temperature gas sensors. *Nanotechnology* (2009). doi:10.1088/0957-4484/20/44/445502
38. Dua, V. *et al.* All-organic vapor sensor using inkjet-printed reduced graphene oxide. *Angew. Chemie - Int. Ed.* **49**, 2154–2157 (2010).
39. Meng, F. L., Guo, Z. & Huang, X. J. Graphene-based hybrids for chemiresistive gas sensors. *TrAC - Trends in Analytical Chemistry* (2015). doi:10.1016/j.trac.2015.02.008
40. Toda, K., Furue, R. & Hayami, S. Recent progress in applications of graphene oxide for gas sensing: A review. *Analytica Chimica Acta* (2015). doi:10.1016/j.aca.2015.02.002
41. Eatemadi, A. *et al.* *Carbon nanotubes: properties, synthesis, purification, and medical applications.* (2014). doi:10.1186/1556-276X-9-393
42. Schroeder, V., Savagatrup, S., He, M., Lin, S. & Swager, T. M. Carbon nanotube chemical sensors. *Chemical Reviews* **119**, 599–663 (2019).
43. Bondavalli, P., Gorintin, L., Feugnet, G., Lehoucq, G. & Pribat, D. Selective gas detection using CNTFET arrays fabricated using air-brush technique, with different metal as electrodes. *Sensors Actuators, B Chem.* (2014). doi:10.1016/j.snb.2014.06.064
44. Salehi-Khojin, A. *et al.* On the sensing mechanism in carbon nanotube chemiresistors. *ACS Nano* **5**, 153–158 (2011).
45. Arora, N. & Sharma, N. N. Arc discharge synthesis of carbon nanotubes: Comprehensive review. *Diamond and Related Materials* **50**, 135–150 (2014).
46. Bonaccorso, F. *et al.* Pulsed laser deposition of multiwalled carbon nanotubes thin films. *Appl. Surf. Sci.* **254**, 1260–1263 (2007).

47. Kumar, M. & Ando, Y. Chemical vapor deposition of carbon nanotubes: A review on growth mechanism and mass production. *Journal of Nanoscience and Nanotechnology* **10**, 3739–3758 (2010).
48. Dai, H. Nanotube Growth and Characterization. in *Carbon Nanotubes* 29–53 (Springer Berlin Heidelberg, 2007). doi:10.1007/3-540-39947-x_3
49. Kharlamova, M. V. *et al.* Separation of Nickelocene-Filled Single-Walled Carbon Nanotubes by Conductivity Type and Diameter. *Phys. Status Solidi Basic Res.* (2017). doi:10.1002/pssb.201700178
50. Chernov, A. I. & Obraztsova, E. D. Density gradient ultra-centrifugation of arc produced single-wall carbon nanotubes. *J. Nanoelectron. Optoelectron.* (2009). doi:10.1166/jno.2009.1027
51. Tortorich, R. P. & Choi, J.-W. Inkjet Printing of Carbon Nanotubes. *Nanomaterials* **3**, 453–468 (2013).
52. Byun, K., Subbaraman, H., Lin, X., Xu, X. & Chen, R. T. *A 3 μ m Channel, Ink-Jet Printed CNT-TFT for Phased Array Antenna Applications.*
53. Alshammari, A. S., Alenezi, M. R., Lai, K. T. & Silva, S. R. P. Inkjet printing of polymer functionalized CNT gas sensor with enhanced sensing properties. *Mater. Lett.* **189**, 299–302 (2017).
54. Huang, L. *et al.* A novel paper-based flexible ammonia gas sensor via silver and SWNT-PABS inkjet printing. *Sensors Actuators, B Chem.* **197**, 308–313 (2014).
55. Timsorn, K. & Wongchoosuk, Chatchawal. Inkjet printing of room-temperature gas sensors for identification of formalin contamination in squids. *J. Mater. Sci. Mater. Electron.* **30**, 4782–4791 (1234).
56. Singh, M., Haverinen, H. M., Dhagat, P. & Jabbour, G. E. Inkjet printing-process and its applications. *Adv. Mater.* **22**, 673–685 (2010).
57. Deiner, L. J. & Reitz, T. L. Inkjet and aerosol jet printing of electrochemical devices for energy conversion and storage. *Advanced Engineering Materials* **19**, (2017).
58. Sridhar, a, Blaudeck, T. & Baumann, R. Inkjet Printing as a Key Enabling Technology for Printed Electronics. *Mater. Matters* **6**, 1–8 (2009).

59. Cummins, G. & Desmulliez, M. P. Y. Inkjet printing of conductive materials: A review. *Circuit World* (2012). doi:10.1108/03056121211280413
60. Tekin, E., Smith, P. J. & Schubert, U. S. Inkjet printing as a deposition and patterning tool for polymers and inorganic particles. *Soft Matter* (2008). doi:10.1039/b711984d
61. Sun, J. *et al.* Fabricating High-Resolution Metal Pattern with Inkjet Printed Water-Soluble Sacrificial Layer. *ACS Appl. Mater. Interfaces* (2020). doi:10.1021/acsami.0c01138
62. Nguyen, P. Q. M., Yeo, L. P., Lok, B. K. & Lam, Y. C. Patterned surface with controllable wettability for inkjet printing of flexible printed electronics. *ACS Appl. Mater. Interfaces* (2014). doi:10.1021/am4054546
63. Editorial. 2D materials. *Nat. Photonics* **10**, 201–201 (2016).
64. Geim, A. K. & Novoselov, K. S. The rise of graphene. *Nat. Mater.* **6**, 183–191 (2007).
65. Castro Neto, A. H., Guinea, F., Peres, N. M. R., Novoselov, K. S. & Geim, A. K. The electronic properties of graphene. *Rev. Mod. Phys.* **81**, 109–162 (2009).
66. Le, T. *et al.* A novel graphene-based inkjet-printed WISP-enabled wireless gas sensor. in *2012 42nd European Microwave Conference* 412–415 (IEEE, 2012). doi:10.23919/EuMC.2012.6459158
67. Cho, B. *et al.* Graphene-based gas sensor: Metal decoration effect and application to a flexible device. *J. Mater. Chem. C* (2014). doi:10.1039/c4tc00510d
68. Paul, R. K., Badhulika, S., Saucedo, N. M. & Mulchandani, A. Graphene nanomesh as highly sensitive chemiresistor gas sensor. *Anal. Chem.* (2012). doi:10.1021/ac3012895
69. Latif, U. & Dickert, F. L. Graphene hybrid materials in gas sensing applications. *Sensors (Switzerland)* (2015). doi:10.3390/s151229814
70. Pearce, R. *et al.* Epitaxially grown graphene based gas sensors for ultra sensitive NO₂ detection. *Sensors Actuators, B Chem.* (2011). doi:10.1016/j.snb.2010.12.046
71. Choi, W. & Alwarappan, S. Graphene-Based Biosensors and Gas Sensors. in *Graphene* (2018). doi:10.1201/b11259-11

72. Yoon, H. J. *et al.* Carbon dioxide gas sensor using a graphene sheet. *Sensors Actuators, B Chem.* **157**, 310–313 (2011).
73. Singh, E., Meyyappan, M. & Nalwa, H. S. Flexible Graphene-Based Wearable Gas and Chemical Sensors. *ACS Appl. Mater. Interfaces* **9**, 34544–34586 (2017).
74. Peregrino, P. P. *et al.* Starch-Mediated Immobilization, Photochemical Reduction, and Gas Sensitivity of Graphene Oxide Films. *ACS Appl. Mater. Interfaces* (2020). doi:10.1021/acsomega.9b03892
75. da Silva, M. F. P. *et al.* Synthesis and characterization of GO-H₃BO₃ composite for improving single-sensor impedimetric olfaction. *J. Mater. Sci. Mater. Electron.* (2020). doi:10.1007/s10854-020-04004-3
76. Hester, J. G. D., Tentzeris, M. M. & Fang, Y. Inkjet-printed, flexible, high performance, carbon nanomaterial based sensors for ammonia and DMMP gas detection. in *European Microwave Week 2015: 'Freedom Through Microwaves', EuMW 2015 - Conference Proceedings; 2015 45th European Microwave Conference Proceedings, EuMC* (2015). doi:10.1109/EuMC.2015.7345899
77. Nguyen, B. H., Nguyen, V. H., Nguyen Bich, H. & Nguyen Van, H. Promising applications of graphene and graphene-based nanostructures. *Adv. Nat. Sci. Nanosci. Nanotechnol.* **7**, (2016).
78. Travan, C. & Bergmann, A. NO₂ and NH₃ Sensing Characteristics of Inkjet Printing Graphene Gas Sensors. *Sensors* **19**, 3379 (2019).
79. Andò, B. *et al.* An inkjet printed CO₂ gas sensor. *Procedia Eng.* **120**, 628–631 (2015).
80. Bozzi, M. *et al.* Inkjet-printed antennas, sensors and circuits on paper substrate. *IET Microwaves, Antennas Propag.* **7**, 858–868 (2013).
81. Le, T., Lakafosis, V., Lin, Z., Wong, C. P. & Tentzeris, M. M. Inkjet-printed graphene-based wireless gas sensor modules. in *2012 IEEE 62nd Electronic Components and Technology Conference* 1003–1008 (IEEE, 2012). doi:10.1109/ECTC.2012.6248958
82. Ricciardella, F. *et al.* Inkjet printed graphene-based chemi-resistors for gas detection in environmental conditions. in (2015). doi:10.1109/aisem.2015.7066858

83. Seekaew, Y. *et al.* Low-cost and flexible printed graphene–PEDOT:PSS gas sensor for ammonia detection. *Org. Electron.* **15**, 2971–2981 (2014).
84. Nikolaou, I. *et al.* Inkjet-Printed Graphene Oxide Thin Layers on Love Wave Devices for Humidity and Vapor Detection. *IEEE Sens. J.* **16**, 7620–7627 (2016).
85. Fang, Y. *et al.* A bio-enabled maximally mild layer-by-layer Kapton surface modification approach for the fabrication of all-inkjet-printed flexible electronic devices. *Sci. Rep.* **6**, 39909 (2016).
86. Fang, Y. *et al.* A novel, facile, layer-by-layer substrate surface modification for the fabrication of all-inkjet-printed flexible electronic devices on Kapton. *J. Mater. Chem. C* **4**, 7052–7060 (2016).
87. Kauffman, D. R. & Star, A. Carbon nanotube gas and vapor sensors. *Angewandte Chemie - International Edition* (2008). doi:10.1002/anie.200704488
88. Zhang, T., Mubeen, S., Myung, N. V. & Deshusses, M. A. Recent progress in carbon nanotube-based gas sensors. *Nanotechnology* (2008). doi:10.1088/0957-4484/19/33/332001
89. Ong, K. G., Zeng, K. & Grimes, C. A. A wireless, passive carbon nanotube-based gas sensor. *IEEE Sens. J.* (2002). doi:10.1109/JSEN.2002.1000247
90. Kong, J. *et al.* Nanotube molecular wires as chemical sensors. *Science* (80-.). (2000). doi:10.1126/science.287.5453.622
91. Li, J. *et al.* Carbon nanotube sensors for gas and organic vapor detection. *Nano Lett.* (2003). doi:10.1021/nl034220x
92. Fu, D. *et al.* Differentiation of gas molecules using flexible and all-carbon nanotube devices. *J. Phys. Chem. C* **112**, 650–653 (2008).
93. Sin, M. L. Y. *et al.* Ultralow-power alcohol vapor sensors using chemically functionalized multiwalled carbon nanotubes. *IEEE Trans. Nanotechnol.* **6**, 571–577 (2007).
94. Star, A., Joshi, V., Skarupo, S., Thomas, D. & Gabriel, J. C. P. Gas sensor array based on metal-decorated carbon nanotubes. *J. Phys. Chem. B* (2006). doi:10.1021/jp064371z
95. Kauffman, D. R. & Star, A. Chemically induced potential barriers at the carbon nanotube-metal nanoparticle interface. *Nano Lett.* **7**, 1863–1868 (2007).

96. Yamada, T. Modeling of carbon nanotube Schottky barrier modulation under oxidizing conditions. *Phys. Rev. B - Condens. Matter Mater. Phys.* (2004). doi:10.1103/PhysRevB.69.125408
97. Yamada, T. Equivalent circuit model for carbon nanotube Schottky barrier: Influence of neutral polarized gas molecules. *Appl. Phys. Lett.* **88**, 083106 (2006).
98. Cui, X., Freitag, M., Martel, R., Brus, L. & Avouris, P. Controlling energy-level alignments at carbon nanotube/Au contacts. *Nano Lett.* **3**, 783–787 (2003).
99. J. Kong, M. G. Chapline & H. Dai. Functionalized carbon nanotubes for molecular hydrogen sensors. *Adv. Mater.* **13**, 1384–1386 (2001).
100. Kong, J. & Dai, H. Full and modulated chemical gating of individual carbon nanotubes by organic amine compounds. *J. Phys. Chem. B* (2001). doi:10.1021/jp0101312
101. Krishna Kumar, M. & Ramaprabhu, S. Nanostructured Pt functionized multiwalled carbon nanotube based hydrogen sensor. *J. Phys. Chem. B* **110**, 11291–11298 (2006).
102. Wongchoosuk, C., Wisitsoraat, A., Phokharatkul, D., Tuantranont, A. & Kerdcharoen, T. Multi-Walled Carbon Nanotube-Doped Tungsten Oxide Thin Films for Hydrogen Gas Sensing. *Sensors* **10**, 7705–7715 (2010).
103. Yang, L., Zhang, R., Staiculescu, D., Wong, C. P. & Tentzeris, M. M. A novel conformal RFID-enabled module utilizing inkjet-printed antennas and carbon nanotubes for gas-detection applications. *IEEE Antennas Wirel. Propag. Lett.* (2009). doi:10.1109/LAWP.2009.2024104
104. Lee, H. *et al.* Carbon-nanotube loaded antenna-based ammonia gas sensor. *IEEE Trans. Microw. Theory Tech.* **59**, 2665–2673 (2011).
105. Vena, A., Sydänheimo, L., Tentzeris, M. M. & Ukkonen, L. A fully inkjet-printed wireless and chipless sensor for CO₂ and temperature detection. *IEEE Sens. J.* **15**, 89–99 (2015).
106. Gandhiraman, R. P. *et al.* Plasma jet printing for flexible substrates. *Appl. Phys. Lett.* **108**, (2016).
107. Ammu, S. *et al.* Flexible, all-organic chemiresistor for detecting chemically aggressive vapors. *J. Am. Chem. Soc.* **134**, 4553–4556 (2012).

108. Lorwongtragool, P. *et al.* Inkjet printing of chemiresistive sensors based on polymer and carbon nanotube networks. in *International Multi-Conference on Systems, Signals and Devices, SSD 2012 - Summary Proceedings* (2012). doi:10.1109/SSD.2012.6198043
109. Lorwongtragool, P., Sowade, E., Kerdcharoen, T. & Baumann, R. R. All inkjet-printed chemical gas sensors based on CNT/polymer nanocomposites: Comparison between double printed layers and blended single layer. in *2012 9th International Conference on Electrical Engineering/Electronics, Computer, Telecommunications and Information Technology, ECTI-CON 2012* (2012). doi:10.1109/ECTICon.2012.6254171
110. Mäklin, J. *et al.* Inkjet printed resistive and chemical-FET carbon nanotube gas sensors. in *Physica Status Solidi (B) Basic Research* **245**, 2335–2338 (2008).
111. Lorwongtragool, P., Sowade, E., Watthanawisuth, N., Baumann, R. R. & Kerdcharoen, T. A novel wearable electronic nose for healthcare based on flexible printed chemical sensor array. *Sensors (Switzerland)* **14**, 19700–19712 (2014).
112. Lin, Z. *et al.* Preparation of water-based carbon nanotube inks and application in the inkjet printing of carbon nanotube gas sensors. *J. Electron. Packag. Trans. ASME* (2013). doi:10.1115/1.4023758
113. Zhou, C. *et al.* Printed thin-film transistors and NO₂ gas sensors based on sorted semiconducting carbon nanotubes by isoindigo-based copolymer. *Carbon N. Y.* **108**, 372–380 (2016).
114. Kim, J., Yun, J. H., Song, J. W. & Han, C. S. The spontaneous metal-sitting structure on carbon nanotube arrays positioned by inkjet printing for wafer-scale production of high sensitive gas sensor units. *Sensors Actuators, B Chem.* **135**, 587–591 (2009).
115. Liu, R. *et al.* Fabrication of platinum-decorated single-walled carbon nanotube based hydrogen sensors by aerosol jet printing. *Nanotechnology* **23**, (2012).
116. Varghese, S. S., Lonkar, S., Singh, K. K., Swaminathan, S. & Abdala, A. Recent advances in graphene based gas sensors. *Sensors Actuators, B Chem.* (2015). doi:10.1016/j.snb.2015.04.062

117. Pantelides, S. T., Puzyrev, Y., Tsetseris, L. & Wang, B. Defects and doping and their role in functionalizing graphene. *MRS Bull.* (2012). doi:10.1557/mrs.2012.187
118. Araujo, P. T., Terrones, M. & Dresselhaus, M. S. Defects and impurities in graphene-like materials. *Materials Today* (2012). doi:10.1016/S1369-7021(12)70045-7
119. Gan, T. *et al.* Electrochemistry of folded graphene edges. *Adv. Funct. Mater.* **175**, 1–19 (2011).
120. Pak, A. J., Paek, E. & Hwang, G. S. Impact of Graphene Edges on Enhancing the Performance of Electrochemical Double Layer Capacitors. *J. Phys. Chem. C* **118**, 21770–21777 (2014).
121. Park, J., He, G., Feenstra, R. M. & Li, A. P. Atomic-scale mapping of thermoelectric power on graphene: Role of defects and boundaries. *Nano Lett.* (2013). doi:10.1021/nl401473j
122. Randviir, E. P., Brownson, D. A. C. C., Metters, J. P., Kadara, R. O. & Banks, C. E. The fabrication, characterisation and electrochemical investigation of screen-printed graphene electrodes. *Phys. Chem. Chem. Phys.* **16**, 4598–4611 (2014).
123. Ricciardella, F. *et al.* Effects of graphene defects on gas sensing properties towards NO₂ detection. *Nanoscale* (2017). doi:10.1039/c7nr01120b
124. Carbone, M., Gorton, L. & Antiochia, R. An overview of the latest graphene-based sensors for glucose detection: The effects of graphene defects. *Electroanalysis* (2015). doi:10.1002/elan.201400409
125. Lee, G., Yang, G., Cho, A., Han, J. W. & Kim, J. Defect-engineered graphene chemical sensors with ultrahigh sensitivity. *Phys. Chem. Chem. Phys.* (2016). doi:10.1039/c5cp04422g
126. Vicarelli, L., Heerema, S. J., Dekker, C. & Zandbergen, H. W. Controlling defects in graphene for optimizing the electrical properties of graphene nanodevices. *ACS Nano* (2015). doi:10.1021/acsnano.5b01762
127. Zhang, Y. H. *et al.* Improving gas sensing properties of graphene by introducing dopants and defects: A first-principles study. *Nanotechnology* (2009). doi:10.1088/0957-4484/20/18/185504

128. Hajati, Y. *et al.* Improved gas sensing activity in structurally defected bilayer graphene. *Nanotechnology* (2012). doi:10.1088/0957-4484/23/50/505501
129. Fuhrer, M. S. *et al.* Crossed nanotube junctions. *Science* (80-.). (2000). doi:10.1126/science.288.5465.494
130. Salehi-Khojin, A., Field, C. R., Yeom, J. & Masel, R. I. Sensitivity of nanotube chemical sensors at the onset of Poole-Frenkel conduction. *Appl. Phys. Lett.* **96**, 2–5 (2010).
131. Robinson, J. A., Snow, E. S., Bădescu, Ș. C., Reinecke, T. L. & Perkins, F. K. Role of defects in single-walled carbon nanotube chemical sensors. *Nano Lett.* **6**, 1747–1751 (2006).
132. Jabari, E. & Toyserkani, E. Micro-scale aerosol-jet printing of graphene interconnects. *Carbon N. Y.* **91**, 321–329 (2015).
133. Goh, G. L., Agarwala, S. & Yeong, W. Y. Aerosol-Jet-Printed Preferentially Aligned Carbon Nanotube Twin-Lines for Printed Electronics. *ACS Appl. Mater. Interfaces* **11**, 43719–43730 (2019).
134. Pandhi, T. *et al.* Electrical Transport and Power Dissipation in Aerosol-Jet-Printed Graphene Interconnects. *Sci. Rep.* **8**, (2018).
135. Cho, Y. C., Elsayed, M. Y. & El-Gamal, M. N. A Metal-Oxide Gas Sensor Based on an Aerosol Jet Printing Technology Featuring a One Second Response Time. in *2019 20th International Conference on Solid-State Sensors, Actuators and Microsystems and Eurosensors XXXIII, TRANSDUCERS 2019 and EUROSENSORS XXXIII* (2019). doi:10.1109/TRANSDUCERS.2019.8808446
136. Dey, A. *et al.* Plasma Jet Printing and in Situ Reduction of Highly Acidic Graphene Oxide. *ACS Nano* (2018). doi:10.1021/acsnano.8b00903
137. Chansin, G. & Pugh, D. Environmental Gas Sensors 2017-2027. *IDTechEx* 1–10 (2016). Available at: <https://www.idtechex.com/en/research-report/environmental-gas-sensors-2017-2027/500>. (Accessed: 30th September 2020)
138. Gao, W. *et al.* Fully integrated wearable sensor arrays for multiplexed in situ perspiration analysis. *Nature* (2016). doi:10.1038/nature16521

139. Rose, D. P. *et al.* Adhesive RFID sensor patch for monitoring of sweat electrolytes. *IEEE Trans. Biomed. Eng.* **62**, 1457–1465 (2015).
140. Hoe, Y. Y. G. *et al.* A microfluidic sensor for human hydration level monitoring. in *2011 Defense Science Research Conference and Expo, DSR 2011* (2011). doi:10.1109/DSR.2011.6026879
141. Van Den Brand, J. *et al.* Flexible and stretchable electronics for wearable health devices. *Solid. State. Electron.* **113**, 116–120 (2015).
142. Tao, X. *Wearable electronics and photonics. Wearable Electronics and Photonics* (2005). doi:10.1533/9781845690441.198
143. Fan, F. R., Tang, W. & Wang, Z. L. Flexible nanogenerators for energy harvesting and self-powered electronics. *Advanced Materials* **28**, 4283–4305 (2016).
144. Ford, S. & Despeisse, M. Additive manufacturing and sustainability: an exploratory study of the advantages and challenges. *J. Clean. Prod.* (2016). doi:10.1016/j.jclepro.2016.04.150

CHAPTER THREE: ELECTRICAL TRANSPORT AND POWER DISSIPATION IN
AEROSOL-JET-PRINTED GRAPHENE INTERCONNECTS

Twinkle Pandhi¹, Eric Kreit², Roberto Aga², Kiyoo Fujimoto¹, Mohammad Taghi
Sharbati³, Samane Khademi³, A. Nicole Chang¹, Feng Xiong³, Jessica Koehne⁴, Emily
M. Heckman⁵, David Estrada¹

¹Micron School of Materials Science and Engineering, Boise State University, Boise, ID
83725, United States

²KBRwyle, 2601 Mission Point Blvd, Suite 300, Beavercreek, OH 45431, United States

³Department of Electrical and Computer Engineering, University of Pittsburgh,
Pittsburgh, PA 15261, United States

⁴NASA Ames Research Center, Moffett Field, CA 94035, United States

⁵Air Force Research Laboratory, Sensors Directorate, 2241 Avionics Circle, Wright-
Patterson AFB, OH 45433, United States

* Corresponding Author: daveestrada@boisestate.edu

Reproduced with permission from Nature Research in Scientific Reports

Scientific Reports volume 8, Article number: 10842 (2018)

<https://doi.org/10.1038/s41598-018-29195-y>

No significant changes were made to this publication.

3.1 Abstract

This chapter reports the first known investigation of power dissipation and electrical breakdown in aerosol-jet-printed (AJP) graphene interconnects. The electrical performance of aerosol-jet printed (AJP) graphene was characterized using the Transmission Line Method (TLM). The electrical resistance decreased with increasing printing pass number (n); the lowest sheet resistance measured was $1.5 \text{ k}\Omega/\square$ for $n=50$. The role of thermal resistance (R_{TH}) in power dissipation was studied using a combination of electrical breakdown thermometry and infrared (IR) imaging. A simple lumped thermal model ($\Delta T = P \times R_{\text{TH}}$), and COMSOL Multiphysics was used to extract the total R_{TH} , including interfaces. The R_{TH} of AJP graphene on KaptonTM is ~ 27 times greater than that of AJP graphene on Al_2O_3 with a corresponding breakdown current density 10x less KaptonTM versus Al_2O_3 .

Keywords: Graphene, Additive Manufacturing, Aerosol-Jet Printing, Flexible Electronics, Power Dissipation

3.2 Introduction

Wearable technology is an emerging multi-billion-dollar industry that is made possible, in part, by advances in flexible and wearable electronic devices.¹⁻⁴ Conventional fabrication processes such as vacuum deposition, photolithography, and epitaxial growth of electronic materials tend to be complex, expensive, and incompatible with rapid prototyping.⁵⁻⁷ Additive manufacturing techniques, such as inkjet printing, aerosol jet printing (AJP), and extrusion printing, are being explored as alternative fabrication methods for such sensor systems.⁸⁻¹² Direct write techniques offer a low-cost fabrication

alternative due to the reduced material consumption and allow for rapid customization and prototyping.^{9,12-14}

Despite the rising popularity of printing techniques, there is a growing need for ink formulations and materials to meet the demand of the electronics industry. Printable, conductive metals like Ag and Cu have been widely studied, but their applications are restricted by their high cost and the rapid oxidation of Cu.⁹ While conductive polymer inks provide low cost printing, their performance is limited by their low conductivities, and poor thermal and chemical stabilities. Carbon nanotubes (CNTs), have shown promise as an AJP compatible ink with significant mechanical flexibility and high mobility making them attractive for AJP applications.^{15,16} Nevertheless, due to poor dispersion of CNTs in AJP compatible inks and the high cost of monodispersed solutions, the applications of CNTs remain limited for AJP printable devices.^{17,18} One of the more promising nanomaterials for such applications is graphene, a two-dimensional (2D) hexagonal carbon structure with sp^2 hybridized carbon atoms.¹⁹ Due to its high specific surface area, high carrier mobility, and unique band structure, graphene has shown many promising properties and demonstrated breakthroughs in electronic related applications.²⁰⁻²³ Graphene is also a promising sensor electrode material due to its flexibility and high electrochemical activity at defect sites.^{3,24-26}

Inkjet printing of graphene has been well established,^{9,27,28} and several groups have demonstrated inkjet printed graphene chemical²⁹ and biological³⁰ sensors. Graphene inks are typically produced through liquid phase exfoliation of graphite or chemical and/or thermal reduction of graphene oxide.^{31,32} These processes typically result in submicron graphene crystal domains, and give rise to numerous point defects within the

lattice, and closed-contour defects around the flake's edge.³³ Under applied electrical bias, these defects result in highly localized electric fields which can be modified by absorbed molecules/target analytes. Combined with the high electrical conductivity and specific surface area of graphene, these defects enable highly sensitive graphene based sensors able to detect target molecules with parts per billion sensitivity in controlled environments.³³ Furthermore, as inkjet is typically a drop-on-demand process, the microstructure of inkjet printed graphene typically results in a well layered structure with varying amounts of porosity, depending on annealing conditions, ink properties, and the number of print passes. In this regard, graphene's compatibility with AJP is less understood.^{8,9,34}

While additive manufacturing is rapidly advancing the low-power sensor applications of graphene, the high-power and high-temperature applications of additively manufactured graphene-based devices have received less attention. Such applications include temperature sensors, resistive heaters, thermal heat spreaders, high-current carrying interconnects, ordnance fuze technology.³⁵⁻³⁹ Substrate properties, microstructure, and thermal interfaces are likely to play a critical role in limiting the reliability and power dissipation in such applications. Previous studies have reported power dissipation processes for mechanically exfoliated, chemical vapor deposition (CVD), and epitaxial grown graphene-based devices. However, power dissipation in printed graphene-based devices has yet to be explored.⁴⁰⁻⁴⁵ This work, therefore, investigates the roles of microstructure and the substrate properties on power dissipation in AJP graphene interconnects. The information gained from this study is expected to provide new fundamental insights that will impact low-power and high-power

applications of AJP graphene devices, as device models for both will require understanding the physical properties of such materials systems and printed devices.

3.3 Results and Discussion

3.3.1 Graphene Ink Characterization

Graphene is obtained via solvent assisted exfoliation of bulk graphite, a process which has a relatively high yield of graphene flakes and is compatible with the ink synthesis processes. In order to develop highly-concentrated graphene ink, we use a combination of the processes reported in Jabari *et al.* and Secor *et al.*.^{8,28} Bulk graphite powder was sonicated in ethanol and the stabilizing polymer ethyl cellulose to obtain suspended graphene flakes. The graphene flakes were then dispersed in a mixture of 92.5% cyclohexanone and 7.5% terpineol, which has been shown to be compatible with AJP (**Figure 3.1a**).⁸ This resulted in an ink concentration of 3.5 mg/ml, which was quantified by UV-VIS absorption spectroscopy and Beer-Lamberts law (**Figure 3.1b**). The ink viscosity of 3.6 cp was measured using a Cone Plate Wells Brookfield Viscometer. To image the individual graphene flakes, we dispersed the graphene in ethanol solution and drop casted onto TEM grids and a SiO₂ coated Si wafer. These samples were then thermally annealed on a hotplate (250 °C for 10 min) and characterized with both TEM and Raman Spectroscopy. Raman spectroscopy revealed the characteristic D, G and 2D peaks for graphene at 1350 cm⁻¹, 1580 cm⁻¹ and 2700 cm⁻¹, respectively. The ratio of the D/G peak intensities (I_D/I_G) determines the quality (defect/disorder) of the graphene flakes. The I_D/I_G peak ratio of 0.24 is lower than previously reported values (0.33-0.7), suggesting the exfoliated flakes are of higher quality with fewer defects.⁴⁶ TEM images in **Figure 3.1c** the graphene flakes vary in

lateral size from $\sim 50 - 200$ nm. To correlate the TEM and Raman data, the I_D/I_G peak ratio and 532 nm excitation wavelength was used in Cancado's general equation⁴⁷ to extract the crystal size ($L_a \approx 80$ nm) of the graphene flakes. AFM characterization of the flakes shows the thickness (t_g) ranges from monolayer to flakes with an average thickness of $t_g = 16$ nm \pm 15 nm (**Figure 3.2**).

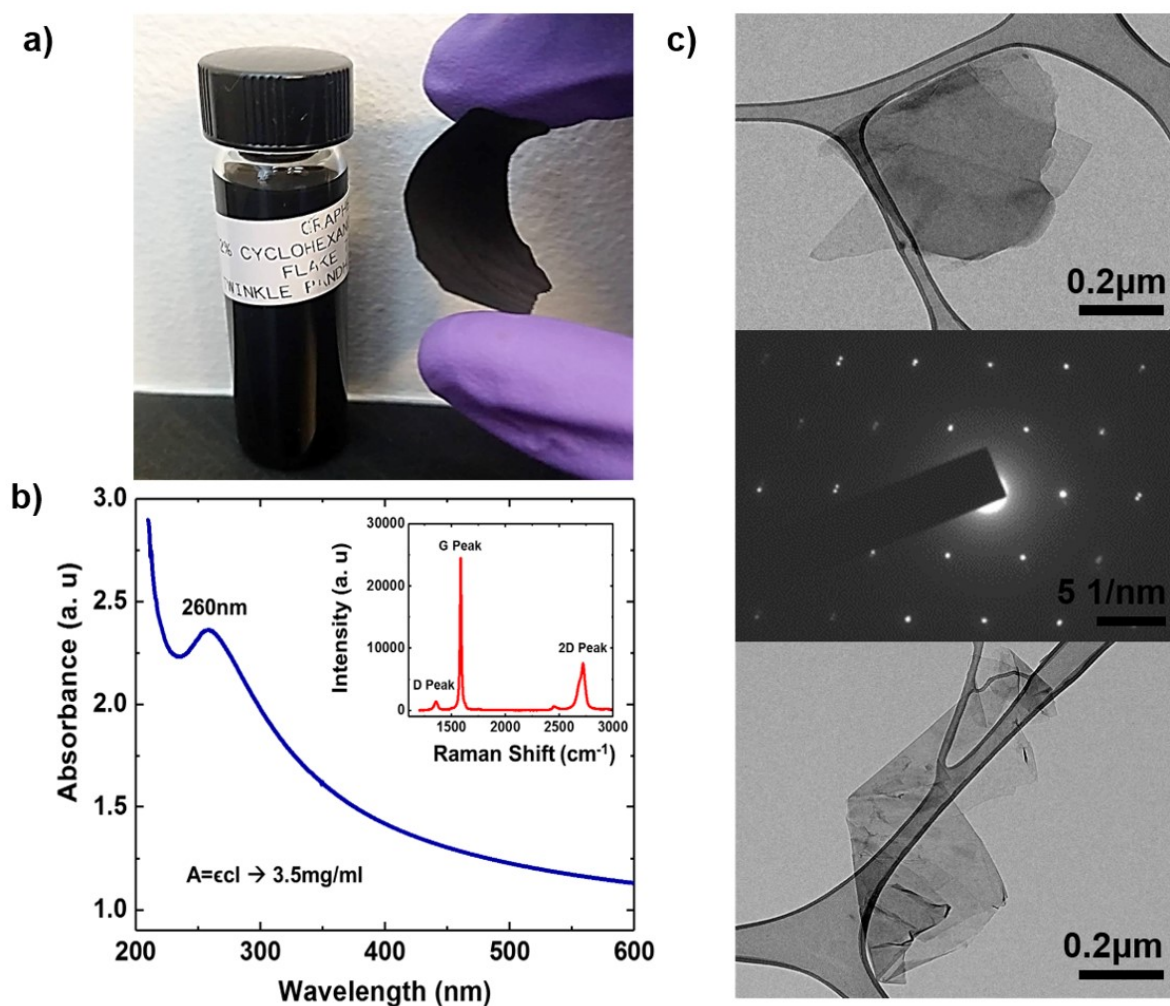


Figure 3.1 Graphene ink characterization (a) optical image of solvent exfoliated graphene/ethyl cellulose (EC) paper and AJP compatible graphene ink solution (b) UV-Visible absorption spectra is employed for quantifying the graphene flake concentration using the Lambert-Beer Law. Typical Raman spectra is seen (inset) for graphene/EC flakes on SiO₂ (c) TEM images and diffraction pattern of graphene flakes: to extract and compare lateral crystal dimensions we observed and calculated using Raman spectra and Cancado's equation.

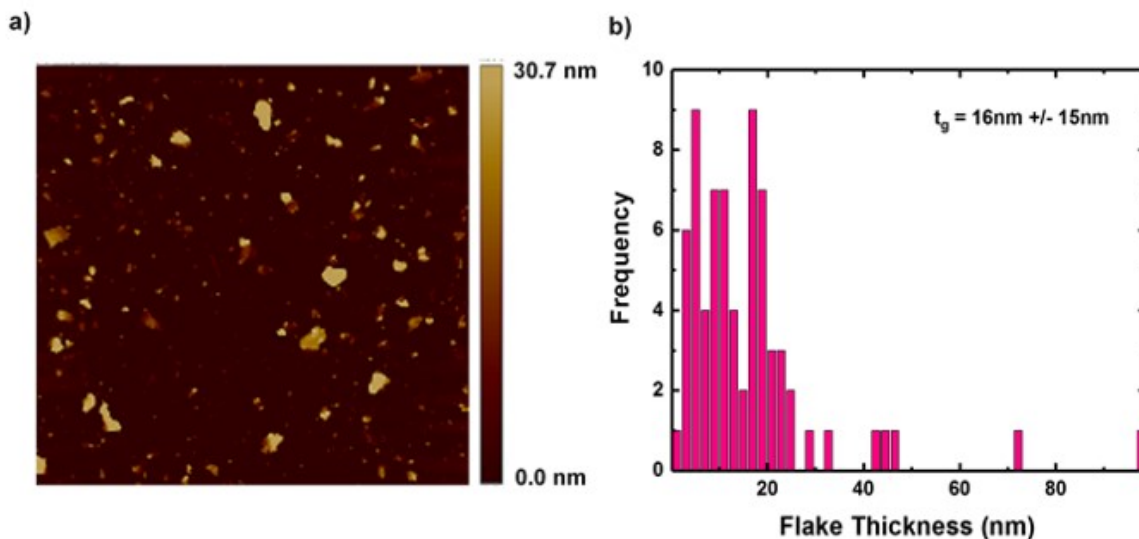


Figure 3.2 To characterize the graphene flakes, diluted graphene ink was drop-casted and annealed (at 100°C for 10 min) on Si/SiO₂ wafer. (a) AFM scan of the dispersed graphene flakes was used to obtain particle statistics. Histogram of (b) flake thickness was extrapolated by using ImageJ.

3.3.2 Aerosol-Jet Printed Graphene Interconnects

AJP offers several advantages over IJP, such as higher resolution ($\sim 10\ \mu\text{m}$), a broader range of viscosities for inks, and the ability to print on conformable substrates.^{1,2} However, due to a limited library of AJP compatible material inks, applications of AJP in flexible and wearable technologies have typically been limited to metallic lines and interconnects for passive devices.^{1,3} Moreover, inkjet printing of graphene is well established, whereas graphene's compatibility with AJP is less understood.⁴⁻⁶ In light of this, we worked to develop graphene-based inks that are compatible with AJP. Here we investigate the fundamental structure of AJP deposited graphene interconnects on Si/SiO₂, KaptonTM, and Al₂O₃ substrates, with help from our Air Force collaborators. The graphene interconnects, and silver contact pads (Clariant Prelect TPS 35) were printed with an Optomec AJ-300 aerosol jet printer using the UA-max ultrasonic atomizer.

The graphene print passes were varied from $n=5$ to $n=50$ and were deposited on SiO_2/Si , KaptonTM, and Al_2O_3 substrates. The graphene was printed in TLM test structures with $200\ \mu\text{m} \times 200\ \mu\text{m}$ printed silver contacts (**Figure 3.3a**).⁷ A recirculating bath temperature of $15\ ^\circ\text{C}$ was used to stabilize the ink. After printing, the graphene lines were annealed for 60 min at $250\ ^\circ\text{C}$. The silver contacts were then printed on top of the graphene in a TLM structure. The SEM image of the AJP graphene TLM structure is shown in **Figure 3.3b**. **Figure 3.3c** shows a magnified SEM image of the graphene line to observe the uniformity of AJP.

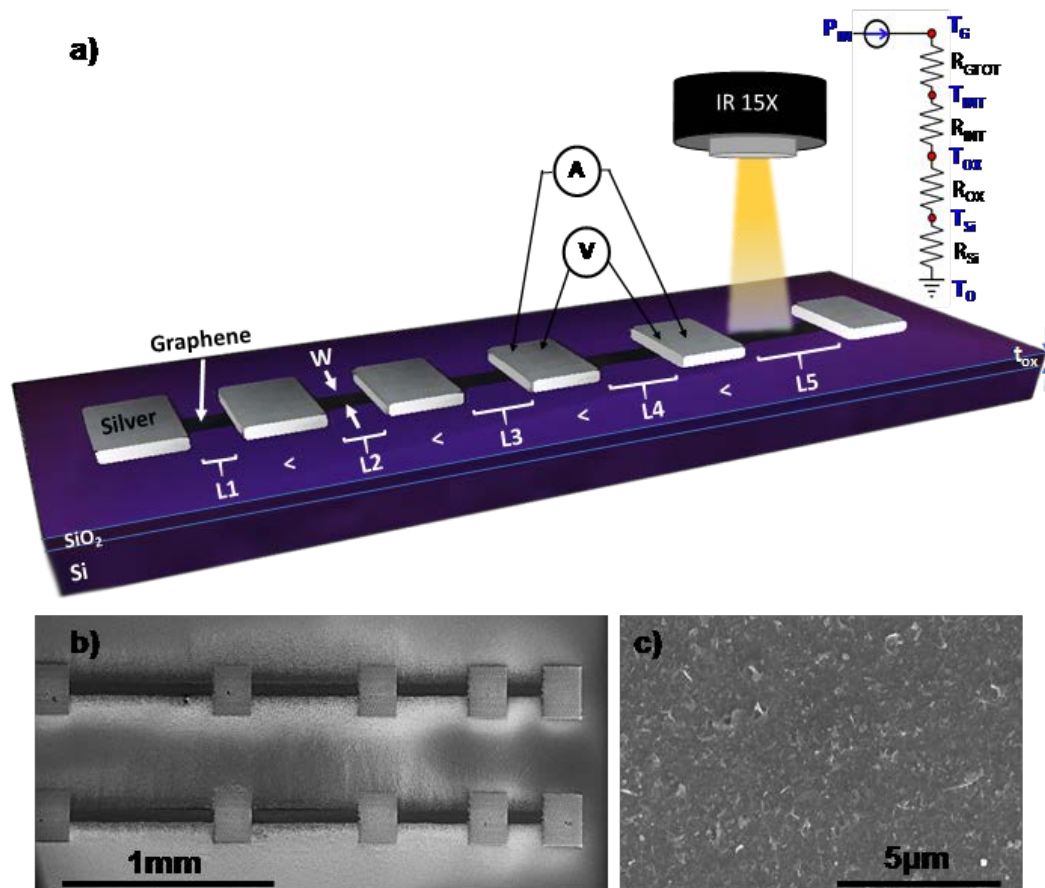


Figure 3.3 Investigating power dissipation of printed graphene interconnects with a combination of electrical breakdown and IR imaging. (a) Schematic of TLM experimental test structures of AJP graphene interconnects (increasing number of passes $n=5$ to $n=50$) with silver contact pads on Si/SiO₂ (b,c) SEM images of the AJP printed/annealed graphene interconnects and a magnified SEM image to show the uniformity of the printed graphene.

Using stylus profilometry, the change in height profile of the graphene interconnect was monitored as a function of increasing number of print passes. The height data seen in **Figure 3.4a** shows a uniform deposition rate with an increase in height directly correlated to the number of passes. A similar height profile is observed for printed graphene interconnects on KaptonTM (**Figure 3.5a-b**).

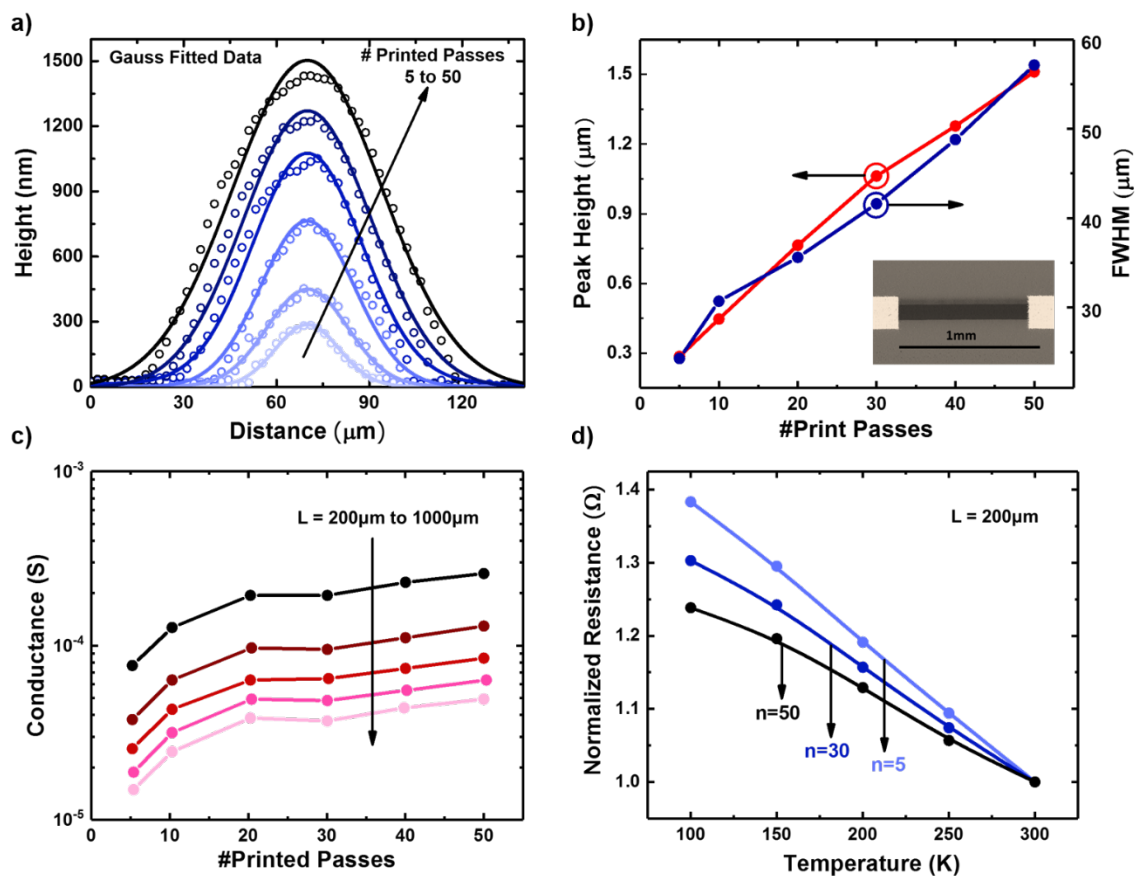


Figure 3.4 a) Height profile of the graphene interconnect on Si/SiO₂ is seen as a function of increasing number of print passes $n=5$ to $n=50$, shows a uniform deposition rate. (b) Full-width-half-max (FWHM) and peak height data extracted from the height profile provides additional support for the height correlation. (c) The electrical conductance of the graphene interconnects on Si/SiO₂, for $n=50$ pass line, with increasing length ($L=200 \mu\text{m}$ to $L=1000 \mu\text{m}$). (d) Temperature-dependent measurements: normalized resistance inversely proportional to temperature.

The linear relation of the full-width-half-max (FWHM) and peak height data (Figure 3.4b) extracted from the height profile provides additional support for this correlation. We note that while the FWHM of the graphene printed on Al₂O₃ substrates remains constant as the peak height increases with increasing pass number (see Figure 3.5d), suggesting the substrate surface energy interactions with the graphene ink can influence the final morphology of the printed graphene interconnects.⁸

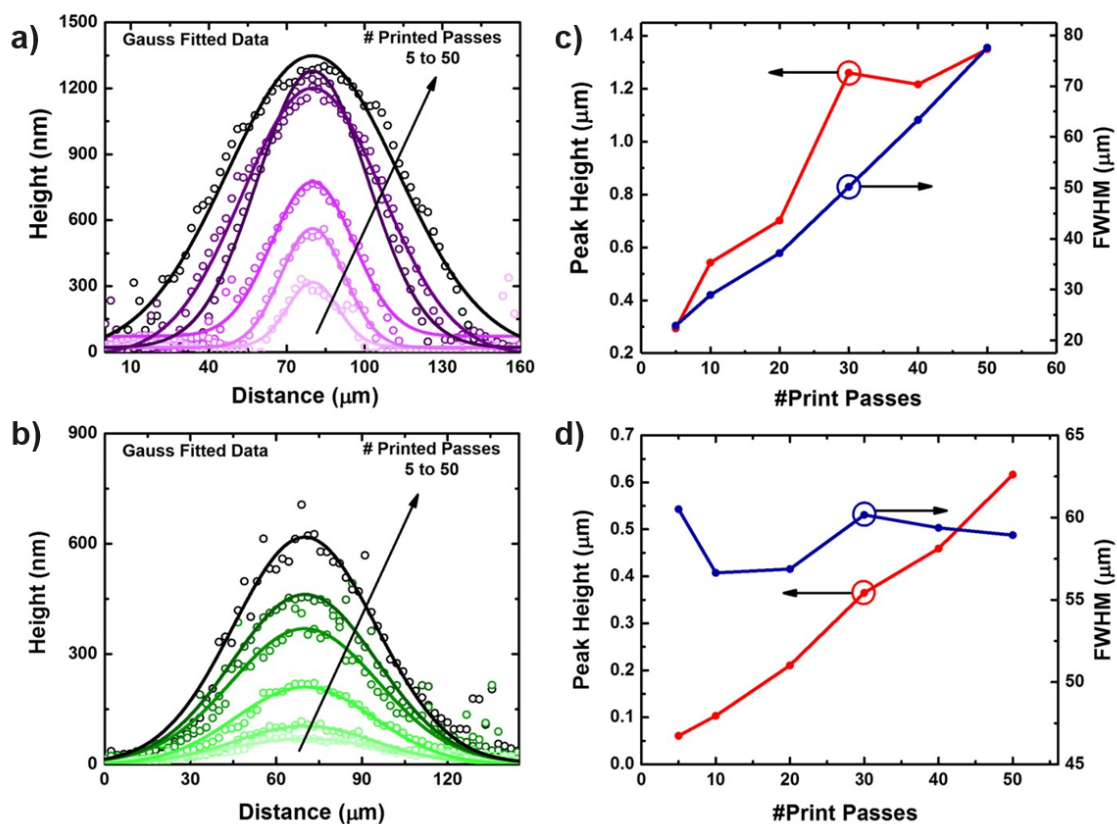


Figure 3.5 Stylus profilometry was used to extract height profile of the graphene interconnect was monitored as a function of increasing number of print passes on KaptonTM (a, c) and on Al₂O₃ (b, d)

3.3.3 Electrical Scaling in AJP Graphene Interconnects

To measure the electrical properties of the printed interconnects, a 2-point probe (Keithley 4200 SCS) and TLM technique was used. As seen in **Figure 3.4c**, for the 50-pass line on SiO₂/Si, conductance decreases with increasing length (L1 to L5) as expected. Based on the TLM measurements the lowest sheet resistance was calculated as 1.5 k Ω /□ for n=50 at room temperature.⁴⁸ Similar conductance profiles are seen for KaptonTM and Al₂O₃ (see **Figure 3.6a-b**). To understand the transport mechanism of the printed graphene, temperature-dependent measurements were performed. In **Figure 3.4d** the normalized resistance is inversely proportional to the temperature. This observation

agrees with the variable range hopping (VRH) model formerly established for graphene-based sensor devices; highlighting the potential to tune the graphene electrical transport properties from VRH to phonon limited conduction based on ink properties and printing parameters.⁹ The electrical conductance increases by a factor of 30 based on the device dimensions and the number of print passes, which is in good agreement with literature.⁶

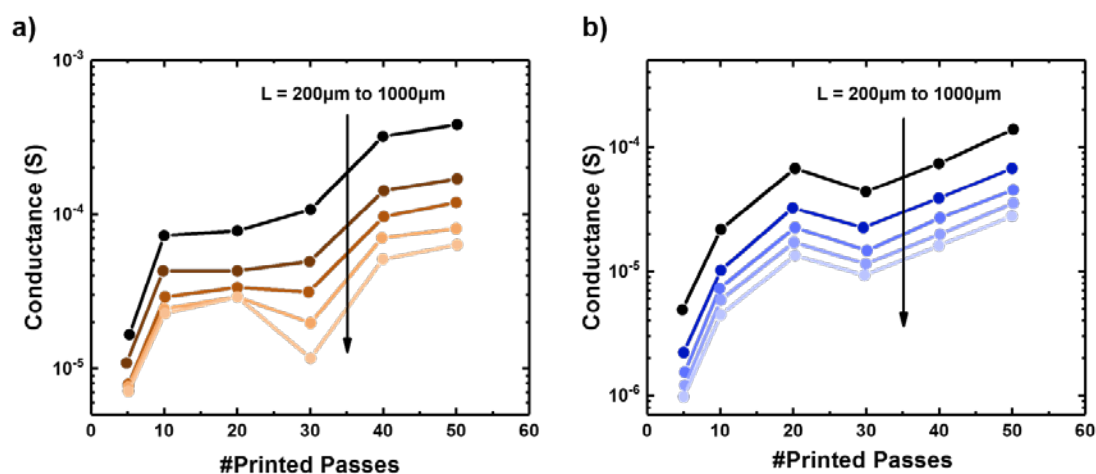


Figure 3.6 Conductance of the graphene interconnect was monitored as a function of increasing number of print passes on Kapton™ (a) and on Al₂O₃ (b)

3.3.4 Power Dissipation of AJP Graphene Interconnects

The overall power dissipation of a graphene device is dependent on the effective thermal conductivity and total thermal resistance of the system. Substrate material, interface thermal resistances, graphene quality, and device structure are a few of the factors that directly impact the total device thermal resistance.^{40,41,50} To study this effect, a simple lumped model, was developed that uses a combination of infrared (IR) thermal imaging and electrical breakdown thermometry supported by finite element modeling (FEM) using COMSOL multiphysics software.⁵¹⁻⁵³

Simple lumped model: Similar to Ohm's law ($\Delta V = IR$), the temperature rise (ΔT) in the graphene interconnects can be calculated as $\Delta T = P \times R_{TH}$, where $P = I^2 \times R_{EL}$

is the dissipated power, and R_{TH} is the total thermal resistance of the device. Here ΔT is comparable to ΔV , P is comparable to I , and $R_{TH} = L/(\kappa_{EFF} \times A)$ is the total thermal resistance and depends on the device dimensions and an effective thermal conductivity for the system (κ_{EFF}). We note that R_{EL} is the inverse of the device conductance, highlighting the potential to tune P based on print passes and device dimensions. To understand the limiting factors in power dissipation, R_{TH} is treated as a sum of the thermal resistances associated with the individual components of the system. For the AJP graphene devices, R_{TH} is the sum of the graphene interconnect thermal resistance (R_{GTOT}), the thermal interface resistance between graphene and the substrate ($R_{INT}=1/(g \times A)$), and the thermal resistance of the substrate (R_{Sub}). For the SiO_2/Si substrate, R_{Sub} is the sum of the oxide thermal resistance ($R_{OX}=t_{OX}/(\kappa_{OX} \times A)$) and the silicon thermal resistance ($R_{Si}=1/(2 \times \kappa_{Si} \times A^{1/2})$). Here, $t_{OX} = 90$ nm, $\kappa_{OX} = 1.4$ $Wm^{-1}K^{-1}$, $\kappa_{Si}=100$ $Wm^{-1}K^{-1}$, g is the graphene $-SiO_2$ boundary thermal boundary conductance taken as 10^8 $Wm^{-2}K^{-1}$, and A is the area of the printed graphene interconnect ($A=L \times W$).^{54,55} For samples printed on KaptonTM and Al_2O_3 , the R_{OX} term is negligible, and the substrate thermal resistances are simply ($R_{Sub}=1/(2 \times \kappa_{Sub} \times A^{1/2})$), where κ_{Sub} is the substrate thermal conductivity is taken as 0.12 $Wm^{-1}K^{-1}$ and 32 $Wm^{-1}K^{-1}$ for KaptonTM and Al_2O_3 (sapphire), respectively.^{56,57} Based on this model, a combination of IR microscopy and electrical breakdown thermometry can be used to quantify the heat spreading and estimate the “missing” R_{GTOT} associated with the printed graphene interconnects.

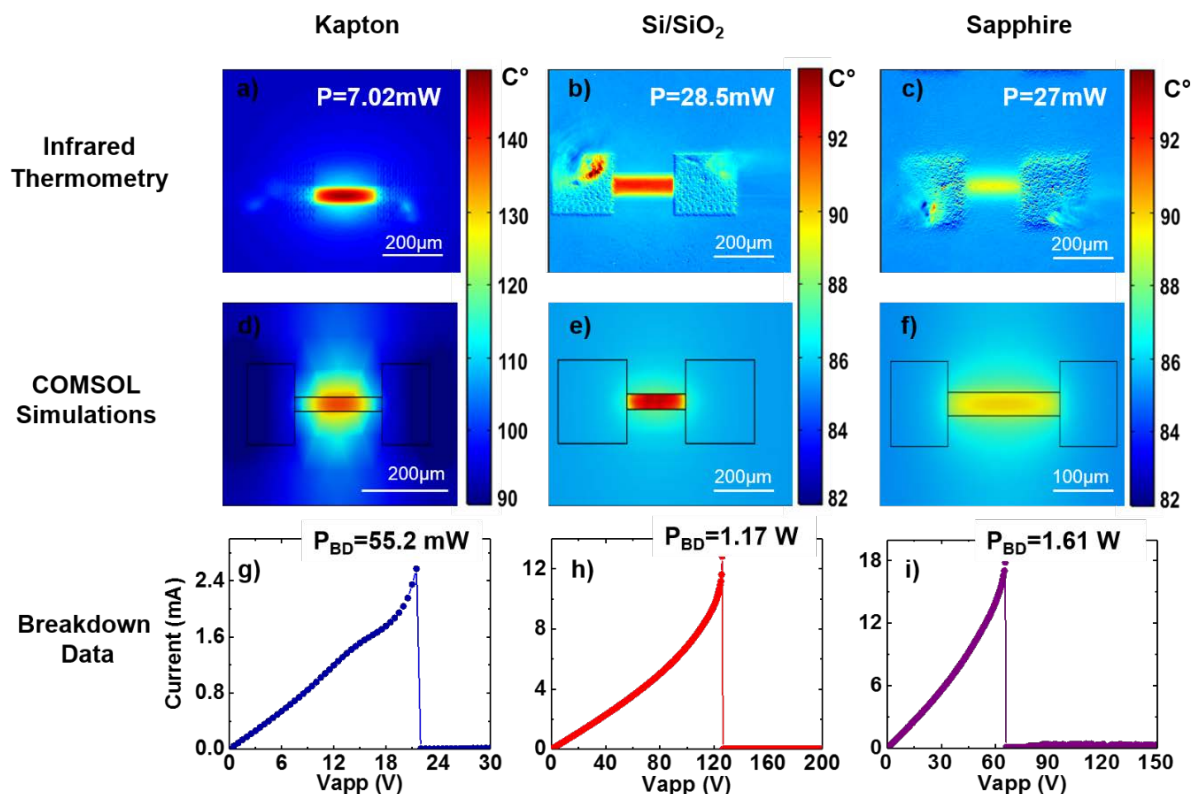


Figure 3.7 Power Dissipation investigation of AJP graphene interconnects: Infrared (IR) thermal images of printed graphene interconnects with $n = 20$ print passes. (a) KaptonTM, (b) SiO₂, and (c) Al₂O₃ (d - f) COMSOL simulation IR images to support the correlating experimental IR images seen above. The temperature scale bar is identical for both experimental and simulated results (g - i) Current vs. Voltage characteristics of AJP printed graphene interconnects on various substrates to extract power breakdown values.

IR Microscopy: The thermal profiles of the graphene devices were characterized under varying bias conditions. The background temperature T_0 was set to 85 °C for a better signal to noise ratio over background IR emission. The thermal profile for graphene on KaptonTM (**Figure 3.7a**) measured a temperature rise of 65 °C associated with an applied power of 7mW. Comparatively, the temperature rise for the SiO₂/Si is 10 °C for an applied power of 28 mW (**Figure 3.7b**), and the temperature increase for Al₂O₃ is 5 °C for an applied power of 27 mW (**Figure 3.7c**). These data illustrate the role of the substrate thermal properties on efficient heat spreading. For example, using the simple

lumped model ($\Delta T = P \times R_{TH}$), the high-temperature rise at low power for KaptonTM results in a total thermal resistance of 9285 K/W compared to 350 K/W for SiO₂/Si and 185 K/W for Al₂O₃.

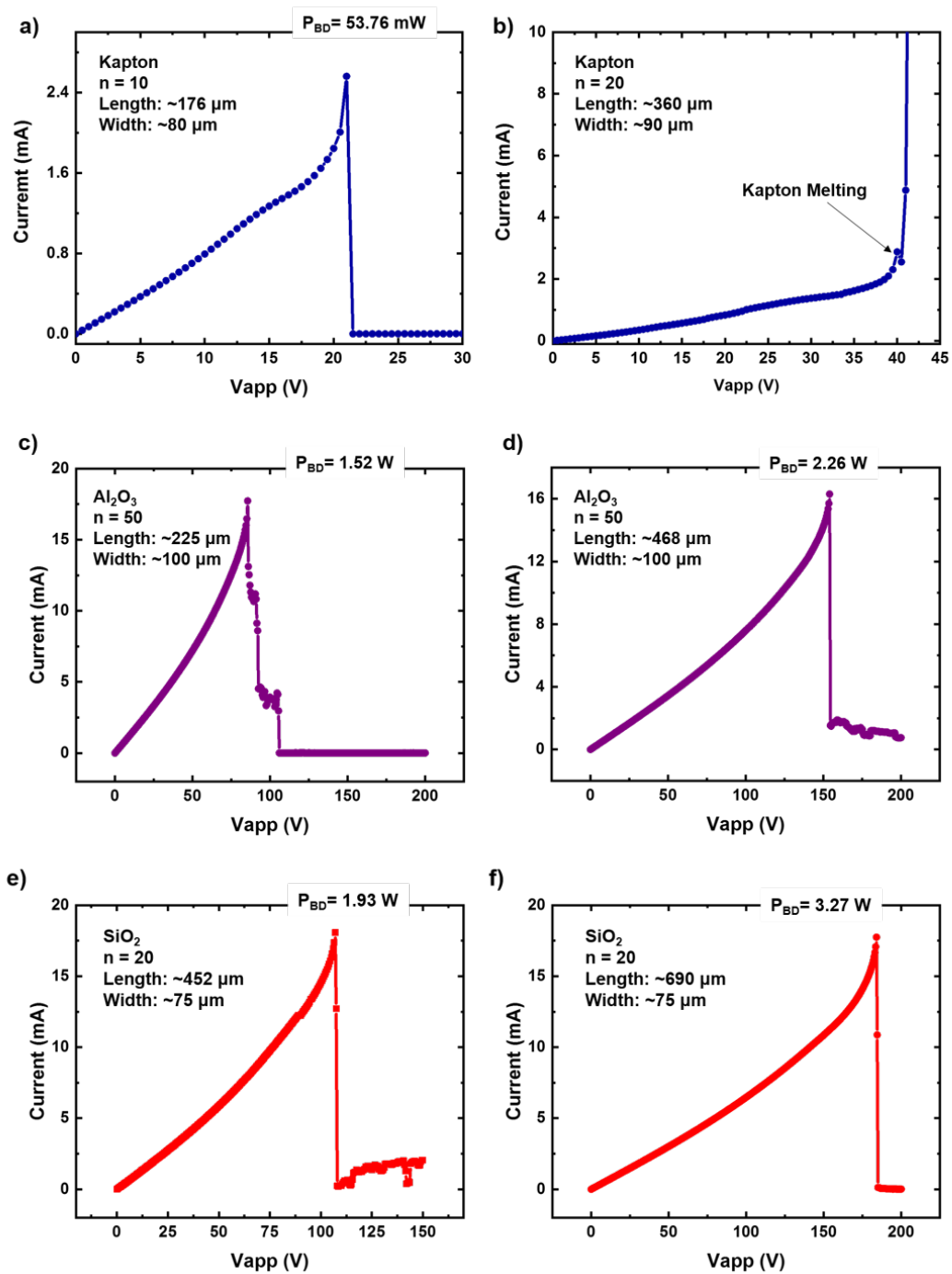


Figure 3.8 Current vs. Voltage characteristics of AJP graphene interconnects on various substrates where a-b) breakdown of KaptonTM, c-d) Al₂O₃, and e-f) breakdown of Si/SiO₂.

For **Figure 3.8b**, we see that current rises until the KaptonTM substrate breaks down and starts to melt at approximately 40V. The melted KaptonTM results in a high conductance, and the current rises rapidly towards the instrument's compliance limit.

Electrical Breakdown Thermometry and COMSOL: To quantify the R_{GTOT} contributions to R_{TH} , a combination of electrical breakdown thermometry and COMSOL Multiphysics was used. **Figures 3.7g-i** show the corresponding I-V characteristics up to device failure for graphene interconnects printed on three different substrates (additional breakdown data seen in **Figure 3.8**). Failure of a Joule-heated device occurs when the temperature rise of the device from the background temperature (T_0) of 85 °C exceeds the breakdown temperature (T_{BD}), which is either the decomposition temperature of KaptonTM or the oxidation temperature of the graphene on SiO₂/Si or Al₂O₃ (measured via TGA data, see **Figure 3.9**).

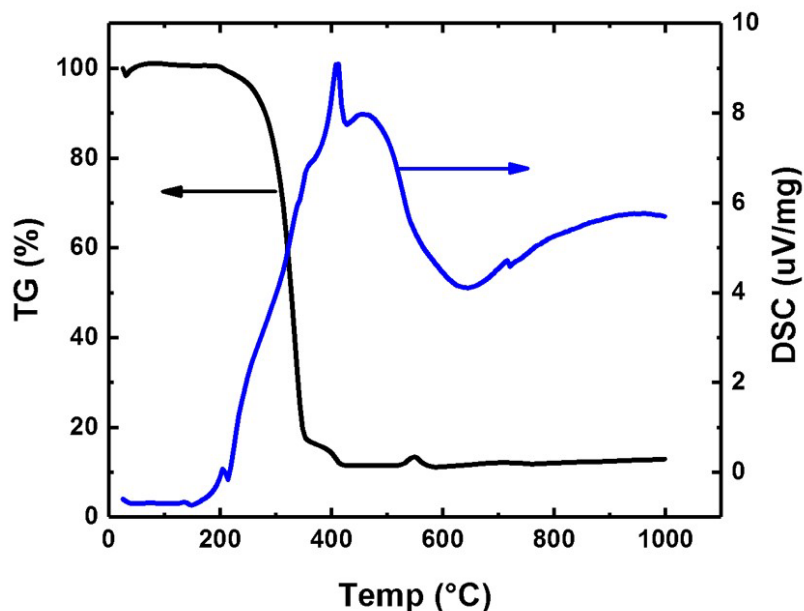


Figure 3.9 TGA (Netzsch instrument, at a heating rate of 5°C/min in the air) of the dried graphene flakes (black), showing mass as a function of temperature and (blue) the differential mass loss. The decomposition peak of surfactant, ethylcellulose, is around 250°C, and oxidation/decomposition of the graphene around 550°C

The power values P of the graphene interconnects were measured up to device failure, which likely occurs when reaching the breakdown temperatures. Using the simple lumped model and 550 °C as the oxidation temperature of carbon (verified by TGA data seen in **Figure 3.9**) for the graphene inks, the individual components of the thermal resistances for the graphene interconnects on SiO₂/Si substrates can be quantified. Using this approach, R_{GTOT} is calculated as $R_{GTOT} = R_{TH} - R_{INT} - R_{OX} - R_{Si}$. The total thermal resistance at the breakdown temperature is 397 K/W. This is only slightly higher than that calculated from low power and IR microscopy and is likely due to temperature dependences of the individual thermal resistances. At the breakdown temperature, $R_{INT} = 1.1 \times 10^{-8} \text{ m}^2\text{K/W}$, $R_{OX} = 4.6\text{K/W}$, and $R_{Si} = 42.3\text{K/W}$. Therefore, the total thermal resistance is dominated by $R_{GTOT} = 349 \text{ K/W}$. A similar analysis for graphene interconnects on Al₂O₃ finds $R_{INT} = 1.0 \times 10^{-8} \text{ m}^2 \text{ K/W}$, $R_{Sub} = 115.3 \text{ K/W}$, and a slightly

lower value of $R_{GTOT} = 173 \text{ K/W}$. This lower R_{GTOT} value can be attributed to the physically thinner interconnect, which is approximately $\frac{1}{2}$ as thick as $N=20$ graphene interconnects printed on SiO_2/Si substrates. Applying this model to the graphene interconnects on KaptonTM, with a melting temperature of $520 \text{ }^\circ\text{C}$ ⁵⁶ and a measured power of 55.2 mW , the total thermal resistance of the interconnect is found to be 7880 K/W . However, the calculated thermal resistance of the substrate is $3.67 \times 10^4 \text{ K/W}$, indicating significant heat transfer between the KaptonTM substrate and the supporting metal substrate during breakdown measurements.

COMSOL multiphysics was used to further analyze the thermal spreading in these systems. **Figures 3.7d-f** show the corresponding COMSOL thermal images for the simulated device structure compared to the thermal images of the actual devices seen in **Figures 3.7a-c**. The thermal profiles show that the experimental results for the imaged power dissipation are in good agreement with the computational results for all three substrates. Furthermore, the COMSOL simulation results can be used to analyze the temperature of each layer of the printed graphene device on SiO_2/Si (the graphene interconnect layer, the interface layer, the oxide layer, and the silicon layer) in order to observe where the maximum power dissipation is taking place. The total thermal resistance of the interconnect on SiO_2/Si was calculated to be 372 K/W , with the highest temperature value of $520 \text{ }^\circ\text{C}$ being reached within the graphene interconnect. From these calculations, it can be concluded that the power dissipation is dominated by the graphene interconnect. The high thermal resistance of the graphene interconnects likely due to several factors: the porosity of the printed interconnects, the high thermal resistance

between graphene layers, and the general disorder of the constituent graphene nanoflakes that make up the interconnect.^{41,58}

Cross-sectional TEM imaging was used to quantify the porosity of the printed graphene interconnects on SiO₂/Si and better understand the structure of AJP deposited graphene. Analysis of the TEM images seen in **Figure 3.10a-d** indicates 15 % porosity in the graphene interconnects. Furthermore, it can be seen that porosity at the graphene-substrate interface reduces the total area for heat flow across the interface, increasing the thermal interface resistance.

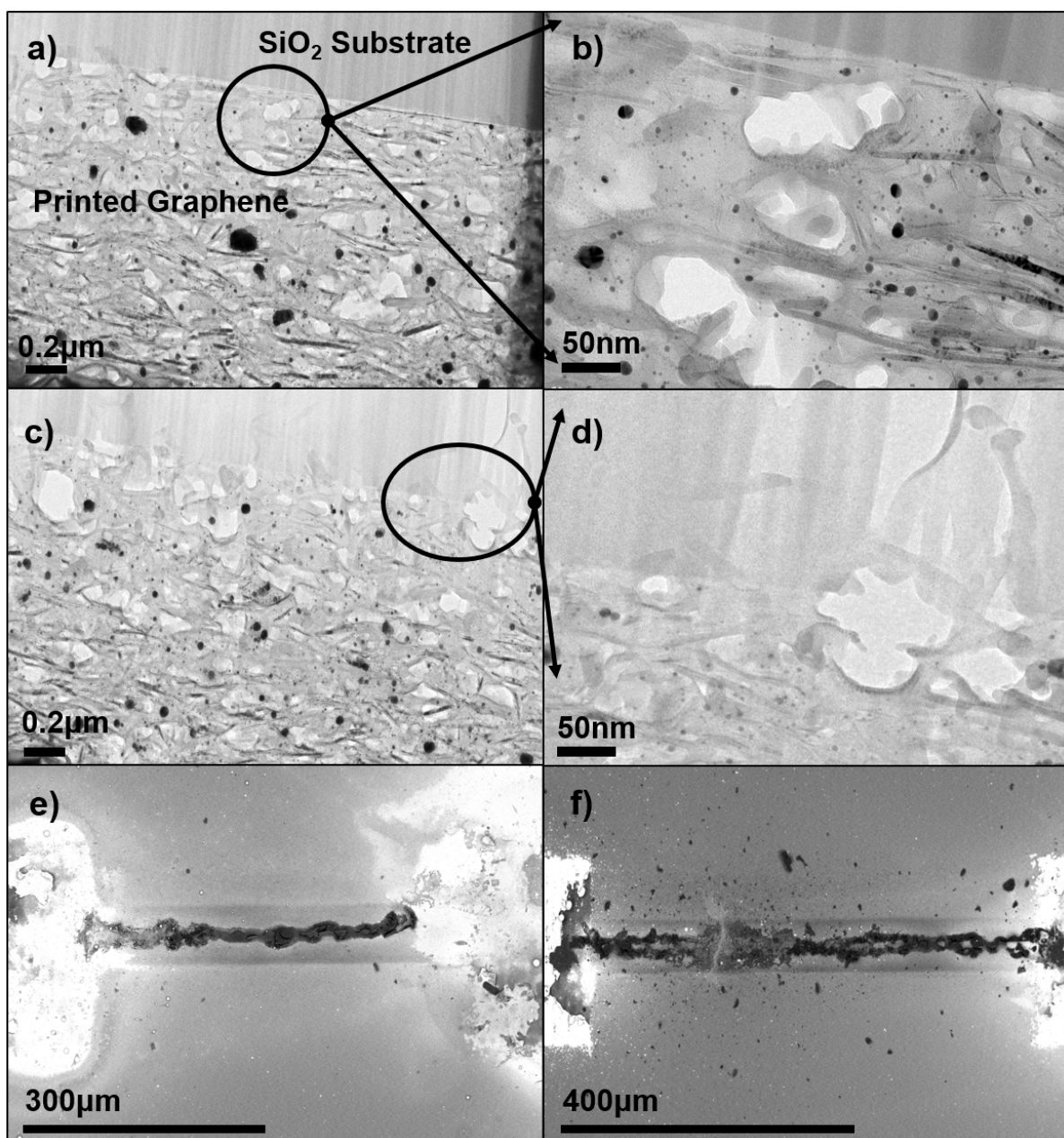


Figure 3.10 Investigating porosity and breakdown of the printed graphene interconnects: (a-b) and (c-d) Cross-section TEM images of the printed graphene interconnects on Si/SiO₂ for n=50 and (e and f) SEM images of different breakdown patterns of the printed graphene interconnects on Si/SiO₂.

3.4 Discussion

Graphene is known to have excellent thermal conductivity (exceeding $2000 \text{ W m}^{-1} \text{ K}^{-1}$)⁵⁹ and high charge carrier mobility ($\sim 120,000 \text{ cm}^2 \text{ V}^{-1} \text{ s}^{-1}$)⁶⁰, which makes it a desirable material for device applications. Nevertheless, the overall performance of

graphene devices can be limited by power dissipation, and the thermal resistance of the system.⁴⁰ Understanding the details of heat spreading (or Joule heating) in the system is important as it can limit the carrier mobility of graphene and the overall current density.⁴¹ Effects of Joule heating are influenced by device structure, thermal transport across material interfaces, and the choice of the substrate material.⁴¹ While several studies have examined the impact of Joule heating in graphene devices fabricated using graphene obtained by various synthesis techniques such as mechanical exfoliation, epitaxial growth on SiC, and CVD growth on transition metal substrates, this is the first to do so for AJP printed graphene interconnects.^{40–42,59,61–64} Our studies of power dissipation in AJP printed graphene interconnects indicate that power dissipation in AJP graphene is dominated by the graphene interconnect morphology for high thermal conductivity substrates but can be limited by the substrate properties in the case of low thermal conductivity polymer substrates typically used for flexible and wearable electronics applications.

Before concluding, we also wish to comment on the nature of the electrical breakdown of AJP deposited graphene interconnects. Electrical breakdown studies, which play a significant role in elucidating the current-carrying capability of the interconnects, have also been investigated for graphene, CNTs, and CNF (carbon nanofiber).^{51,53,58} Due to different structure-property-processing correlations, vastly different breakdown patterns are expected under high electric fields. Generally, Joule heating and/or oxidation breakdown results in a physical break perpendicular to the direction of current flow, as seen in GNRs and SWCNT devices.^{65–67} For CNTs, Joule heating, maybe the cause for breakdown at an early stage, but the main electric field and

oxidation breakdown mechanism is driven by percolative pathways.^{51,68} Moreover, Kitsuki *et al.* demonstrated the current induced breakdown of CNFs, and how the morphology of the graphitic layers comprising the CNFs play a significant role.⁵⁸ The cup-shaped features and voids observed can result in a quick break due to weak interlayer bonds of the graphitic layers.

This mechanism of CNFs breakdown can be applied to the AJP graphene breakdown due to their similar morphologies. This high porosity observed by the cross-section TEM images gives rise to a high thermal resistance within the interconnect and plays a significant role in the breakdown pattern of the graphene interconnects. **Figures 3.10e-f** show the breakdown patterns of n=20 graphene interconnect on SiO₂/Si used in this study. In both cases, we find a breakdown pattern parallel to the direction of the current flow. This type of breakdown pattern is likely due to the high porosity causing trapped gasses and solvents within the interconnect, as well as weak interlayer bonding of graphene flakes. As the device undergoes Joule heating, these trapped gases and fluids expand or vaporize, resulting in physical expansion and mechanical failure of the interconnect. This is particularly well captured in **Figure 3.10e**; we do not see a break perpendicular to the direction of current flow. However, **Figure 3.10f** shows both breakdown patterns suggesting a combination of a typical Joule heating and trapped gas/solvent driven breakdown for this device. Lastly, we note that the breakdown of AJP graphene on KaptonTM and Al₂O₃ was catastrophic with the substrate completely melting and destroying the graphene interconnect (for KaptonTM) and complete oxidation and disintegration of the interconnect (Al₂O₃) (see **Figure 3.11 and 3.12**). However, further detailed analysis of the fundamental breakdown mechanisms is beyond the scope of this

work and remains to be done in order to fully understand the physical nature of such breakdowns.

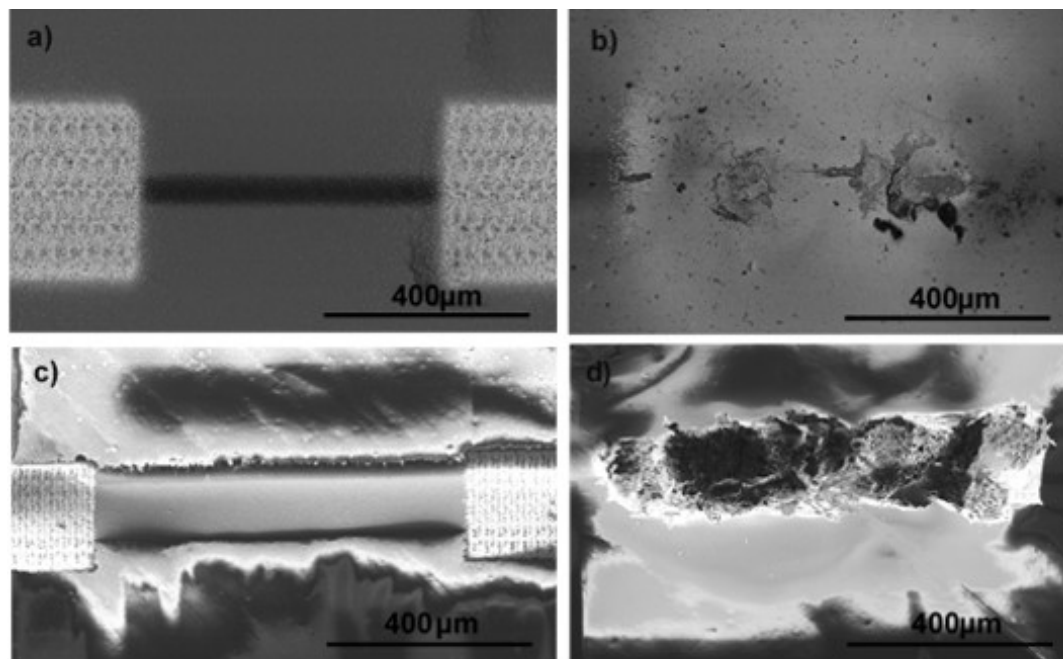


Figure 3.11 SEM images of the printed graphene interconnects on Al_2O_3 (a) and the corresponding breakdown image (b). Similarly, printed graphene interconnect SEM on KaptonTM (c) and the corresponding breakdown image (d).

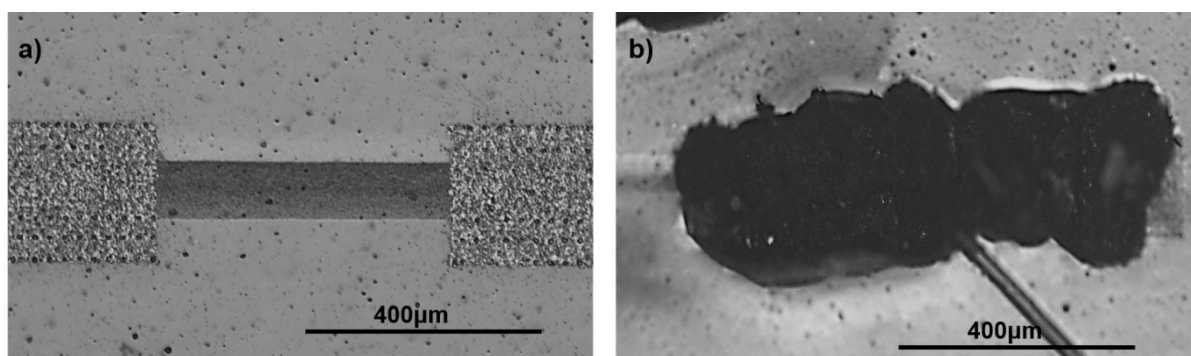


Figure 3.12 Optical images of an AJP graphene interconnect on KaptonTM (a) and a similar device after breakdown (b).

3.5 Conclusion

In summary, this study provides new insights into the electrical transport, and power dissipation of aerosol-jet printed graphene interconnects. Graphene inks printed via AJP into TLM structures exhibited physical, electrical, and thermal tunability based upon the number of print passes. Furthermore, electrical breakdown and infrared thermometry was performed to compare the power dissipation of the graphene printed interconnects on KaptonTM, SiO₂/Si, and Al₂O₃ substrates. The combination of IR imaging and COMSOL simulation captured the Joule heating of the printed graphene and emphasized the role of device morphology and the substrate in the power dissipation of printed graphene devices.

3.6 Methods

3.6.1 Preparation and Characterization of Graphene Ink

Similar to the processes described in Jabari et al. and Secor et al., graphene flakes were obtained by solvent assisted exfoliation of 50 mg/ml graphite powder in a suspension of 2% ethyl cellulose (EC) in ethanol using a Qsonica (Q125) probe tip sonicators for 90 min.^{8,28} To remove the larger graphite flakes, the dispersion was centrifuged (HeraeusTM MegafugeTM 8 Centrifuge) at 4500 RPM for 30 min and the supernatant was collected immediately. In a 1:2 volume ratio, the collected supernatant and 0.04 g/ml aqueous solution of NaCl (Sigma-Aldrich, >99.5%) was centrifuged for 15 min at 4500 RPM, to facilitate the flocculation of graphene flakes. The resulting graphene/EC dispersion was dried overnight on a PTFE plate. To tailor the concentration and viscosity of ink to the AJP, the dried graphene/EC paper was then dispersed by sonication for 30 min, in a mixture of 92.5% cyclohexanone and 7.5% terpineol solution,

followed by centrifugation at 4500rpm for 15 min. The resulting ink concentration, as seen in Figure 3.1a, is 3.5 mg/ml with a viscosity of 3.6 cP.

3.6.2 SEM, AFM, and TEM Imaging

A FEI Teneo (Hillsboro, OR), field emission SEM was used to image the printed films. Using the Dimatix inkjet printer, MLG and silver ink were used to print a transmission line measurement (TLM) structure with varying print passes from 15-30, with increments of 5 passes, on a glass substrate (seen in Figure 3.1a). The SEM image for the 25-layer pass line of IJP multilayered graphene is shown in Figure 3.1b to demonstrate its uniformity. TEM images were obtained using a JOEL JEM 2100 (Peabody, MA) system, with the particles characterized using ImageJ software. 25 and 30 printed passes of MLG were printed on untreated Kapton, and the TEM samples were prepared by a FIB (focused ion beam) tool at the Center for Advanced Energy Studies. Lastly, Raman spectra were obtained using a Horiba LabRAM HR Evolution Raman microscope (Irvine, CA) with a 532 nm excitation wavelength. The spectra (1000 – 3000 cm^{-1}) were collected at a relative laser power of 25% with a 100x objective and 30 s exposure time.

3.6.3 UV-VIS Spectroscopy

Ultraviolet-Visible (UV-VIS) absorption spectroscopy (Cary 5000G) was used to measure the optical absorbance of the graphene inks and quantify the graphene concentration. Using the Lambert-Beer law, $A = \alpha C_g l$, where A is the (absorbance), α (absorption coefficient), C_g (concentration of graphene), and l is (path length of the spectroscopy), a graphene concentration of 3.5mg/ml was measured. The previously

reported absorption coefficient at wavelength of 660nm ($\alpha_{660} = 2460 \text{ L/g-m}$) was used in the calculations.⁸

3.6.4 Thermogravimetric Analysis

In order to find the annealing temperature and oxidation temperature of the graphene, Thermogravimetric Analysis (TGA) was employed. A Netzsch TGA instrument was used to obtain the spectra of mass percent versus temperature. The mass of the dried graphene flakes (black) was analyzed as the temperature increased from 25°C to 1000°C at a heating rate of 5°C/min in air. TGA analysis revealed the decomposition peak of surfactant, ethyl cellulose, is around 250°C and oxidation /decomposition of the graphene is 550°C (see supplementary information Figure 3.9).

3.6.5 AJP of Graphene Interconnects

The graphene interconnects were printed using an AJ-300 Aerosol Jet printer manufactured by Optomec. The atomizer utilized was the UA-Max ultrasonic atomizer. A recirculating bath temperature of 15 °C was used to help stabilize the ink temperature and prevent the output from being too solvent rich. The tool platen was heated to 65 °C to help ensure rapid drying of the ink once on the substrate. The printing nozzle was a 100 μ ID ceramic, and the mist tube material was polyethylene. The power applied to the atomizer was 48W (48 volts at 1 amp). The sheath and atomizer flows were 50 and 20 sccm nitrogen respectively. The tool translation speed used was 1 mm/sec and the resulting single pass line width was measured to be ~50 μ . After printing any remaining solvent was driven out of the lines with a 100 °C bake for 10min followed by a ramp to 200 °C bake under a nitrogen purge for 30 min to maximize conductivity of the printed features.

3.6.6 Finite Element Model

In order to understand the heat dissipation and temperature distribution in our devices, we performed finite element simulations using COMSOL Multiphysics®. In our thermal model, the bottom boundary of the substrate and the outmost surface of the silver pad (which were in contact with the probe) were kept at the ambient temperature under the isothermal boundary condition ($T = T_{\text{ambient}}$). All other external boundaries were under the adiabatic boundary conditions if they are thermally insulating. Thermal properties of the substrates are $\kappa_{\text{OX}} = 1.4 \text{ Wm}^{-1}\text{K}^{-1}$, $\kappa_{\text{Si}} = 100 \text{ Wm}^{-1}\text{K}^{-1}$, $\kappa_{\text{Kapton}} = 0.12 \text{ Wm}^{-1}\text{K}^{-1}$, and $\kappa_{\text{Al}_2\text{O}_3} = 32 \text{ Wm}^{-1}\text{K}^{-1}$. Thermal conductivities of graphene interconnect are assumed at $\kappa_{\perp} = 2 \text{ Wm}^{-1}\text{K}^{-1}$ and $\kappa_{\parallel} = 50 \text{ Wm}^{-1}\text{K}^{-1}$ for cross-plane and in-plane directions, respectively. These values are significantly lower than those of pristine graphene because of the nature of printed graphene. The thermal interface resistance between graphene interconnect and substrates R_{int} were fitted to be between $1.0 \times 10^{-7} \text{ m}^2\text{K/W}$ to $1.0 \times 10^{-8} \text{ m}^2\text{K/W}$.

3.7 Acknowledgements

This work was funded by startup funds from the Micron School of Materials Science and Engineering; by the Air Force Office of Scientific Research Summer Faculty Fellowship Program; by the Idaho NASA EPSCoR Office; and by the Air Force Research Laboratory – Minority Leadership Program. M.T.S, S.K, and F.X. acknowledges support from startup funds from the Swanson School of Engineering at University of Pittsburgh. The authors acknowledge the Boise State Surface Science Laboratory for help with AFM imaging and the Microscopy and Characterization Suite at the Center for Advanced Energy Studies for help with cross-sectional TEM sample preparation.

3.8 Reference

1. Kenry *et al.* Emerging flexible and wearable physical sensing platforms for healthcare and biomedical applications. *Microsystems Nanoeng.* **2**, 16043 (2016).
2. Kim, S. J., Choi, K., Lee, B., Kim, Y. & Hong, B. H. Materials for flexible, stretchable electronics: graphene and 2D materials. *Annu. Rev. Mater. Res.* **45**, 63–84 (2015).
3. Singh, E., Meyyappan, M. & Nalwa, H. S. Flexible graphene-based wearable gas and chemical sensors. *ACS Appl. Mater. Interfaces* **9**, 34544–34586 (2017).
4. Stoppa, M. & Chiolerio, A. Wearable electronics and smart textiles: A critical review. *Sensors (Switzerland)* **14**, 11957–11992 (2014).
5. Kim, C. S., Ahn, S. H. & Jang, D. Y. Review: Developments in micro/nanoscale fabrication by focused ion beams. *Vacuum* **86**, 1014–1035 (2012).
6. Westervelt, R. M. & Westervelt, R. M. Graphene nanoelectronics. *Science (80-.)*. **322**, 2007–2008 (2008).
7. Campbell, S. A. *The Science and Engineering of Microelectronic Fabrication*. Oxford University Press **476**, (2001).
8. Jabari, E. & Toyserkani, E. Micro-scale aerosol-jet printing of graphene interconnects. *Carbon N. Y.* **91**, 321–329 (2015).
9. Torrisi, F. *et al.* Inkjet-printed graphene electronics. *ACS Nano* **6**, 2992–3006 (2012).
10. Zhan, Z. *et al.* Inkjet-printed optoelectronics. *Nanoscale* **9**, 965–993 (2017).
11. Renn, M. J. Aerosol-jet printed thin film transistors. *WHITEPAPER - Optomec* 3–5 (2010).
12. Clinton, R. G. *NASA's In Space Manufacturing Initiative and Additive Manufacturing Development for Rocket Engine Space Flight Hardware*. (2016).
13. Bucella, S. G., Nava, G., Vishunubhatla, K. C. & Caironi, M. High-resolution direct-writing of metallic electrodes on flexible substrates for high performance organic field effect transistors. *Org. Electron.* **14**, 2249–2256 (2013).
14. Seifert, T. *et al.* Additive manufacturing technologies compared: Morphology of deposits of silver ink using inkjet and aerosol jet printing. *Ind. Eng. Chem. Res.* **54**, 769–779 (2015).

15. Kordás, K. *et al.* Inkjet Printing of Electrically Conductive Patterns of Carbon Nanotubes. *Small* **2**, 1021–1025 (2006).
16. Cao, C., Andrews, J. B. & Franklin, A. D. Completely Printed, flexible, stable, and hysteresis-free carbon nanotube thin-film transistors via aerosol jet printing. *Adv. Electron. Mater.* **3**, (2017).
17. Jariwala, D., Sangwan, V. K., Lauhon, L. J., Marks, T. J. & Hersam, M. C. Carbon nanomaterials for electronics, optoelectronics, photovoltaics, and sensing. *Chem. Soc. Rev.* **42**, 2824–2860 (2013).
18. Hersam, M. C. Progress towards monodisperse single-walled carbon nanotubes. *Nat. Nanotechnol.* **3**, 387–394 (2008).
19. Geim, A. K. & Novoselov, K. S. The rise of graphene. *Nat. Mater.* **6**, 183–191 (2007).
20. Schedin, F. *et al.* Detection of individual gas molecules adsorbed on graphene. *Nat. Mater.* **6**, 652–655 (2007).
21. Salehi-Khojin, A. *et al.* Chemical sensors based on randomly stacked graphene flakes. *Appl. Phys. Lett.* **100**, (2012).
22. Kumar, B. *et al.* The role of external defects in chemical sensing of graphene field-effect transistors. *Nano Lett.* **13**, 1962–1968 (2013).
23. Amin, K. R. & Bid, A. Graphene as a sensor. *Curr. Sci.* **107**, 430–436 (2014).
24. Banerjee, S. *et al.* Electrochemistry at the edge of a single graphene layer in a nanopore. *ACS Nano* **7**, 834–843 (2013).
25. Chen, D. *et al.* Graphene-based materials in electrochemistry. *Chem. Soc. Rev.* **39**, 3157 (2010).
26. Ambrosi, A., Chua, C. K., Bonanni, A. & Pumera, M. Electrochemistry of graphene and related materials. *Chem. Rev.* **114**, 7150–88 (2014).
27. Li, J. *et al.* Efficient Inkjet Printing of Graphene. *Adv. Mater.* **25**, 3985–3992 (2013).
28. Secor, E. B., Prabhumirashi, P. L., Puntambekar, K., Geier, M. L. & Hersam, M. C. Inkjet printing of high conductivity, flexible graphene patterns. *J. Phys. Chem. Lett.* **4**, 1347–1351 (2013).
29. Dua, V. *et al.* All-organic vapor sensor using inkjet-printed reduced graphene oxide. *Angew. Chemie - Int. Ed.* **49**, 2154–2157 (2010).

30. Hondred, J. A. *et al.* Printed Graphene Electrochemical Biosensors Fabricated by Inkjet Maskless Lithography for Rapid and Sensitive Detection of Organophosphates. *ACS Appl. Mater. Interfaces* **10**, 11125–11134 (2018).
31. Hernandez, Y. *et al.* High-yield production of graphene by liquid-phase exfoliation of graphite. *Nat. Nanotechnol.* **3**, 563–568 (2008).
32. Stankovich, S. *et al.* Synthesis of graphene-based nanosheets via chemical reduction of exfoliated graphite oxide. *Carbon N. Y.* **45**, 1558–1565 (2007).
33. Salehi-khojin, A. *et al.* Chemical sensors based on randomly stacked graphene flakes. **33111**, 9–12 (2012).
34. Cinti, S. & Arduini, F. Graphene-based screen-printed electrochemical (bio)sensors and their applications: Efforts and criticisms. *Biosensors and Bioelectronics* **89**, 107–122 (2017).
35. Xin, G. *et al.* Large-area freestanding graphene paper for superior thermal management. *Adv. Mater.* **26**, 4521–4526 (2014).
36. Yan, C., Wang, J. & Lee, P. S. Stretchable graphene thermistor with tunable thermal index. *ACS Nano* **9**, 2130–2137 (2015).
37. Michel, M. *et al.* A thermally-invariant, additively manufactured, high-power graphene resistor for flexible electronics. *2D Mater.* **4**, 025076–025086 (2017).
38. Aga, R. S. *et al.* In situ study of current-induced thermal expansion in printed conductors using stylus profilometry. *Flex. Print. Electron.* **1**, (2016).
39. Aga, R. S. *et al.* Considerations in printing conductive traces for high pulsed power applications. *Microelectron. Reliab.* **81**, 342–351 (2018).
40. Bae, M. H., Ong, Z. Y., Estrada, D. & Pop, E. Imaging, simulation, and electrostatic control of power dissipation in graphene devices. *Nano Lett.* **10**, 4787–4793 (2010).
41. Pop, E. Energy dissipation and transport in nanoscale devices. *Nano Research* **3**, 147–169 (2010).
42. Xu, Z. & Buehler, M. J. Heat dissipation at a graphene–substrate interface. *J. Phys. Condens. Matter* **24**, 475305 (2012).
43. Yu, Y. J. *et al.* High-resolution spatial mapping of the temperature distribution of a Joule self-heated graphene nanoribbon. *Appl. Phys. Lett.* **99**, 2009–2012 (2011).
44. Beechem, T. E. *et al.* Self-Heating and Failure in Scalable Graphene Devices. *Sci. Rep.* **6**, 26457 (2016).

45. Grosse, K. L., Bae, M.-H., Lian, F., Pop, E. & King, W. P. Nanoscale Joule heating, Peltier cooling and current crowding at graphene–metal contacts. *Nat. Nanotechnol.* **6**, 287–290 (2011).
46. Rao, K. S., Senthilnathan, J., Liu, Y.-F. F. & Yoshimura, M. Role of peroxide ions in formation of graphene nanosheets by electrochemical exfoliation of graphite. *Sci. Rep.* **4**, 4237 (2014).
47. Cañado, L. G. *et al.* General equation for the determination of the crystallite size l_a of nanographite by Raman spectroscopy. *Appl. Phys. Lett.* **88**, (2006).
48. Schroder, D. K. *Semiconductor material and device characterisation. Physics Today* **44**, (2006).
49. Cho, D.-H. *et al.* Effect of surface morphology on friction of graphene on various substrates. *Nanoscale* **5**, 3063 (2013).
50. Freitag, M. *et al.* Energy dissipation in graphene field-effect transistors. *Nano Lett.* **9**, 1883–1888 (2009).
51. Estrada, D. & Pop, E. Imaging dissipation and hot spots in carbon nanotube network transistors. **98**, 1–11 (2011).
52. Gupta, M. P. *et al.* High field breakdown characteristics of carbon nanotube thin film transistors. *Nanotechnology* **24**, (2013).
53. Pop, E. The role of electrical and thermal contact resistance for Joule breakdown of single-wall carbon nanotubes. *Nanotechnology* **19**, (2008).
54. Dorgan, V. E., Bae, M. H. & Pop, E. Mobility and saturation velocity in graphene on SiO₂. *Appl. Phys. Lett.* **97**, (2010).
55. Grosse, K. L. *et al.* Direct observation of resistive heating at graphene wrinkles and grain boundaries. *Appl. Phys. Lett.* **105**, (2014).
56. Dupont. DuPont™ Kapton®. <http://www.dupont.com/content/dam/dupont/products-and-services/membranes-and-films/polyimide-films/documents/DEC-Kapton-summary-of-properties.pdf> **50**, 1–7 (2012).
57. Pishchik, V., Lytvynov, L. A. & Dobrovinskaya, E. R. *Sapphire. Sapphire: Material, Manufacturing, Applications* (Springer US, 2009). doi:10.1007/978-0-387-85695-7
58. Kitsuki, H. *et al.* Current-induced breakdown of carbon nanofibers for interconnect applications. *2007 7th IEEE Int. Conf. Nanotechnol. - IEEE-NANO 2007, Proc.* **114307**, 342–345 (2007).

59. Balandin, A. a *et al.* Superior thermal conductivity of single-layer graphene 2008. *Nano Lett.* **8**, 902–907 (2008).
60. Bolotin, K. I., Sikes, K. J., Hone, J., Stormer, H. L. & Kim, P. Temperature-dependent transport in suspended graphene. *Phys. Rev. Lett.* **101**, (2008).
61. Prakash Gupta, M. *et al.* Impact of thermal boundary conductances on power dissipation and electrical breakdown of carbon nanotube network transistors. *J. Appl. Phys.* **112**, (2012).
62. Li, X., Kong, B. D., Zavada, J. M. & Kim, K. W. Strong substrate effects of Joule heating in graphene electronics. *Appl. Phys. Lett.* **99**, 10–14 (2011).
63. Ghosh, S. *et al.* Extremely high thermal conductivity of graphene: Prospects for thermal management applications in nanoelectronic circuits. *Appl. Phys. Lett.* **92**, 1–4 (2008).
64. Lee, K., Moon, J.-S., Oh, T., Kim, S. & Asbeck, P. Analysis of heat dissipation of epitaxial graphene devices on SiC. *Solid. State. Electron.* **101**, 44–49 (2014).
65. Xiong, F., Liao, A. D., Estrada, D. & Pop, E. Low-power switching of phase-change materials with carbon nanotube electrodes. *Science (80-.).* **332**, 568–570 (2011).
66. Liao, A. *et al.* Thermal dissipation and variability in electrical breakdown of carbon nanotube devices. *Phys. Rev. B - Condens. Matter Mater. Phys.* **82**, (2010).
67. Liao, A. D. *et al.* Thermally limited current carrying ability of graphene nanoribbons. *Phys. Rev. Lett.* **106**, (2011).
68. Shekhar, S., Heinrich, H. & Khondaker, S. I. Huge volume expansion and structural transformation of carbon nanotube aligned arrays during electrical breakdown in vacuum. *Carbon N. Y.* **50**, 1635–1643 (2012).

CHAPTER FOUR: FULLY INKJET-PRINTED MULTILAYERED GRAPHENE-
BASED FLEXIBLE ELECTRODES FOR ELECTROCHEMICAL PERFORMANCE

Twinkle Pandhi,¹ Casey Cornwell,² Kiyu Fujimoto,¹ Pete Barnes,¹ Jasmine Cox,³ Hui Xiong,¹ Paul H. Davis,¹ Harish Subbaraman,³ Jessica E. Koehne,⁴ and David Estrada^{1,5*}

¹Micron School of Materials Science and Engineering, Boise State University, Boise, ID
83725-2090, United States

²Department of Chemistry, Northwest Nazarene University, Nampa, ID 83686, United
States

³Department of Electrical and Computer Engineering, Boise State University, Boise, ID
83725-2075, United States

⁴NASA Ames Research Center, Moffett Field, CA 94035, United States

⁵Center for Advanced Energy Studies, Boise State University, Boise, ID 83725-1012,
United States

* Corresponding Author: daveestrada@boisestate.edu

Reproduced with permission from RSC Advances

RSC Adv., 2020,10, 38205-38219

<https://doi.org/10.1039/D0RA04786D>

No significant changes were made to this publication.

4.1 Abstract

Graphene has proven to be useful in biosensing applications. However, one of the main hurdles with printed graphene-based electrodes is achieving repeatable electrochemical performance from one printed electrode to another. We have developed a consistent fabrication process to control the sheet resistance of inkjet-printed graphene electrodes, thereby accomplishing repeatable electrochemical performance. Herein, we investigated the electrochemical properties of multilayered graphene (MLG) electrodes fully inkjet-printed (IJP) on flexible Kapton substrates. The electrodes fabricated by inkjet printing three materials – (1) a conductive silver ink for electrical contact, (2) an insulating dielectric ink, and (3) MLG ink as the sensing material. The selected materials and fabrication methods provided great control over the ink rheology and material deposition, which enabled stable and repeatable electrochemical response: bending tests revealed the electrochemical behavior of these sensors remained consistent over 1000 bend cycles. Due to the abundance of structural defects (e.g., edge defects) present in the exfoliated graphene platelets, cyclic voltammetry (CV) of the graphene electrodes showed good electron transfer ($k = 1.125 \times 10^{-2}$ cm/s) with a detection limit (0.01 mM) for ferric/ferrocyanide redox couple, $[\text{Fe}(\text{CN})_6]^{-3/4}$, which is comparable or superior to modified graphene or graphene oxide-based sensors. Additionally, the potentiometric response of the electrodes displayed good sensitivity over the pH range of 4-10. Moreover, a fully IJP three-electrode device (MLG, platinum, and Ag/AgCl) also showed quasi-reversible compared to a single IJP MLG electrode device. These findings demonstrate significant promise for scalable fabrication of a flexible, low cost, and fully-

IJP wearable sensor system needed for space, military, and commercial biosensing applications.

Keywords: Graphene, Inkjet Printing, Flexible Electronics, Electrochemistry, pH sensing, Biosensing

4.2 Introduction

Graphene has been used for many electrochemical applications, such as in fuel cells, electric double-layer capacitors, and lithium-ion batteries.¹⁻⁵ So far, research has been conducted for graphene oxide electrodes, screen printed graphene electrodes, and IJP graphene electrodes modified with PEDOT-PSS or polyaniline, but fully IJP printed bare graphene-based electrodes with high stability, sensitivity, and repeatability have not been developed.^{2,6-18} Conventional fabrication processes for sensor development, such as vacuum deposition, photolithography, and epitaxial growth of electronic materials, tend to be complicated and expensive, often requiring lithographic patterning and high-temperature processing.¹⁹ As a result, additive electronics manufacturing techniques, such as inkjet printing (IJP), aerosol jet printing (AJP), and micro-dispense printing (MDP), are being explored as potential low-cost scalable fabrication methods for flexible sensor systems.²⁰⁻²⁴ Previous studies have demonstrated that inkjet printing, a drop-on-demand process, eliminates the need for the prefabricated masks or stencils required for lithographic and contact-printing processes.²⁵⁻²⁸ An inkjet-printed ion-selective single layer reduced graphene oxide-based sensor by Claussen *et al.* demonstrated a wide sensing range and low detection limits.²⁹ However, such studies involved rigid substrates and high annealing temperatures that are not compatible with flexible substrates or included lithographic processes in the overall device design.

Over the last two decades, carbon-based materials such as graphene or functionalized/doped graphene, glassy carbon, carbon nanotubes (CNTs), fullerenes, and boron-doped diamond have been investigated for their use as electrodes in electrochemical sensing due to their advantageous structural and electrical properties.^{13,18,30-36} As each carbon allotrope possesses a unique structure and surface chemistry, the electrochemical behavior of each is also unique. For electrochemical applications, highly ordered pyrolytic graphite, pseudographite, graphene, and orientated CNTs are excellent candidates due to their high conductivity, large surface area, and unique heterogeneous electron transfer rates.^{32,35,37}

Graphene, a monolayer of sp^2 hybridized carbon in a 2-dimensional hexagonal lattice structure, has received much attention in the research community due to its unique physical and chemical properties. The sp^2 bonding between the carbon atoms in graphene creates three σ -bonds, which are responsible for its high mechanical strength and high in-plane thermal conductivity.³⁸⁻⁴² Graphene's remarkable conductivity is associated with overlapping p_z orbitals above and below the molecular plane, which creates a delocalized π - electron system to allow for free movement of electrons. These unique bonding characteristics give rise to a linear band structure with a zero-band gap near the K and K' points, leading to graphene's high electrical conductivity.^{39,43} Moreover, graphene makes for an excellent candidate for electrochemical applications due to its high conductivity, large surface area, unique heterogeneous electron transfer rate, and low production cost. The edge plane and basal plane-defect sites of the highly ordered pyrolytic graphite greatly favors electrochemical activity.^{2,18} Three common techniques used to obtain graphene are exfoliation, chemical vapor deposition (CVD), and epitaxial growth. While

these are widely used techniques, they are known to introduce defects to the graphene structure that are detrimental to electrical and thermal transport properties, while conversely improving chemical and electrochemical sensitivity.^{1,5,42,44–48}

The method of fabricating electrochemical graphene sensors is vital in creating edge and basal plane defects to improve chemical sensitivity. Work such as Banerjee *et al.* reported ultrahigh electrochemical current densities for graphene edges embedded in dielectric nanopores.¹ Yuan *et al.* further demonstrated that the electrochemical activity on the edge states of single-layer CVD grown graphene is higher than on the basal plane.⁴⁹ Shang *et al.* showed that increased graphitic edge and basal plane defects in CVD grown multilayer graphene resulted in superior electron transfer kinetics compared to the edge state of highly ordered pyrolytic graphite.⁵⁰ Fisher *et al.* used microwave plasma-enhanced chemical vapor deposition grown multilayered graphene petal nanosheets to develop a versatile glucose sensor on a silicon wafer with high sensitivity, selectivity, and stability.⁵¹ Furthermore, Tang *et al.* showed excellent electrocatalytic activity for reduced graphene oxide sheets synthesized by chemical exfoliation and cast onto a glassy carbon electrode.⁵² We chose a high yield, solvent assisted exfoliation method to synthesize multilayer graphene to retain a desirable edge and basal-plane defects that promote electrochemical activity. Moreover, it has been previously shown that the annealing conditions, ink properties, and number of print passes impact the electrical and structural porosity of printed graphene microstructures.⁵³ Such porosity in functionalized graphene electrodes has a significant impact on enhancing the electrochemical performance as well.⁵⁴

In this report, the electrochemical performance of IJP MLG electrodes and fully IJP three-electrode sensors is investigated by measuring the cyclic voltammetry response of a ferric/ferrocyanide redox couple and by performing pH sensitivity studies. Additionally, the effect of electrode porosity is examined with a comparison between the electrochemical performance of MLG electrodes having different porosities as a result of the printing process. It is observed that the structure-property-processing correlations of fully additively manufactured graphene-based electrochemical electrodes are essential factors in improving consistency, repeatability, and uniformity of such fully printed sensor systems. Finally, the IJP MLG electrodes are shown to exhibit robust electrochemical performance over 1000 bend cycles, highlighting the attractive properties and behavior of IJP MLG electrodes for use in wearable electroanalysis. Advances such as this will further enable additive electronics manufacturing of flexible sensors for human performance monitoring in space, military, and commercial applications.

4.3 Results and Discussions

4.3.1 Inkjet Printing of Graphene Electrodes

Inkjet printing of graphene has been well established,^{4,10,11} and several groups have demonstrated inkjet-printed graphene chemical¹² and biological¹³ sensors. Graphene inks are typically produced through liquid-phase exfoliation of graphite or chemical or thermal reduction of graphene oxide.^{14,15} These processes usually result in submicron graphene crystal domains and give rise to numerous point defects within the lattice, and closed-contour defects around the flake's edge.⁹ Under applied electrical bias, these defects result in highly localized electric fields, which can be modified by absorbed molecules/target analytes. Combined with the high electrical conductivity and specific

surface area of graphene, these defects enable highly sensitive graphene-based sensors to detect target molecules with parts per billion sensitivity in controlled environments.^{9,55} Furthermore, as inkjet is typically a drop-on-demand process, the microstructure of inkjet-printed graphene typically results in a well-layered structure with varying amounts of porosity, depending on annealing conditions, ink properties, and the number of print passes.

Microstructural and electrical characterization was performed on multilayered graphene (MLG) printed lines with silver contact pads in a transmission line measurement (TLM) structure with varying numbers of print passes (15-30, in increments of 5 passes) using a Dimatix inkjet printer (seen in **Figure 4.1a**). To minimize interference due to excessive charging and fluorescence from the large surface roughness of Kapton HN substrates, the MLG and silver TLM structures for microstructural and electrical characterization were printed on glass instead. The tool platen temperature, nozzle diameter, and cartridge temperature were optimized to ensure that the dimensions and material deposition were adequate to obtain uniform structures. Scanning electron microscopy (SEM) of a line with 25 print passes of IJP multilayered graphene (**Figure 4.1b - left**) demonstrated good uniformity of the printed layer. Transmission electron microscopy (TEM) (**Figure 4.1b - right**) showed multilayer graphene flakes ranging in thickness from 5-20 nm layers. The surfactant ethyl cellulose (EC) stabilized the graphene flakes in the solution but required decomposition after printing to achieve

optimal electrical conductivity. Thermal gravimetric analysis (TGA) was employed to analyze the EC coated graphene flakes' thermal stability.

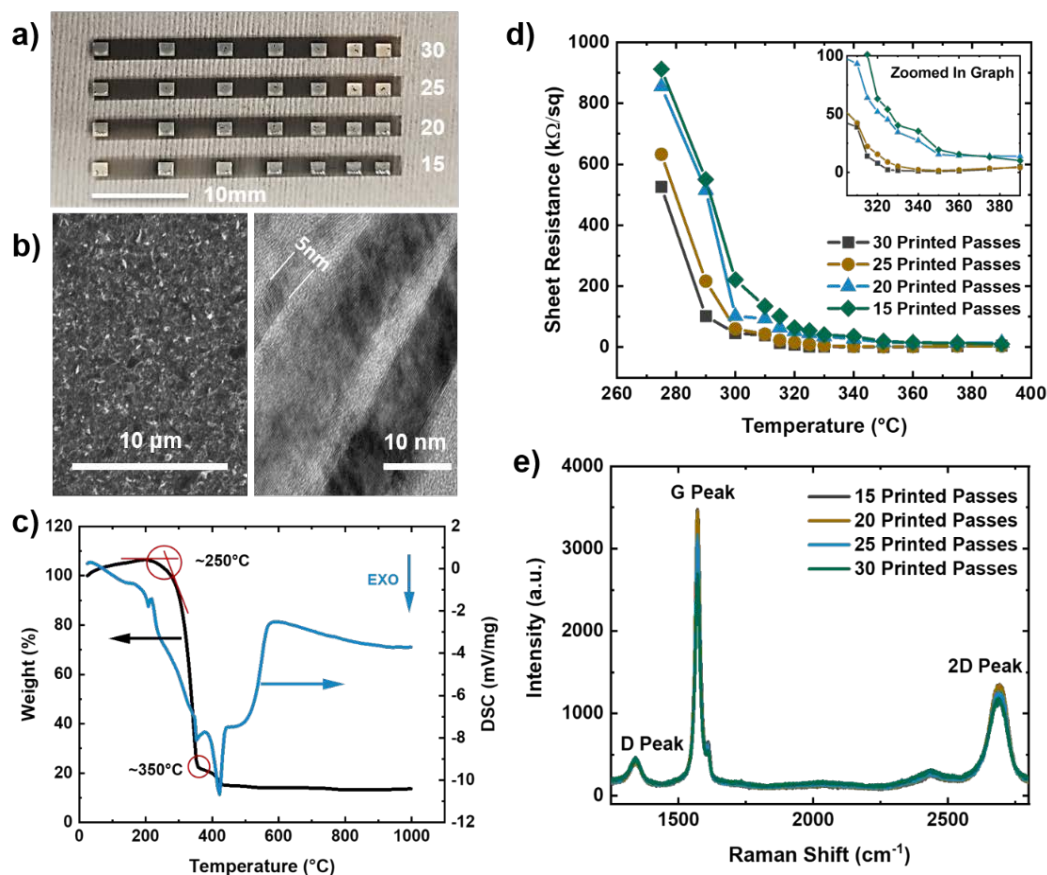


Figure 4.1 Inkjet-printed graphene layer characterization. a) Optical image of inkjet-printed graphene (15-30 printed passes) structure on the glass. b) SEM image of the 25-pass printed line (left) and TEM image of the multilayer graphene flakes (right) on Kapton HN. c) TGA and DSC data of the graphene/ethylcellulose ink. d) Sheet resistance vs. temperature for 15 to 30 printed passes on the glass. e) Typical Raman spectra (532 nm excitation) for 15 to 30 printed passes MLG films.

Figure 4.1c shows weight percent (black) and differential scanning calorimetry (blue) as a function of temperature. The decomposition peak of EC occurs at around 250 °C, while the decomposition temperature of the solvents is seen around 350 °C. Using the TGA, the graphene printed structures were then annealed in two stages: first at 250 °C for 30 minutes to evaporate the surfactant, and subsequently at 350 °C for another 30

minutes to remove the remaining solvents, leading to enhanced electrical conductivity. The silver contacts were deposited via IJP on top of the graphene in a TLM structure using commercially available 40 wt % silver ink.

To measure the electrical properties of the printed interconnects, a 2-point probe (Keithley 4200 SCS, Textronix, Beaverton, OR) measurements on the TLM structure were conducted. **Figure 4.1d** shows the calculated sheet resistance as a function of annealing temperature for 15 - 30 print passes. Based on the TLM measurements, the lowest sheet resistance was calculated to be 0.89 k Ω /sq, and 1.60 k Ω /sq for 30 and 25 print passes, respectively, at an annealing temperature of 350°C. Moreover, Raman spectroscopy results are shown in **Figure 4.1e** reveal the graphitic nature of our electrodes through the characteristic D, G, and 2D peaks for the IJP graphene layers at 1350 cm⁻¹, 1580 cm⁻¹, and 2700 cm⁻¹, and I_{2D}/I_G peak ratios in the range of 0.38-0.43.⁵⁶

4.3.2 Electrochemical Response of MLG Electrodes

To investigate our IJP MLG electrode's electrochemical properties, the synthesized MLG was printed into 1 cm × 1 cm squares (15, 20, 25, and 30 printed passes) with silver contact pads (1 printed layer) and SU-8 (3 printed passes) as a passivation layer for the silver electrode. All layers were printed by IJP on two mil thick untreated Kapton HN film (**Figure 4.2 a,b**). Before printing MLG ink on Kapton, contact angle (CA) measurements of MLG inks on a Kapton HN substrate were performed to ensure wettability. In **Figure 4.2c**, we present a low CA of 15.6°, suggesting good wettability of MLG ink on untreated Kapton HN substrates. An example of the flexible and fully printed MLG electrode with 25-layer print passes on Kapton HN is seen in **Figure 4.2d**.

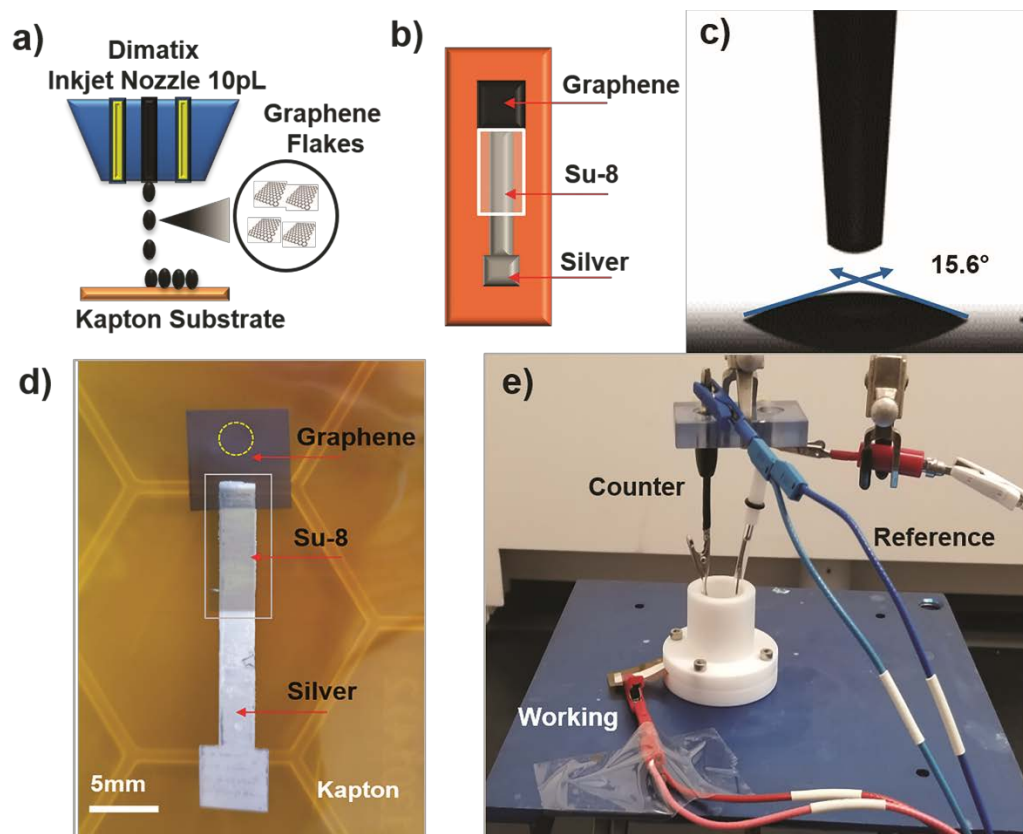


Figure 4.2 a) Sketch of the Dimatix inkjet printer printing graphene on Kapton. b) Design and layers of the graphene electrode. c) Contact angle measurements of graphene ink on Kapton. d) Optical image of the printed graphene electrode, where the yellow ring indicates the surface area of the electrode exposed to the electrolyte. e) Photograph of the electrochemical experimental setup of the graphene electrode in aqueous ferricyanide redox couple with Ag/AgCl as the reference electrode and platinum wire as the counter electrode.

The experimental setup to study the electrochemical response of printed MLG electrodes is shown in **Figure 4.2e**, like the setups used by Munoz and Richter.^{58–61} Cyclic voltammetry (CV) measurements were carried out with a Bio-Logic VMP-300 potentiostat with scan rates from 10–100 mV/s in 1 mM $[\text{Fe}(\text{CN})_6]^{-3/4}$ with 1 M KCl as the supporting electrolyte, at room temperature for MLG working electrodes made by 15 to 30 printed passes (**Figure 4.3a,b** for 25 and 30 printed passes and **Figure 4.4a,b** for 15 and 20 printed passes). Ferro/ferri cyanide redox couple is often used in physiological experiments because of its sensitivity to relatively small changes on the surface and

widely been used for carbon electrodes. The iron is low spin and quickly reduce to the ferric/ferrocyanide $[\text{Fe}(\text{CN})_6]^{-3/4}$.¹³ For this experiment, the electrochemical cell is comprised of an IJP MLG working electrode, a standard platinum wire counter electrode, and a conventional aqueous Ag/AgCl/KCl (sat.) reference electrode with saturated (sat.) KCl solution from SYC Technologies. A $\sim 0.07 \text{ cm}^2$ circular surface area of IJP MLG is defined by the size of the O-ring in the liquid cell. Studies were performed with the 25 and 30 printed pass electrodes due to their superior electrochemical performance. The observed electrochemical behavior was evaluated, as can be seen from the CV curves in **Figure 4.3**, distinct redox peaks can be observed.

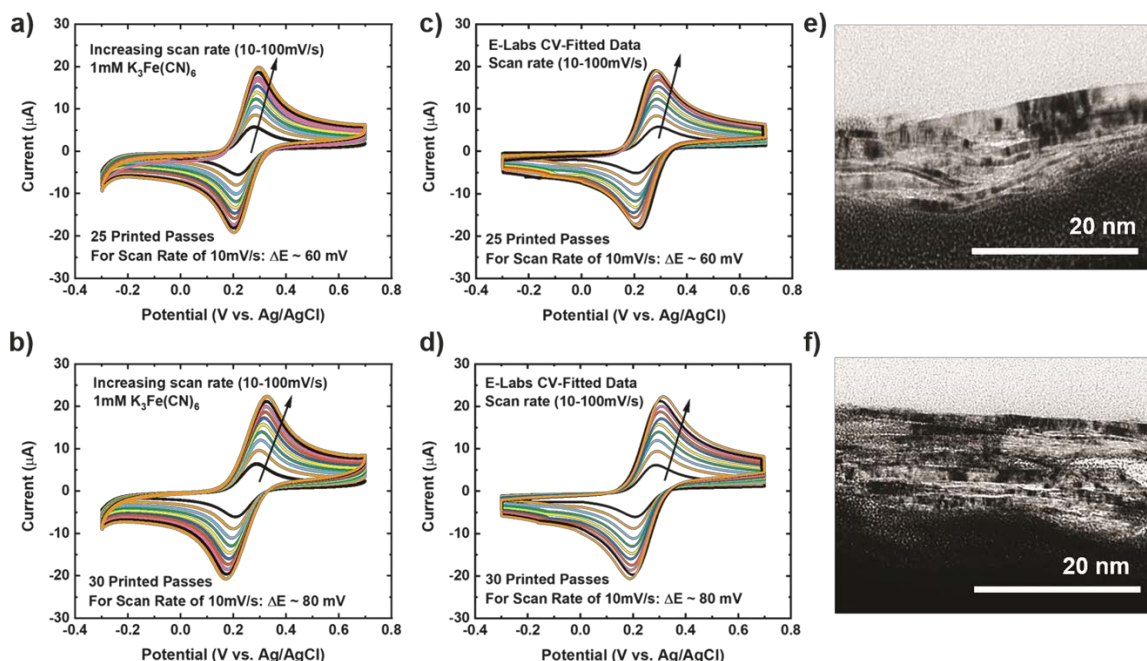


Figure 4.3 Graphene electrode cyclic voltammetry (CV) scan rate data for 1 mM $[\text{Fe}(\text{CN})_6]^{-3/4}$ in 1M KCl as the supporting electrolyte with increasing scan rate 10mV/s-100mV/s for a) 25 printed passes of graphene and b) 30 printed passes of graphene. E-labs CV-Sim fitted data for c) 25 printed passes of graphene and d) 30 printed passes of graphene. Cross-section TEM images of e) 25 printed passes graphene and f) 30 printed passes graphene.

The 25 printed passes of MLG electrode exhibits quasi-reversible CV characteristics with a peak to peak separation ~ 60 mV at a scan rate of 10 mV/s in a 1 mM dilution of $[\text{Fe}(\text{CN})_6]^{-3/4}$. This peak to peak separation (i.e., near-ideal ΔE_p of 59 mV for Nernstian reactions) is evidence of the fast electrode kinetics, while shifts in peak to peak separation with an increase in scan rate point to the electrodes' quasi-reversible nature.

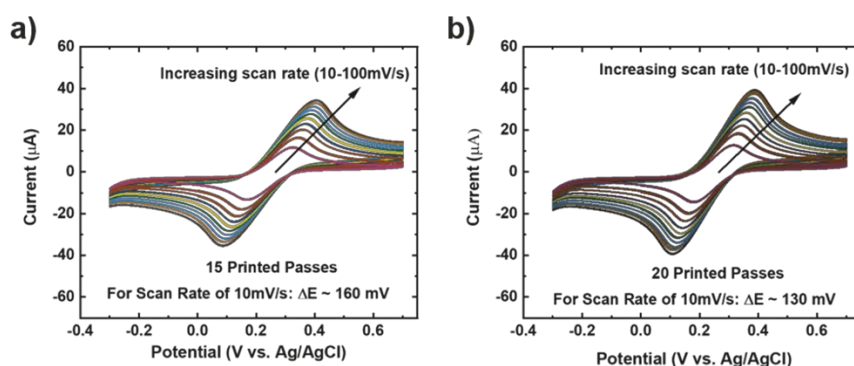


Figure 4.4 (a) 15 printed passes and (b) 20 printed passes cyclic voltammetry (CV) scans for 5 mM $[\text{Fe}(\text{CN})_6]^{-3/4}$ in 1 M KCl as the supporting electrolyte with increasing scan rate from 10 to 100 mV/s

The kinetics (extracted dimensionless coefficient φ) of our IJP MLG electrode (25.14) is compared with that of other comparable graphene-based electrodes and inkjet-printed electrodes in **Table 4.2**. Electrodes shaded in pink shows functionally of a fully printed three-electrode sensor system. Our electrode shows much better reversibility, stability, and repeatability on a flexible substrate than the other electrodes. Our data suggest that IJP MLG electrodes possess well-defined structures and electrochemical properties to support fast kinetics, comparable to results presented in the literature for MLG.⁵¹ Although 30 printed passes of MLG shows a higher current and lower sheet resistance than 25 printed passes, a higher peak to peak separation of 80 mV (**Figure 4.3b**) is observed. It is hypothesized that while the additional printed passes for the (30 printed passes sample) electrode increase uniformity and decrease resistance, they also

create denser packing of the graphene flakes, thereby reducing the porosity and slowing the redox reaction on the electrode surface.

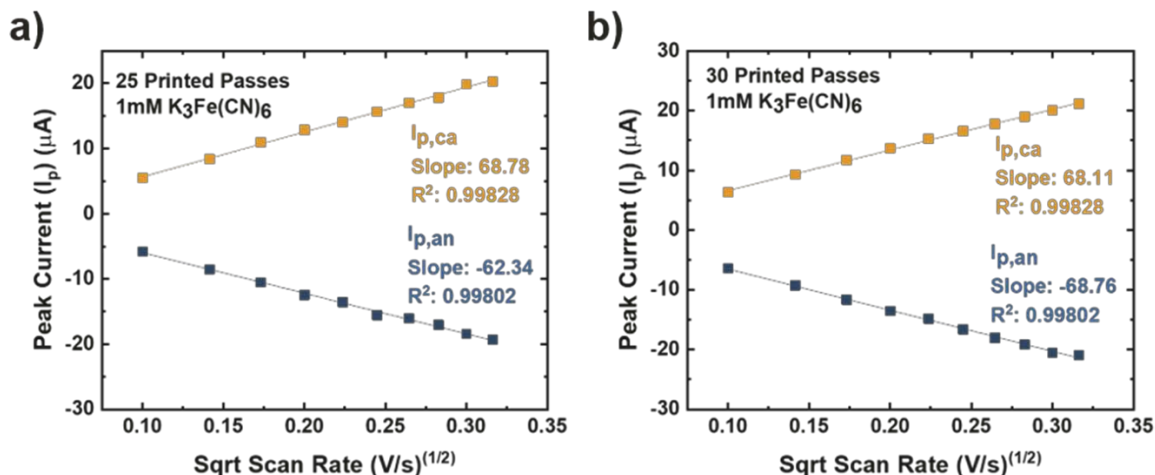


Figure 4.5 Extracted peak current (I_p) versus square root of scan rate (V/s)^{1/2} data from the CV measurements of (a) 25 printed passes and (b) 30 printed passes.

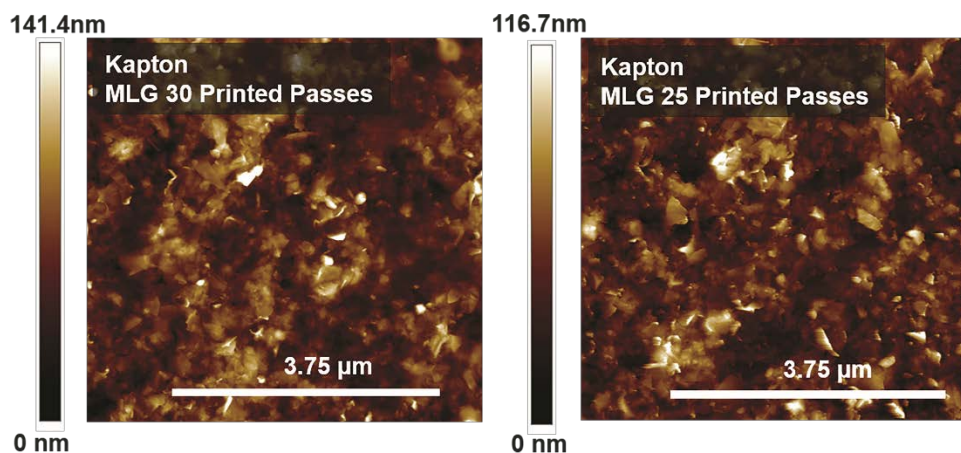


Figure 4.6 AFM scanned image of a) MLG 30 printed passes on Kapton and b) 25 printed passes on Kapton

For further analysis, the cathodic and anodic peak currents (I_{pc} and I_{pa} , respectively) from the CV data were plotted versus the square root of the scan rate (V/s)^{1/2} for both 25 and 30 printed passes (**Figure 4.5 a-b**). The cathodic (I_{pc}) and anodic (I_{pa}) peak currents for 25 and 30 printed passes graphene showed excellent linear

regression, suggesting redox reaction controlled by diffusion. CV simulation was used to extract the diffusion coefficient (**D**) and the rate constant (**k**) from the experimental CV data (**Figures 4.3a-b**). This simulation provided identical CV curves compared to the data for 25 and 30 printed passes, respectively, as seen in **Figures 4.3c-d**. In order to calculate the active surface area, we accounted for surface roughness extracted from the AFM images of 25 printed passes and 30 printed passes (seen in **Figure 4.6**). To compare our data, we also used the Randles - Sevcik equation to calculate the electrochemically active surface area. All the steps for these calculations are presented in the Supplementary Active Surface Area Calculations. The active surface area extracted from AFM images of $\sim 0.086 \text{ cm}^2$ and $\sim 0.084 \text{ cm}^2$ compared to the calculated electrochemically active surface area of $\sim 0.091 \text{ cm}^2$, and $\sim 0.093 \text{ cm}^2$ for 25 printed passes 30 printed passes, respectively, are in good agreement with 0.7% error. Using the calculated electrochemically active surface area, the diffusion coefficients are $\mathbf{D}=4.17 \times 10^{-6} \text{ cm}^2/\text{s}$ for 25 printed passes and $\mathbf{D} = 6.38 \times 10^{-6} \text{ cm}^2/\text{s}$ for 30 printed passes, respectively. Our calculated diffusion coefficient values are comparable with the ferric/ferrocyanide electrolyte reported in Konopka and McDuffie *et al.*.⁶² Furthermore, the average electron transfer rate constants, (25 printed passes) $\mathbf{k} = 1.125 \times 10^{-2} \text{ cm/s}$ with an average double-layer capacitance of $43.4 \text{ }\mu\text{F}$ and (30 printed passes) $\mathbf{k} = 7.34 \times 10^{-3} \text{ cm/s}$ with an average double-layer capacitance of $45.5 \text{ }\mu\text{F}$, where $\alpha = 0.5$ (shows symmetric free energy curve, where the influence of applied voltage at transition state is about mid-way between reactants and products).⁶³

To compare our extracted rate constant (**k**), we used the dimensionless kinetic parameter equation to estimate the heterogenous standard rate constant (**k₀**).⁶⁴

$$\varphi = (-0.6288 + 0.0021x)/(1 - 0.017x)$$

where the peak potential separation is (x), multiplied by the number of electrons involved in the reaction (n), with ferricyanide redox system is equal to one. The rate constant (k_0) is then calculated using the equation

$$\varphi = k_0 \left(\pi D v n \left(\frac{F}{RT} \right) \right)^{\frac{1}{2}}$$

where D is the diffusion coefficient of the redox mediator (potassium ferricyanide is about 4.17×10^{-6} cm²/s), v is the scan rate (10 mV/s), F is the Faraday constant, R is the gas constant, and T is the temperature (25°C). The k_0 of MLG was calculated as 2.38×10^{-2} cm/s close to our extracted value of $k = 1.125 \times 10^{-2}$ cm/s.

Furthermore, we conducted CV with ferrocene methanol (C₁₁H₁₂FeO), an outer sphere redox species, which is not sensitive to surface oxides and only depended on the density of states.⁶⁵⁻⁶⁷ Unlike [Fe(CN)₆]^{-3/-4}, which is an inner sphere redox system that is sensitive to surface. From the CV scans in **Figure 4.7**, we see that the peak separation remains close to 65mV at a scan rate of 10mV/s similar, suggesting the quasi-reversible electrode kinetics. Our MLG demonstrates a good electrochemical response due to many edge sites available on the surface of the electrodes.

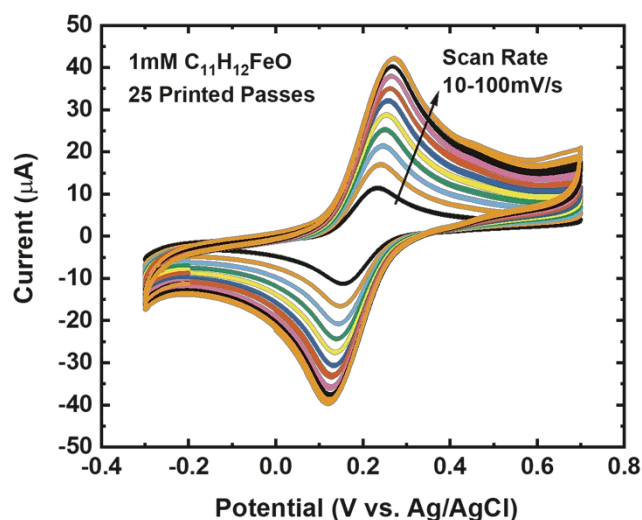


Figure 4.7 Graphene electrode cyclic voltammetry (CV) scan rate data for 1 mM $C_{11}H_{12}FeO$ in 1M KCl as the supporting electrolyte with increasing scan rate 10mV/s-100mV/s for 25 printed passes of graphene.

This suggests that 25 printed passes of MLG has slightly faster electron transfer kinetics than 30 printed passes, likely due to a higher surface roughness of 25 printed passes extracted from the AFM images in the (**Figure 4.6a, b**). This electron transfer rate ($k = 1.125 \times 10^{-2}$ cm/s) is close to or better than that of graphite, graphene oxide, mechanically exfoliated graphene, and screen-printed carbon or graphene or CNT electrode, which range from 10^{-4} cm/s – 10^{-2} cm/s for the ferric/ferrocyanide redox reaction.^{5,68-73}

Cross-sectional TEM was used to image the porosity of the printed MLG electrodes (25 printed passes and 30 printed passes) on untreated Kapton substrates and better understand the structure of IJP deposited MLG. From the cross-sectional TEM images seen in **Figures 4.3e-f**, it is evident that the 25 printed passes (**Figure 4.3e**) IJP MLG sheets are less dense than the 30 printed passes of MLG (**Figure 4.3f**). It is seen that 25 printed passes of graphene exhibit a higher disordered stacking than the 30 printed

pass case. A higher porosity between the stacked multilayers of graphene is observed in 25 printed passes of graphene than in the 30 printed passes. Surface porosity and packing morphology play a significant role in electrochemical performance, as established by Punckt *et al.*⁵⁴ Moreover, using our CV data with varying scan rate (ν), we can obtain the values of max current at $\nu = 10\text{mV/s}$ and $\nu = 100\text{mV/s}$ and calculate the porosity (P)

according to the equation, $P = k \times \frac{I_{max}(\nu=100\frac{\text{mV}}{\text{s}})}{I_{max}(\nu=10\frac{\text{mV}}{\text{s}})}$ $k = \frac{\sqrt{10}}{\sqrt{100}}$. For an ideal planar

electrode, $P = 1$ since then $I_{max} \sim (\nu)^{1/2}$. We find that for our IJP MLG electrodes, $P = 1.17$ for 25 printed passes and $P = 1.06$ for 30 printed passes. This suggests that 25 printed passes show more porosity than 30 printed passes, further supporting our hypothesis that enhanced electrocatalytic behavior is influenced by packing morphology in our printed graphene electrodes⁷⁴

4.3.3 Stability of MLG Electrodes

It is important that these electrodes are inherently stable in the electrolyte and can be reproduced via the printing methods, to enable biosensor design, optimization, and efficient collection of data in real-time.⁷⁵ To investigate the stability of our MLG electrodes, CV measurements were carried out for a series of redox mediator couple dilutions between 1 mM to 5 mM $[\text{Fe}(\text{CN})_6]^{-3/4}$ with 1 M KCl as the supporting electrolyte. Scans were performed at room temperature for 25 (**Figure 4.8a-c**) and 30 (**Figure 4.8d-e**) printed passes with varying scan rate of 10 mV/s (**Figure 4.8a,d**), 50 mV/s (**Figure 4.8b,e**), and 100 mV/s (**Figure 4.8c,f**). We observed that 25 printed passes showed a lower peak to peak separation for all three scan rates in each dilution as compared to 30 printed passes of MLG. Additionally, time-dependent effects were investigated by recording the CV curves at 100 mV/s every 5 min in the same electrolyte

for up to 2 hours, similar to the study of Patel *et al.* .⁷⁶ These studies were carried out with 25 printed passes of MLG electrode in 1 mM ferric/ferrocyanide solution. **Figure 4.9a** shows great stability with negligible change in the peak to peak potential separation, even after 16 hours in the electrolyte.

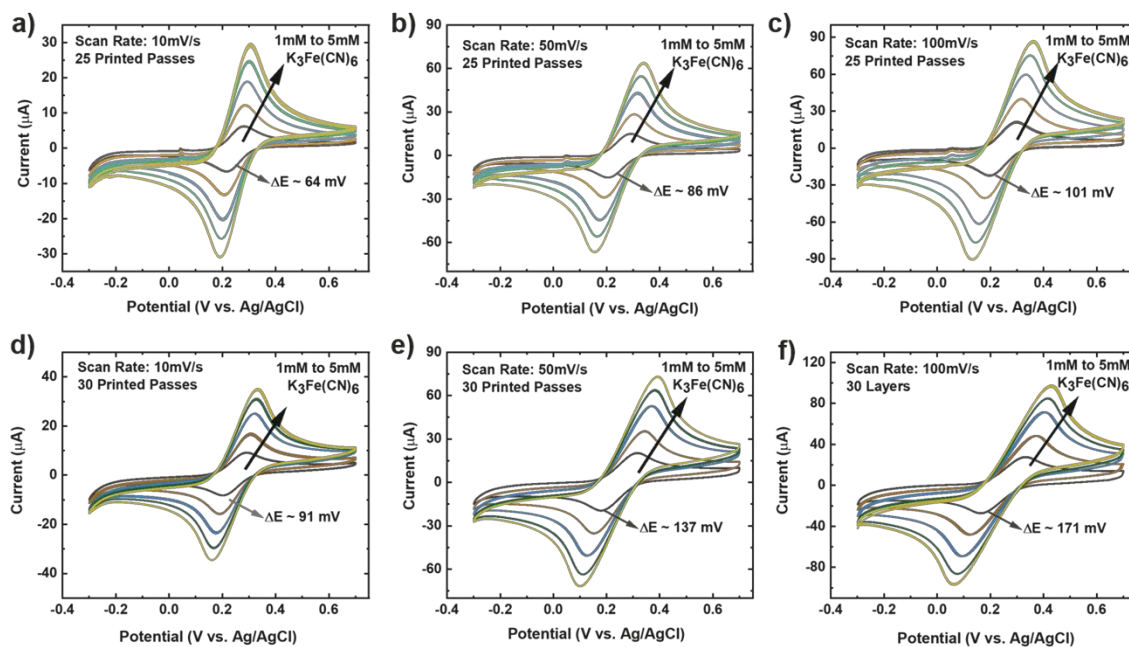


Figure 4.8 Graphene electrode CV dilution data for 1 mM - 5 mM $[\text{Fe}(\text{CN})_6]^{3-/4-}$ in 1M KCl as the supporting electrolyte for 25 printed passes at scan rates of a) 10mV/s, b) 50mV/s, and c) 100mV/s. d-f) are corresponding data for 30 printed passes, with scan rates of d) 10mV/s, e) 50mV/s, and f) 100mV/s.

The reproducibility of the MLG electrodes is demonstrated via the CV scans seen in **Figure 4.9b**, showing a triplicate study with equivalent ink, printing, and other experimental and measurement conditions. The CV scans show consistent and reproducible results for all three electrodes, with a mean peak to peak potential separations of 64 ± 1 mV. To understand the sensing range of the MLG electrode, CV measurements were performed with varying concentrations of ferric/ferrocyanide solution from 10 mM to 1 μM . The bare MLG flexible electrode exhibits a broad sensing

range from 10 mM down to 0.01 mM (**Figure 4.9c**), which is comparable to the sensing range for non-flexible, modified graphene, reduced graphene oxide, or CNT electrodes shown in **Table 4.2** and reported in the literature.^{8,9,11,77–84}

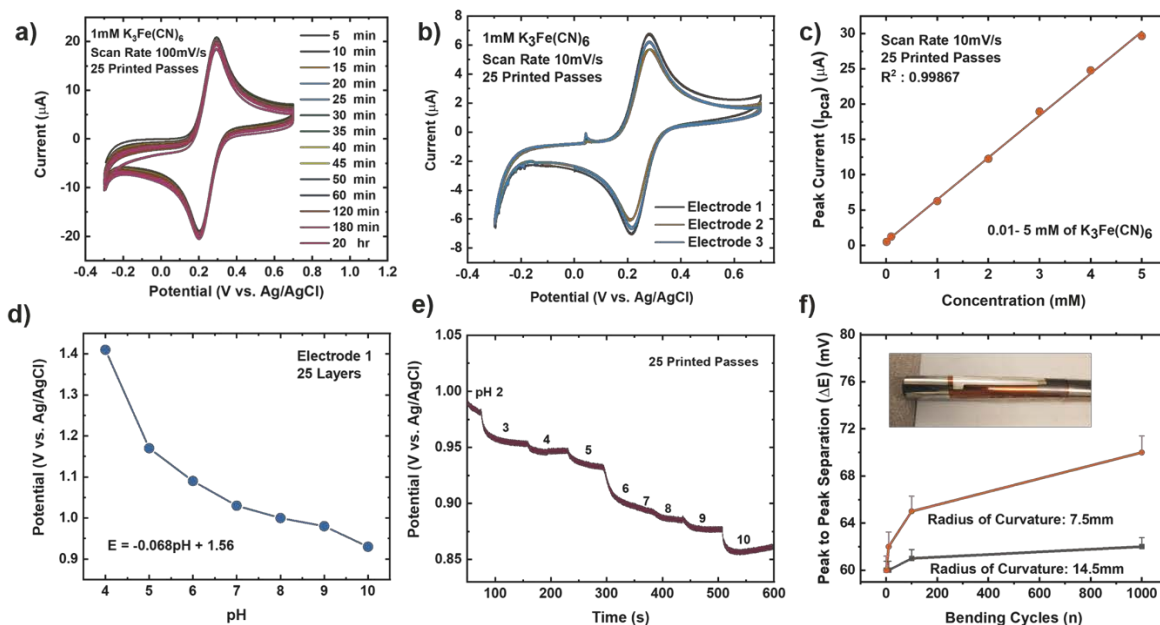


Figure 4.9 a) Time-dependent CV scans for 25 IJP printed passes, 1mM $\text{K}_3\text{Fe}(\text{CN})_6$ in 1 M KCl as the supporting electrolyte at a scan rate of 100mV/s. b) CV repeatability data for 25 IJP printed passes (3 graphene electrodes), 1 mM dilution $[\text{Fe}(\text{CN})_6]^{-3/4}$ in 1 M KCl as the supporting electrolyte at a scan rate of 10 mV/s. c) CV dilution data showing peak current (I_{pca}) vs. concentration from 5 mM to 0.01 mM of $[\text{Fe}(\text{CN})_6]^{-3/4}$ in 1 M KCl as the supporting electrolyte for 25 IJP printed passes, one graphene electrode at scan rate from 10mV/s. d) Static linear pH data vs. potential (potassium phosphate monobasic with sodium hydroxide commercial pH buffer solutions: 4-10 pH) using the 25 passes graphene printed electrode. Error bars represents the interelectrode standard variation in slope compared to the theoretical values based on the Nernst equation.^{94–96} e) Time vs. potential data with changing pH from 2 to 10 for a single 25 printed passes graphene electrode. The error bar represents the standard deviation of potential across three independent samples. f) Bending cycles (1, 10, 100, and 1000) conducted on the electrodes with radius of curvature either 7.5 mm (orange) or 14.5 mm (black) vs. peak to peak separation potential.

4.3.4 pH Sensitivity of MLG Electrodes

The pH of a system is critical to chemical/biological/biochemical processes.^{78,80,85,86} It is also an essential factor for accurately determining the stability and sensitivity of a biosensor as biochemical reactions that take place on the sensor are highly dependent on pH. Potentiometric pH sensors can extract information about pH values by measuring the open circuit potentials.¹¹ For this study, pH sensitivity experiments were conducted on bare MLG electrodes to observe the potentiometric response of the electrode as the pH was varied in the range of 1-10. First, static pH data were acquired using commercially available potassium phosphate monobasic with sodium hydroxide pH buffer solutions (pH 1, 4, 7, and 10) on bare 25 printed passes of MLG printed electrode. Solutions with pH values of 2, 3, 5, 6, 8, and 9 were then formulated by mixing the high pH standard solution with low pH solutions. The pH of the buffer solutions was confirmed using a glass-electrode benchtop pH meter (Mettler-Toledo, Columbus, OH) in a stirred solution. Chronopotentiometry measurements were performed with the printed MLG electrodes while varying the pH buffer solution.

The open circuit potential values were captured for different pH solutions for a 120 second duration. Since the MLG electrode electrochemical process is reversible, the Nernst equation for pH calculation from open circuit potentials is as follows, $E = E_0 - \frac{RT}{nF} \ln(Q)$, where for an ideal electrode, $E = E^{\circ} + 0.0591 \text{ pH}$, with E the measured open circuit potential and E° the standard potential, R the gas constant ($8.314 \text{ J K}^{-1} \text{ mol}^{-1}$), T the absolute temperature (K), n the signed ionic charge and F is the Faraday constant ($96,487.3415 \text{ C mol}^{-1}$).⁸⁷ The equation of the fitted line (pH values 4-10) is as follows: $E = 1.56 - 0.051 \text{ pH}$, where the slope of 51 mV/pH is close to that of an ideal electrode

(i.e., 59 mV/pH) seen in **Figure 4.9d**. To examine the reproducibility of the MLG electrodes, the pH experiment was conducted on three different 25 print pass electrodes fabricated with identical print conditions as described above. **Figure 4.10** displays the potential (MLG vs. Ag/AgCl) versus pH data for all three electrodes. Additionally, from **Figure 4.10**, it can be determined that the MLG electrodes are capable of providing a consistent response with potential (V vs. Ag/AgCl). Furthermore, we employed a response time experiment of our electrode with changing pH values. We started by measuring pH 2 buffer solution and added aliquots (100 μ L to 1mL) of pH 10 buffer solution to change the pH of the solution tested from 2 to 10 and recorded the change in the open circuit potential. The solution tested was stirred between measurements with a magnetic stirrer placed under the cell. **Figure 4.9e** displays the change in potential with the pH of the solution. This suggests that the IJP of bare MLG on a Kapton substrate showed a significant response to the change in pH in the solution.

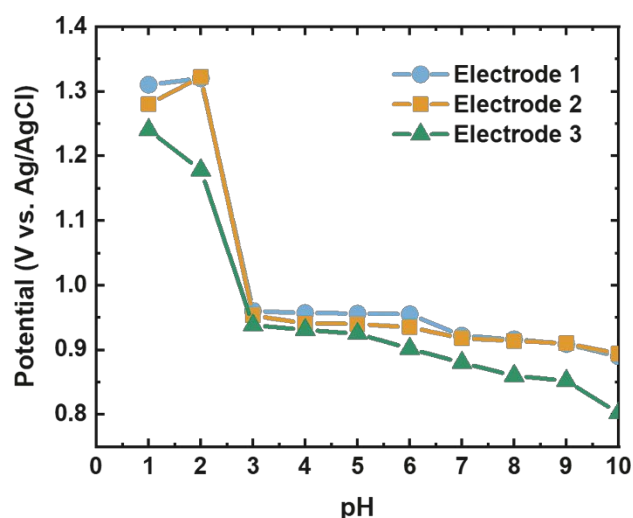


Figure 4.10 Static linear pH data vs. potential (potassium phosphate monobasic with sodium hydroxide commercial pH buffer solutions: 1-10 pH) using the 3 identical 25 passes graphene printed electrodes

Using the separate solutions methods (SSM) with different interfering ions of K^+ , Na^+ , and NH^{4+} (pH 6) to estimate the potentiometric selectivity coefficients K_{IJ}^{pot} at different ion concentration ($10^{-2}M$), where K is the selectivity coefficient, I is the primary ion, and J is the interfering ion.^{88,89} Equation is as follows:

$$K_{IJ}^{pot} = a_I / (a_J)^{z_I/z_J}$$

where a is the activity of the ion and z is the sign or the magnitude for the corresponding charge of the ion. For good selectivity of H^+ ions over the cations, the K value is <1 .

Table 4.1 shows the selectivity coefficient for MLG sensor. The result does show that MLG has good ion selectivity compared to literature.^{90,91}

Table 4.1 SSM for Calculating Selectivity Coefficients of MLG sensors (H^+ ions against interfering ions)

Ions (J)	Log $K_{I,J}^{pot}$	$K_{I,J}^{pot}$
Na^+	-5.34	4.52E-06
K^+	-4.48	3.32E-05
NH^{4+}	-6.87	1.34E-07

To investigate the flexibility of the IJP MLG electrodes, bending cycle testing (n = number of bending cycles) was performed on five IJP printed MLG electrodes fabricated with identical printing conditions (25 printed passes), and having similar resistance measurements. Bending cycles were performed with 7.5 mm and 14.5 mm radius of curvature tubes, and tests were performed from $n = 1$ to 1000, with CV measurements performed at $n = 10$ intervals, as shown in the images in **Figure 4.9f**. Bending is expected to increase the resistance of the electrodes, which should increase the peak to peak separation. **Figure 4.9f** shows that the IJP MLG electrodes show a robust performance over this range of bend cycle testing. Additionally, bending cycles resulted in a ~2% increase peak-to-peak separation with a 14.5 mm radius of curvature

and an ~10% increase in peak-to-peak separation with a 7.5 mm radius of curvature at $n=1000$. A summary of flexible, graphene-based sensors is listed in **Table 4.2**. Electrodes shaded in pink shows functionality of a fully printed three-electrode sensor system; however only our study show functionality of bare graphene electrodes with inkjet-printed Pt counter electrodes. To the best of our knowledge, this is the first study amongst all other flexible, graphene-based sensors, to report on and demonstrate the stability of these types of sensors subjected to cyclic bending tests.

Table 4.2 Comparison of the Ψ (kinetic parameter) of different material- and fabrication-based electrodes

Fully Printed Three-Electrode Sensor System (shaded in pink)							
Electrode Material	Fabrication Technique	Substrate	Electrolyte	Redox Couple	Scan Rate (mV/s)	Ψ Ep Δ (59-200 mV)	Ref.
Multi-layered Graphene	Inkjet-Printed	Kapton (polyimide)	1M KCl	Fe(CN) ₆ ^{3-/4-} (1mM)	10	25.14	This work
Reduced Graphene Oxide	Laser-Scribed	PET	1M KCl	Fe(CN) ₆ ^{3-/4-} (1mM)	10	25.14	66
COOH-terminated Graphene Nanoflakes	Coated	Boron Doped Dimond	0.1M KH ₂ PO ₄	Fe(CN) ₆ ^{3-/4-} (0.5mM)	50	2.54	97
Reduced Graphene Oxide	Coated	Glassy Carbon Electrode	0.1M KCl	Fe(CN) ₆ ^{3-/4-} (5mM)	30	2.54	98
Gold	Inkjet-Printed	Kapton (polyimide)	100mM KCl	Fe(CN) ₆ ^{3-/4-} (1mM)	100	1.71	99
Reduced Graphene Oxide	Screen-Printed	Poly(vinyl chloride)	0.1M KCl	Fe(CN) ₆ ^{3-/4-} (5mM)	50	1.61	15
Edge-Oxidized Graphene Nanosheet	Inkjet-Printed	Kapton (polyimide)	0.1M KNO ₃	Fe(CN) ₆ ^{3-/4-} (2mM)	50	1.61	100
			0.1M KCl		100	1.29	101

Carbon Nanotubes	Inkjet-Printed	Kapton (polyimide)		FcMeOH (4mM)			
CNT	Inkjet-Printed	PET	0.1M KNO ₃	FcMeOH (2mM)	25	1.28	102
Gold	Inkjet-Printed	Paper	3 M KCl	Fe(CN) ₆ ^{3-/4-} (3mM)	20	0.75	103
Graphite	Screen Printed	Ultra-flexible Polyester Materials	0.1M KCl	Fe(CN) ₆ ^{3-/4-} (1mM)	10	0.60	104
Reduced Graphene Oxide	Inkjet-Printed	FTO (Fluorine-doped tin oxide) TEC-15	0.1 M TBAPF ₆	Co(bpy) ₃ (B(CN) ₄) ₃ (1mM)	50	0.60	105
Graphene-PEDOT:PSS	Inkjet-Printed	Screen-Printed Carbon Electrode/ Non-Conformal	0.1M KCl	Fe(CN) ₆ ^{3-/4-} (0.36μM)	100	0.33	106
Functionalized Graphene Nanoribbons	Screen-Printed	Polyethylene glycol terephthalate	0.2M PBS	Fe(CN) ₆ ^{3-/4-} (1mM)	100	0.20	107
Graphene-Polyaniline	Inkjet-Printed	PET	0.1M KCl	Fe(CN) ₆ ^{3-/4-} (1mM)	100	0.20	108
Graphite Pencil	Drawn	Paper	0.1 M KCl	Fe(CN) ₆ ^{3-/4-} (1mM)	100	0.10	109
Graphene with	Inkjet Mask-less	Screen-Printed	1M PBS		10	EpΔ >300	110

platinum (laser annealed)	Lithography	Carbon Electrode/ Non-Conformal Substrate		$\text{Fe}(\text{CN})_6^{3-/4-}$ (5mM)		(mV vs. Ag/AgCl)	
Reduced Graphene/Poly(lactic Acid)	3D-Printed	—	0.1M KCl	$\text{Fe}(\text{CN})_6^{3-/4-}$ (1mM)	100	~500 (mV vs. Ag/AgCl)	111
Reduced Graphene Oxide	Inkjet-Printed/Laser Sintered	Cellulose-based Paper	1M KCl	$\text{Fe}(\text{CN})_6^{3-/4-}$	10	~0.7 (V vs. Ag/AgCl)	112
Reduced Graphene oxide	Inkjet-Printed	Poly(ethylene 2,6-naphthalate) PEN	0.1 M KCl	$\text{Fe}(\text{CN})_6^{3-/4-}$ (1mM)	10	~400 to 5000 (mV vs. Ag/AgCl)	113
PEDOT:PSS	Inkjet-Printed	Paper	0.1M PBS	FcMeOH (-)	20	~50 (mV vs. Ag/AgCl)	114
Multi-walled nanotubes with silver	Inkjet-Printed	Paper	0.5M KCl	$\text{Fe}(\text{CN})_6^{3-/4-}$ (3mM)	20	~55 (mV vs. Ag/AgCl)	115
Graphite	Screen-Printed	Chromatography paper	0.1 M H_2SO_4	$\text{Fe}(\text{CN})_6^{3-/4-}$ (1mM)	100	~56 (mV vs. Ag/AgCl) after 30 scans	116

4.3.5 Fully Printed Three-Electrode Devices

The studies mentioned above provide insights into the electrochemical performance of individual working IJP MLG electrodes using conventional external reference and counter electrodes. Here we compare the electrochemical performance of fully flexible IJP three-electrode (working, counter, and reference) sensor systems to the individual IJP MLG electrode. Fully IJP flexible electrodes could enable large scale, roll-to-roll level production of such sensors. To fabricate the IJP three-electrode sensor system, custom made polyvinyl pyrrolidone capped Pt nanoparticle (PVP-PtNP) ink (seen inset of **Figure 4.11a**) was prepared to print a counter electrode. The TEM image seen in **Figure 4.11a** shows the PtNP ranging from 5-8 nm. To measure the electrical properties of the printed platinum lines, a 4-point probe (Keithley 4200 SCS, Textronix) measurements were conducted. **Figure 4.11b** shows the calculated resistivity as a function of annealing temperature for 4 print passes. Based on the graph, the lowest resistivity was calculated to be $1.3 \times 10^{-6} \Omega\text{-m}$ for 4 print passes at an annealing temperature of $\sim 425^\circ\text{C}$ which is $\sim 10\times$ greater than bulk platinum ($1.06 \times 10^{-7} \Omega\text{-m}$).⁹² Silver (NovaCentrix), Su8 (PriElex Microchem), NaClO, and a cocktail mixture of PVP(Butvar B-98) ink solutions were used to fabricate the Ag/AgCl/(Na⁺) reference electrode (see Methods section for further details). **Figure 4.11c** displays the fully IJP three-electrode sensor system using MLG as the working electrode, Pt counter electrode and Ag/AgCl/(Na⁺) reference electrode. Su8 ink was used as a passivation layer for the MLG electrode, and Ag/AgCl/(Na⁺) electrode.

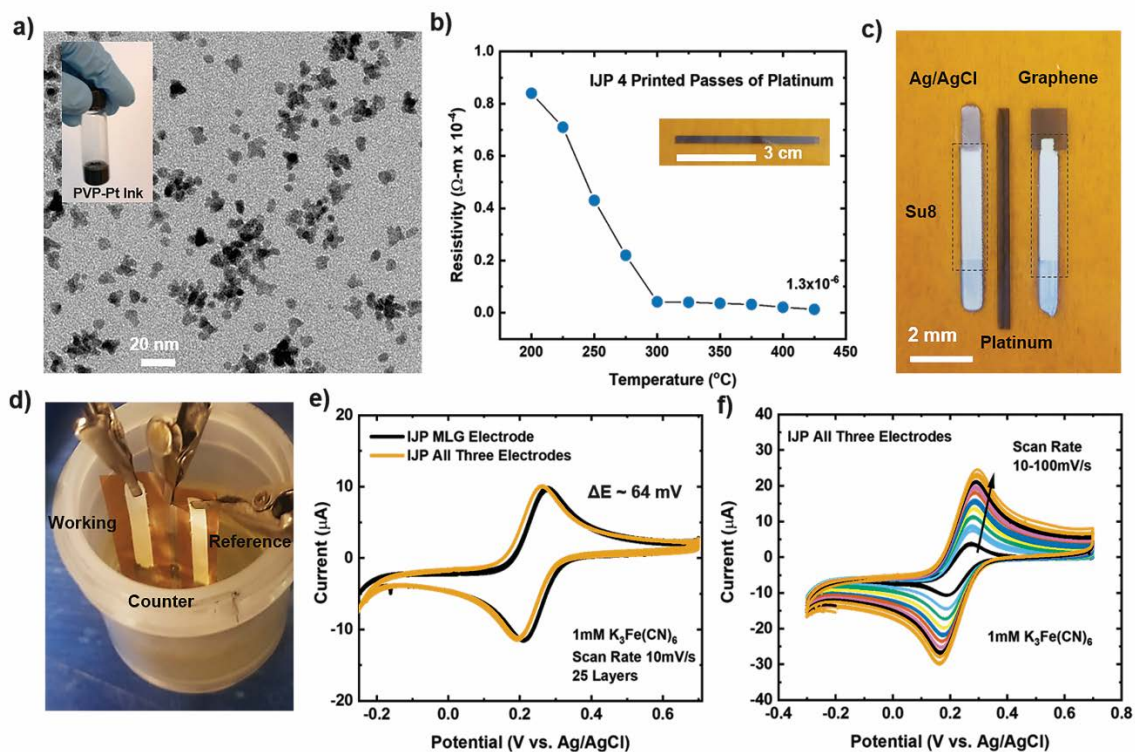


Figure 4.11 a) TEM image of the platinum nanoparticles (PtNP) with an optical image of the platinum ink (inset) b) Resistivity vs. temperature for 4 printed passes of platinum lines on Kapton (inset). c) Optical image of IJP all three electrodes (Ag/AgCl as the reference electrode, platinum as the counter electrode, and MLG as the working electrode). d) optical picture of the electrochemical setup for the fully printed three electrode sensors. e) Cyclic voltammetry (CV) data of IJP MLG (black) compared to all three electrodes (orange) in 1 mM $[\text{Fe}(\text{CN})_6]^{-3/4}$ and 1 M KCl as the supporting electrolyte with scan rate 10mV/s and f) CV scans of all three printed electrodes with increasing scan rate from 10 mV/s-100 mV/s.

The experimental setup shown in **Figure 4.11d** was used to study and compare the electrochemical response of a fully printed three-electrode device to our individual IJP MLG electrode. CV measurements were carried out with a scan rate of 10 mV/s in 1 mM $[\text{Fe}(\text{CN})_6]^{-3/4}$ with 1 M KCl as the supporting electrolyte, for the individual IJP MLG electrode (25 printed passes) and the fully printed three-electrode device. **Figure 4.11e** demonstrates that the response of the fully printed three-electrode devices is comparable to the individual IJP MLG electrodes, and that the three-electrode device exhibits excellent reversibility with a peak to peak separation of ~64mV. Furthermore,

CV measurements were carried out with an increasing scan rate from 10-100 mV/s in 1 mM $[\text{Fe}(\text{CN})_6]^{-3/4}$, as seen in **Figure 4.11f**. Again, CV simulation was used to extract the rate constant (**k**) from the experimental CV data seen in **Figure 4.11f**. The electron rate transfer constant extracted for the fully IJP three-electrode sensors was determined to be $\mathbf{k} = 1.22 \times 10^{-2}$ cm/s for a scan rate of 10mV/s. These CV measurements suggest that the fully printed three-electrode device shows fast electron transfer with this redox system, similar to the results presented for the individual IJP MLG electrodes.

4.4 Conclusion

In this study, the electrochemical behavior of fully inkjet-printed multilayer graphene electrodes on flexible Kapton substrates was investigated. Cyclic voltammetry was used to analyze the electrochemical reversibility of a fully inkjet-printed MLG electrode and a fully inkjet-printed three-electrode device using the ferric/ferrocyanide $[\text{Fe}(\text{CN})_6]^{-3/4}$ redox couple as the analyte. It was confirmed that electrodes optimized at 25 printed passes (with adequate inert edge defects and surface porosity) showed quasi-reversibility with a low peak to peak potential separation of 60 mV and fast electron-transfer kinetics ($\mathbf{k} = 1.125 \times 10^{-2}$ cm/s). Moreover, it was verified that the printed MLG electrode was responsive to varying solution pH and displayed good electrochemical stability even after 1000 bending cycles (7.5 mm radius of curvature) with less than 10% change in peak to peak separation. Cross-sectional TEM images also revealed that the morphology of the printed graphene electrodes enhanced the electrochemical response and behavior of the printed electrodes. These studies indicate that fully IJP three-electrode sensors are a promising approach to fabricating flexible electrodes with an excellent electrochemical response comparable to those reported in the literature. These

electrodes can be produced quickly, easily, and repeatedly, thus showing excellent potential for scalable manufacturing and flexible biosensing applications. The approach reported here enables a deeper understanding of how the combination of ink rheology and additive electronics manufacturing can enable the scalable manufacturing of flexible biosensors for space, military, and commercial applications.

4.5 Methods

4.5.1 Preparation and Characterization of Graphene Ink

Similar to previous work, graphene flakes were obtained by solvent assisted exfoliation of 50 mg/mL graphite powder in a suspension of 2% ethyl cellulose (EC) in ethanol using a Qsonica (Q125) (Newtown, CT) probe tip sonicator for 90 minutes.^{20,53,57,58} To remove the larger graphite flakes, the dispersion was centrifuged (Heraeus™ Megafuge™ 8 Centrifuge TX-150 rotor) at 3402 RCF for 60 min and the supernatant was collected immediately. In a 1:2 volume ratio, the collected supernatant and 0.04 g/mL aqueous solution of NaCl (Sigma-Aldrich, >99.5%) were centrifuged for 30 min at 3402 RCF to facilitate the flocculation of graphene flakes. The resulting graphene/EC dispersion was dried overnight on a PTFE (Teflon) plate. To tailor the concentration and viscosity of ink to be compatible with the Dimatix IJP (Fujifilm, Santa Clara, CA), the dried graphene/EC paper was then dispersed by sonication for 30 min in a mixture of 85% cyclohexanone and 15% terpineol solution, followed by centrifugation at 3402 RCF for 15 min. The resulting ink concentration was 3.5 mg/mL with a viscosity of 8 cP (Wells-Brookfield Cone/Plate Middleboro, MA). The ink concentration was quantified by UV-VIS absorption spectroscopy and Beer-Lamberts law at $\lambda = 600\text{nm}$.

4.5.2 Thermogravimetric Analysis

To determine the annealing temperature of printed graphene features, thermogravimetric analysis (TGA) was employed. A Netzsch STA 449 F1 Jupiter (Burlington, MA) TGA instrument was used to measure the weight percent loss as a function of temperature (25°C to 1000°C) heating rate of 5°C/min in air. TGA analysis revealed the decomposition peak of ethylcellulose is around 250°C, while the other volatile solvent components (cyclohexanone and terpineol) are driven off at 390°C (seen in Figure 4.1e).

4.5.3 Fabrication of MLG Electrodes

The MLG was printed using a Dimatix inkjet printer. The tool platen was heated to 60°C to ensure rapid drying of the ink once deposited on the Kapton HN (Dupont, Wilmington, DE) substrate. A 10 pL cartridge was used to print the MLG. The waveform, jetting voltage, and drop spacing were adjusted to achieve uniform droplets in volume and velocity of the MLG ink. Moreover, 4 nozzles were used to print, and the cartridge was at room temperature. After printing, any remaining ethyl cellulose and solvent was driven out of the lines with a 250°C bake for 30 mins followed by a ramp to a 350°C bake for 45 mins to maximize conductivity of the printed features. Next, NovaCentrix, Metalon (JS-B40G, Austin, TX) silver ink was used to print the contact pad connecting the printed MLG before sintering at 250 °C for 15 mins. Lastly, PriElex Microchem (Westborough, MA) SU-8 ink was printed on top of the silver contact pad connecting the printed MLG. SU-8 acted as a passivation layer to isolate the silver while conducting electrochemical experiments.

4.5.4 Fabrication of Platinum Inks and Platinum Electrodes

98 % sodium tetrahydroborate (Alfa Aesar), 99.999% hexachloroplatinic (IV) acid hydrate (40% platinum metals basis, BeanTown Chemical), 10 kDa polyvinylpyrrolidone (Alfa Aesar), 95-100.5% sodium hydroxide pellets (Macron), ethylene glycol (VWR), $\geq 99.5\%$ carboxymethyl cellulose sodium salt, and 40 kDa MWCO Slide-A-Lyzer Dialysis flasks (Thermo Scientific) were purchased from commercial sources and used without further purification. A 0.58 M hexachloroplatinic acid (H_2PtCl_6) stock solution was prepared with the addition of 5 g of H_2PtCl_6 to 20 mL of nanopure (18 M Ω) water. Additionally, a 2.2 M stock solution of sodium tetrahydroborate (NaBH_4) was prepared with the addition of 0.500 g of NaBH_4 to 6 mL of nanopure (18 M Ω) water buffered to a pH of 12 with NaOH. Both solutions were used without further purification or dilution.

A platinum nanoparticle ink containing ~20 wt.% of 5-8 nm of polyvinyl pyrrolidone capped Pt nanoparticles (PVP-PtNP) suspended in a water/ethylene glycol co-solvent mixture was prepared to be compatible with ink jet printing. The synthesis of PVP stabilized Pt nanoparticles was accomplished through wet chemical methods where 10 mL of stock H_2PtCl_6 solution was added to 1.5L of nano-pure water containing 6g of dissolved PVP. The $\text{H}_2\text{PtCl}_6/\text{H}_2\text{O}/\text{PVP}$ solution was allowed to stir for two hours and was followed by the drop-wise addition of 6 mL of stock NaBH_4 to form PVP-PtNP. The resulting suspension was allowed to stir vigorously for 24 hours, and this process was repeated until a total of 20 g of H_2PtCl_6 had been reduced or 6 L of PVP-PtNP suspension had been synthesized to form ~8 g of PVP capped platinum nanoparticles.

The removal of excess capping agent and reaction by-products was performed through dialysis while utilizing 40 kDa MWCO Slide-A-Lyzer Dialysis flasks. As the dialysis process can be extremely time consuming, the PVP capped Pt nanoparticle suspension was dialyzed against a very high concentration solution of carboxymethyl cellulose in order to accelerate this process. A total of 6 L of PVP-PtNP was concentrated to 50 mL, which was followed by rotary evaporation to further concentrate the suspension to 20 mL. The viscosity of the PVP-PtNP suspension was tuned through the addition of ethylene glycol solution to ensure the ink rheology was compatible with inkjet printing.

The PVP-Pt was printed using a Dimatix inkjet printer. The tool platen was heated to 30°C to ensure rapid drying of the ink once deposited on the Kapton HN (Dupont, Wilmington, DE) substrate. A 10pL cartridge was used to print the PVP-Pt. The waveform, jetting voltage, and drop spacing were adjusted to achieve uniform droplets in volume and velocity of the PVP-Pt ink. Moreover, 2 nozzles were used to print, and the cartridge was at room temperature. After printing, any remaining surfactant and solvent was driven out of the lines with a 150°C bake for 15 mins followed by a ramp to a 400°C bake for 45 mins to maximize conductivity of the printed features.

4.5.5 Fully IJP Three-Electrode Devices

A good method to fabricate fully inkjet printed Ag/AgCl reference electrodes has been described by Moya et. al.⁹³ NovaCentrix, Metalon (JS-B40G, Austin, TX) silver ink was used to print the silver layers on Kapton substrate and then sintered at 250°C for 30 mins. Then, PriElex Microchem (Westborough, MA) SU-8 ink was printed on top of the silver layers for passivation and then sintered 250°C for 50 mins. For chlorination,

diluted NaClO (5 v/v% purchased from Sigma-Aldrich) was printed (2 passes) on the exposed silver and then washed with deionized water. For the formulation of a protecting membrane, a cocktail mixture of PVB (Butvar B-98) (10 w%) in methanol (40%), xylene (30%), diacetone alcohol (15%), and 1-butanol (15%), all purchased from Sigma-Aldrich, was printed (5 passes) on top of the chlorinated area. Lastly, the electrode was left in a fume hood to dry overnight.

4.5.6 Electrochemical Set-up

The electrochemical experiments were conducted using a customized 3D printed cell (**Figure 4.2e**), and potentiostat (BioLogic VMP-300 instrument, Knoxville, TN) with EC-Lab for the software. The 3D printed cell allowed for the printed MLG (working electrode) to be placed on the bottom of the cell, with only 0.07 cm² of the MLG exposed to the solution in the cell. Ag/AgCl was used as a reference electrode and with a platinum mesh as the working electrode. Room temperature cyclic voltammetry (CV) measurements were carried out in a fume hood with an increasing scan rate from 10-100 mV/s, with dilutions ranging from 1 mM to 5mM [Fe(CN)₆]^{-3/4} and 1 M KCl (both purchased from Sigma Aldrich) as the supporting electrolyte. The EC-lab software was used to extract the fitted CV data seen in **Figure 4.3c,d**.

4.6 Acknowledgements

T.P. designed and printed the test structures, and together with C.C., P.B., and J.C. characterized the devices. J.K. and D.E. conceived of the experimental design, and together with H.S and C.X. supervised the experiments. K.F. synthesized the platinum (PVP-Pt) inks. All authors contributed to the development of the manuscript.

4.7 References

- 1 S. Banerjee, J. Shim, J. Rivera, X. Jin, D. Estrada, V. Solovyeva, X. You, J. Pak, E. Pop, N. Aluru and R. Bashir, *ACS Nano*, 2013, **7**, 834–43.
- 2 M. Pumera, A. Ambrosi, A. Bonanni, E. L. K. Chng and H. L. Poh, *TrAC - Trends Anal. Chem.*, 2010, **29**, 954–965.
- 3 A. Ambrosi, C. K. Chua, A. Bonanni and M. Pumera, *Chem. Rev.*, 2014, **114**, 7150–88.
- 4 R. A. W. Dryfe and P. R. Unwin, *J. Electroanal. Chem.*, 2015, 753, 1–2.
- 5 A. T. Valota, I. A. Kinloch, K. S. Novoselov, C. Casiraghi, A. Eckmann, E. W. Hill and R. A. W. Dryfe, *ACS Nano*, , DOI:10.1021/nn202878f.
- 6 L. Huang, Y. Huang, J. Liang, X. Wan and Y. Chen, *Nano Res.*, 2011, **4**, 675–684.
- 7 M. S. Mannoor, H. Tao, J. D. Clayton, A. Sengupta, D. L. Kaplan, R. R. Naik, N. Verma, F. G. Omenetto and M. C. McAlpine, *Nat. Commun.*, 2012, **3**, 763.
- 8 N. Lei, P. Li, W. Xue, J. Xu, J. Xu and J. Xu, *Meas. Sci. Technol.*, , DOI:10.1088/0957-0233/22/10/107002.
- 9 P. K. Ang, W. Chen, A. Thye, S. Wee and K. P. Loh, 2008, **130**, 14392–14393.
- 10 D. Dodoo-Arhin, R. C. T. Howe, G. Hu, Y. Zhang, P. Hiralal, A. Bello, G. Amaratunga and T. Hasan, *Carbon N. Y.*, 2016, **105**, 33–41.
- 11 B. Melai, P. Salvo, N. Calisi, L. Moni, A. Bonini, C. Paoletti, T. Lomonaco, V. Mollica, R. Fuoco and F. Di Francesco, in *Proceedings of the Annual International Conference of the IEEE Engineering in Medicine and Biology Society, EMBS*, 2016, vol. 2016-October, pp. 1898–1901.
- 12 Y. Xu, I. Hennig, D. Freyberg, A. James Strudwick, M. Georg Schwab, T. Weitz and K. Chih-Pei Cha, *J. Power Sources*, 2014, **248**, 483–488.
- 13 M. Zhou, Y. Zhai and S. Dong, *Anal. Chem.*, 2009, **81**, 5603–5613.
- 14 E. P. Randviir, D. A. C. C. Brownson, J. P. Metters, R. O. Kadara and C. E. Banks, *Phys. Chem. Chem. Phys.*, 2014, **16**, 4598–4611.
- 15 J. Ping, J. Wu, Y. Wang and Y. Ying, *Biosens. Bioelectron.*, 2012, **34**, 70–76.
- 16 F.-Y. Kong, S.-X. Gu, W.-W. Li, T.-T. Chen, Q. Xu and W. Wang, *Biosens. Bioelectron.*, 2014, **56**, 77–82.

- 17 C. Sriprachuabwong, C. Karuwan, A. Wisitsorrat, D. Phokharatkul, T. Lomas, P. Sritongkham and A. Tuantranont, *J. Mater. Chem.*, DOI:10.1039/c2jm14005e.
- 18 Y. Shao, J. Wang, H. Wu, J. Liu, I. A. Aksay and Y. Lin, *Electroanalysis*, 2010, **22**, 1027–1036.
- 19 Q. He, S. Wu, Z. Yin and H. Zhang, *Chem. Sci.*, 2012, **3**, 1764.
- 20 E. Jabari and E. Toyserkani, *Carbon N. Y.*, 2015, **91**, 321–329.
- 21 Z. Zhan, J. An, Y. Wei, V. T. Tran, H. Du, X. Niu, Y. Chen, Q. Pei, K. Schierle-Arndt, P. Yang, J.-U. Park, G. Shvets, R. S. Ruoff, S. Krishnamurthy, R. Goodhue, J. Hutchison, V. Scardaci, A. C. Ferrari and J. N. Coleman, *Nanoscale*, 2017, **9**, 965–993.
- 22 M. J. Renn, *WHITEPAPER - Optomec*, 2010, 3–5.
- 23 R. G. Clinton, *NASA's In Space Manufacturing Initiative and Additive Manufacturing Development for Rocket Engine Space Flight Hardware*, 2016.
- 24 F. Torrisci, T. Hasan, W. Wu, Z. Sun, A. Lombardo, T. S. Kulmala, G.-W. W. Hsieh, S. Jung, F. Bonaccorso, P. J. Paul, D. Chu, A. C. Ferrari, H. Tang, D. Liu, Y. Zhao, X. Yang, J. Lu, F. Cui, P. A. Brooksby, A. K. Farquhar, H. M. Dykstra, M. R. Waterland, A. J. Downard, R. Zappacosta, M. Di Giulio, V. Ettore, D. Bosco, C. Hadad, G. Siani, S. Di Bartolomeo, A. Cataldi, L. Cellini, A. Fontana, F. Torrisci, T. Hasan, W. Wu, Z. Sun, A. Lombardo, T. S. Kulmala, G.-W. W. Hsieh, S. Jung, F. Bonaccorso, P. J. Paul, D. Chu, A. C. Ferrari, A. Pattammattel, C. V. Kumar, E. del Corro, L. Kavan, M. Kalbac, O. Frank, T. A. Faculty, S. K. Bidasaria, I. P. Fulfillment, U. Mogera, R. Dhanya, R. Pujar, C. Narayana, G. U. Kulkarni, F. Irin, M. J. Hansen, R. Bari, D. Parviz, S. D. Metzler, S. K. Bhattacharia, M. J. Green, A. a. Green, M. C. Hersam, K. D. Papadimitriou, E. N. Skountzos, S. S. Gkermpoura, I. Polyzos, V. G. Mavrantzas, C. Galiotis, C. Tsitsilianis, H. H. Winter, R. J. T. Nicholl, H. J. Conley, N. V. Lavrik, I. Vlassioux, Y. S. Puzyrev, V. P. Sreenivas, S. T. Pantelides, K. I. Bolotin, J. Yuan, A. Luna, W. Neri, C. Zakri, T. Schilling, A. Colin, P. Poulin, D. Du, P. Li, J. Ouyang, A. M. Dimiev, G. Ceriotti, A. Metzger, N. D. Kim, J. M. Tour, A. N. J. Rodgers, M. Velický and R. A. W. Dryfe, *ACS Nano*, 2012, **6**, 2992–3006.

- 25 Z. P. Yin, Y. a. Huang, N. B. Bu, X. M. Wang and Y. L. Xiong, *Chinese Sci. Bull.*, 2010, **55**, 3383–3407.
- 26 a Sridhar, T. Blaudeck and R. Baumann, *Mater. Matters*, 2009, **6**, 1–8.
- 27 D. McManus, S. Vranic, F. Withers, V. Sanchez-Romaguera, M. Macucci, H. Yang, R. Sorrentino, K. Parvez, S. K. Son, G. Iannaccone, K. Kostarelos, G. Fiori and C. Casiraghi, *Nat. Nanotechnol.*, , DOI:10.1038/nnano.2016.281.
- 28 R. Worsley, L. Pimpolari, D. McManus, N. Ge, R. Ionescu, J. A. Wittkopf, A. Alieva, G. Basso, M. MacUcci, G. Iannaccone, K. S. Novoselov, H. Holder, G. Fiori and C. Casiraghi, *ACS Nano*, , DOI:10.1021/acsnano.8b06464.
- 29 Q. He, S. R. Das, N. T. Garland, D. Jing, J. A. Hondred, A. A. Cargill, S. Ding, C. Karunakaran and J. C. Claussen, *ACS Appl. Mater. Interfaces*, , DOI:10.1021/acсами.7b00092.
- 30 M. Pumera, A. Ambrosi, A. Bonanni, E. L. K. Chng, H. L. Poh, E. Lay, K. Chng, A. Ambrosi, A. Bonanni, E. L. K. Chng and H. L. Poh, *TrAC - Trends Anal. Chem.*, 2010, **29**, 954–965.
- 31 J. L. Richard C. Alkire, Philip N. Bartlett, *Electrochemistry of Carbon Electrodes*, Urbana, Volume 16., 2015.
- 32 D. A. C. Brownson, D. K. Kampouris and C. E. Banks, *Chem. Soc. Rev.*, 2012, **41**, 6944.
- 33 L. L. Zhang and X. S. Zhao, *Chem. Soc. Rev.*, 2009, **38**, 2520.
- 34 H. Choi, H. Kim, S. Hwang, M. Kang, D.-W. Jung and M. Jeon, *Scr. Mater.*, 2011, **64**, 601–604.
- 35 H. Kabir, H. Zhu, J. May, K. Hamal, Y. Kan, T. Williams, E. Echeverria, D. N. McIlroy, D. Estrada, P. H. Davis, T. Pandhi, K. Yocham, K. Higginbotham, A. Clearfield and I. F. Cheng, *Carbon N. Y.*, , DOI:10.1016/j.carbon.2018.12.058.
- 36 L. Wang, Z. Sofer and M. Pumera, *ACS Nano*, 2020, **14**, 21–25.
- 37 F. Du, L. Zhu and L. Dai, in *Biosensors Based on Nanomaterials and Nanodevices*, 2017.
- 38 A. H. Castro Neto, F. Guinea, N. M. R. Peres, K. S. Novoselov and A. K. Geim, *Rev. Mod. Phys.*, 2009, **81**, 109–162.
- 39 A. K. Geim and K. S. Novoselov, *Nat. Mater.*, 2007, **6**, 183–191.

- 40 C. M. Lewandowski, N. Co-investigator and C. M. Lewandowski, *Carbon Nanotube and Graphene Device Physics*, 2015, vol. 1.
- 41 H. Y. Chen, S. Maiti and D. H. Son, *ACS Nano*, 2012, **6**, 583–591.
- 42 D. Estrada, Z. Li, G.-M. Choi, S. N. Dunham, A. Serov, J. Lee, Y. Meng, F. Lian, N. C. Wang, A. Perez, R. T. Haasch, J.-M. Zuo, W. P. King, J. A. Rogers, D. G. Cahill and E. Pop, *npj 2D Mater. Appl.*, , DOI:10.1038/s41699-019-0092-8.
- 43 R. Mas-Ballesté, C. Gómez-Navarro, J. Gómez-Herrero and F. Zamora, *Nanoscale*, 2011, **3**, 20–30.
- 44 K. L. Grosse, V. E. Dorgan, D. Estrada, J. D. Wood, I. Vlassiuk, G. Eres, J. W. Lyding, W. P. King and E. Pop, *Appl. Phys. Lett.*, , DOI:10.1063/1.4896676.
- 45 P. Yasaei, A. Fathizadeh, R. Hantehzadeh, A. K. Majee, A. El-Ghandour, D. Estrada, C. Foster, Z. Aksamija, F. Khalili-Araghi and A. Salehi-Khojin, *Nano Lett.*, , DOI:10.1021/acs.nanolett.5b01100.
- 46 J. C. Koepke, J. D. Wood, D. Estrada, Z. Y. Ong, K. T. He, E. Pop and J. W. Lyding, *ACS Nano*, 2013, **7**, 75–86.
- 47 B. Kumar, K. Min, M. Bashirzadeh, A. B. Farimani, M. H. Bae, D. Estrada, Y. D. Kim, P. Yasaei, Y. D. Park, E. Pop, N. R. Aluru and A. Salehi-Khojin, *Nano Lett.*, 2013, **13**, 1962–1968.
- 48 A. Salehi-Khojin, D. Estrada, K. Y. Lin, K. Ran, R. T. Haasch, J. M. Zuo, E. Pop and R. I. Masel, *Appl. Phys. Lett.*, 2012, 9–12.
- 49 W. Yuan, Y. Zhou, Y. Li, C. Li, H. Peng, J. Zhang, Z. Liu, L. Dai and G. Shi, *Sci. Rep.*, 2013, **3**, 2248.
- 50 N. G. Shang, P. Papakonstantinou, M. McMullan, M. Chu, A. Stamboulis, A. Potenza, S. S. Dhesi and H. Marchetto, *Adv. Funct. Mater.*, , DOI:10.1002/adfm.200800951.
- 51 J. C. Claussen, A. Kumar, D. B. Jaroch, M. H. Khawaja, A. B. Hibbard, D. M. Porterfield and T. S. Fisher, *Adv. Funct. Mater.*, , DOI:10.1002/adfm.201200551.
- 52 L. Tang, Y. Wang, Y. Li, H. Feng, J. Lu and J. Li, *Adv. Funct. Mater.*, , DOI:10.1002/adfm.200900377.

- 53 T. Pandhi, E. Kreit, R. Aga, K. Fujimoto, M. T. Sharbati, S. Khademi, A. N. Chang, F. Xiong, J. Koehne, E. M. Heckman and D. Estrada, *Sci. Rep.*, , DOI:10.1038/s41598-018-29195-y.
- 54 C. Punckt, M. A. Pope and I. A. Aksay, *J. Phys. Chem. C*, , DOI:10.1021/jp405142k.
- 55 K. S. Rao, J. Senthilnathan, Y.-F. F. Liu and M. Yoshimura, *Sci. Rep.*, 2014, **4**, 4237.
- 56 L. G. Cañado, K. Takai, T. Enoki, M. Endo, Y. A. Kim, H. Mizusaki, A. Jorio, L. N. Coelho, R. Magalhães-Paniago and M. A. Pimenta, *Appl. Phys. Lett.*, , DOI:10.1063/1.2196057.
- 57 E. B. Secor, P. L. Prabhumirashi, K. Puntambekar, M. L. Geier and M. C. Hersam, *J. Phys. Chem. Lett.*, 2013, **4**, 1347–1351.
- 58 L. Dybowska-Sarapuk, K. Kielbasinski, A. Arazna, K. Futera, A. Skalski, D. Janczak, M. Sloma and M. Jakubowska, *Nanomaterials*, , DOI:10.3390/nano8080602.
- 59 E. F. Silva, A. A. Tanaka, R. N. Fernandes, R. A. A. Munoz and I. S. da Silva, *Microchem. J.*, 2020, **157**, 105027.
- 60 L. A. J. Silva, W. P. da Silva, J. G. Giuliani, S. C. Canobre, C. D. Garcia, R. A. A. Munoz and E. M. Richter, *Talanta*, 2017, **165**, 33–38.
- 61 D. N. Barreto, M. M. A. C. Ribeiro, J. T. C. Sudo, E. M. Richter, R. A. A. Muñoz and S. G. Silva, *Talanta*, 2020, **217**, 120987.
- 62 S. J. Konopka and B. McDuffie, *Anal. Chem.*, , DOI:10.1021/ac50160a042.
- 63 N. Elgrishi, K. J. Rountree, B. D. McCarthy, E. S. Rountree, T. T. Eisenhart and J. L. Dempsey, *J. Chem. Educ.*, 2018, **95**, 197–206.
- 64 D. A. C. Brownson and C. E. Banks, *The Handbook of Graphene Electrochemistry*, 2014.
- 65 A. S. Ambolikar, S. K. Guin and S. Neogy, *New J. Chem.*, , DOI:10.1039/c9nj04467a.
- 66 K. Griffiths, C. Dale, J. Hedley, M. D. Kowal, R. B. Kaner and N. Keegan, *Nanoscale*, , DOI:10.1039/c4nr04221b.

- 67 E. P. Randviir, D. A. C. Brownson, M. Gómez-Mingot, D. K. Kampouris, J. Iniesta and C. E. Banks, *Nanoscale*, , DOI:10.1039/c2nr31823g.
- 68 J. Yang and S. Gunasekaran, *Carbon N. Y.*, 2012, **51**, 36–44.
- 69 R. O. Kadara, N. Jenkinson and C. E. Banks, *Sensors Actuators, B Chem.*, , DOI:10.1016/j.snb.2009.01.044.
- 70 M. V. Mirkin and A. J. Bard, *Anal. Chem.*, , DOI:10.1021/ac00043a020.
- 71 H. He, Q. Xie, Y. Zhang and S. Yao, *J. Biochem. Biophys. Methods*, , DOI:10.1016/j.jbbm.2004.11.004.
- 72 S. Cinti, F. Arduini, M. Carbone, L. Sansone, I. Cacciotti, D. Moscone and G. Palleschi, *Electroanalysis*, , DOI:10.1002/elan.201500168.
- 73 S. H. Lee, H. Y. Fang, W. C. Chen, H. M. Lin and C. A. Chang, *Anal. Bioanal. Chem.*, , DOI:10.1007/s00216-005-0034-5.
- 74 D. Menshykau and R. G. Compton, *Electroanalysis*, , DOI:10.1002/elan.200804334.
- 75 H. Dong, S. Kyung, H. Chang, K. Roh and J. Choi, *Biosens. Bioelectron.*, 2012, **38**, 184–188.
- 76 A. N. Patel, M. G. Collignon, M. A. OConnell, W. O. Y. Hung, K. McKelvey, J. V. MacPherson and P. R. Unwin, *J. Am. Chem. Soc.*, , DOI:10.1021/ja308615h.
- 77 N. O. Gomes, E. Carrilho, S. A. S. Machado and L. F. Sgobbi, *Electrochim. Acta*, 2020, **349**, 136341.
- 78 P. Salvo, B. Melai, N. Calisi, C. Paoletti, F. Bellagambi, A. Kirchhain, M. G. Trivella, R. Fuoco and F. Di Francesco, *Sensors Actuators, B Chem.*, 2018.
- 79 W. Fu, C. Nef, O. Knopfmacher, A. Tarasov, M. Weiss, M. Calame and C. Schönenberger, *Nano Lett.*, , DOI:10.1021/nl201332c.
- 80 D. Janczak, A. Peplowski, G. Wroblewski, L. Gorski, E. Zwierkowska and M. Jakubowska, *J. Sensors*, 2017, **2017**, 1–6.
- 81 J. G. Giuliani, T. E. Benavidez, G. M. Duran, E. Vinogradova, A. Rios and C. D. Garcia, *J. Electroanal. Chem.*, 2016, **765**, 8–15.
- 82 W. R. de Araujo, C. M. R. Frasson, W. A. Ameku, J. R. Silva, L. Angnes and T. R. L. C. Paixão, *Angew. Chemie Int. Ed.*, 2017, **56**, 15113–15117.

- 83 L. García-Carmona, A. Martín, J. R. Sempionatto, J. R. Moreto, M. C. González, J. Wang and A. Escarpa, *Anal. Chem.*, 2019, **91**, 13883–13891.
- 84 A. A. Dias, C. L. S. Chagas, H. D. A. Silva-Neto, E. O. Lobo-Junior, L. F. Sgobbi, W. R. De Araujo, T. R. L. C. Paixaõ and W. K. T. Coltro, *ACS Appl. Mater. Interfaces*, 2019, **11**, 39484–39492.
- 85 C.-H. Chuang, H.-P. Wu, C. H. C.-H. Chen and P.-R. Wu, *Proc. Int. Conf. Sens. Technol. ICST*, 2011, **5**, 1–13.
- 86 R. Rahimi, M. Ochoa, T. Parupudi, X. Zhao, I. K. Yazdi, M. R. Dokmeci, A. Tamayol, A. Khademhosseini and B. Ziaie, *Sensors Actuators, B Chem.*, 2016, **229**, 609–617.
- 87 Y. Wen, X. Wang, P. Cai and X. Yu, *Sensors Actuators B Chem.*, 2015, **216**, 409–411.
- 88 R. P. Buck and E. Lindner, *Pure Appl. Chem.*, , DOI:10.1351/pac199466122527.
- 89 E. Lindner and Y. Umezawa, *Pure Appl. Chem.*, 2008.
- 90
- 91 J. Ping, Y. Wang, J. Wu and Y. Ying, *Electrochem. commun.*, , DOI:10.1016/j.elecom.2011.10.018.
- 92 D. C. Giancoli, *Phys. Educ.*, , DOI:10.1088/0031-9120/35/5/705.
- 93 A. Moya, R. Pol, A. Martínez-Cuadrado, R. Villa, G. Gabriel and M. Baeza, *Anal. Chem.*, 2019, **91**, 15539–15546.
- 94 G. Chen, S. Xiao, A. Lorke, J. Liu and P. Zhang, *J. Electrochem. Soc.*, , DOI:10.1149/2.0101816jes.
- 95 D. De Venuto, S. Carrara, A. Cavallini and G. De Micheli, in *Proceedings of the 12th International Symposium on Quality Electronic Design, ISQED 2011*, 2011.
- 96 S. Carrara, M. D. Torre, A. Cavallini, D. De Venuto and G. De Micheli, in *2010 IEEE Biomedical Circuits and Systems Conference, BioCAS 2010*, 2010.
- 97 M. M. Lounasvuori, M. Rosillo-Lopez, C. G. Salzmänn, D. J. Caruana and K. B. Holt, *Faraday Discuss.*, , DOI:10.1039/c4fd00034j.

- 98 K. L. S. Castro, S. M. Oliveira, R. V. Curti, J. R. Araújo, L. M. Sassi, C. M. Almeida, E. H. M. Ferreira, B. S. Archanjo, M. F. Cabral, A. Kuznetsov, L. A. Sena, C. A. Achete and E. D'Elia, *Int. J. Electrochem. Sci.*, , DOI:10.20964/2018.01.02.
- 99 G. C. Jensen, C. E. Krause, G. A. Sotzing and J. F. Rusling, *Phys. Chem. Chem. Phys.*, , DOI:10.1039/c0cp01755h.
- 100 B. Nagar, M. Jović, V. C. Bassetto, Y. Zhu, H. Pick, P. Gómez-Romero, A. Merkoçi, H. H. Girault and A. Lesch, *ChemElectroChem*, , DOI:10.1002/celec.201901697.
- 101 A. Lesch, F. Cortés-Salazar, V. Amstutz, P. Tacchini and H. H. Girault, *Anal. Chem.*, , DOI:10.1021/ac503748g.
- 102 A. Lesch, M. Jović, M. Baudoz, Y. Zhu, P. Tacchini, F. Gumy and H. H. Girault, *ECS Trans.*, , DOI:10.1149/07707.0073ecst.
- 103 A. Määttänen, U. Vanamo, P. Ihalainen, P. Pulkkinen, H. Tenhu, J. Bobacka and J. Peltonen, *Sensors Actuators, B Chem.*, , DOI:10.1016/j.snb.2012.10.113.
- 104 C. W. Foster, J. P. Metters, D. K. Kampouris and C. E. Banks, *Electroanalysis*, , DOI:10.1002/elan.201300563.
- 105 R. Martínez-Flores, E. J. Canto-Aguilar, G. Rodríguez-Gattorno, G. Oskam, D. Meneses-Rodríguez and M. A. Ruiz-Gómez, *J. Electrochem. Soc.*, , DOI:10.1149/2.0381905jes.
- 106 C. Sriprachuabwong, C. Karuwan, P. Ditsayut, T. Lomas, P. Sritongkham, A. Tuantranont, A. Wisitsorrat, D. Phokharatkul, T. Lomas, P. Sritongkham, A. Tuantranont, P. Ditsayut, T. Lomas, P. Sritongkham and A. Tuantranont, *J. Mater. Chem.*, 2012, **22**, 5478.
- 107 F. Valentini, D. Romanazzo, M. Carbone and G. Palleschi, *Electroanalysis*, , DOI:10.1002/elan.201100415.
- 108 C. Bardpho, P. Rattanarat, W. Siangproh and O. Chailapakul, *Talanta*, 2016, **148**, 673–679.
- 109 W. Li, D. Qian, Y. Li, N. Bao, H. Gu and C. Yu, *J. Electroanal. Chem.*, , DOI:10.1016/j.jelechem.2016.03.027.

- 110 J. A. Hondred, J. C. Breger, N. J. Alves, S. A. Trammell, S. A. Walper, I. L. Medintz and J. C. Claussen, *ACS Appl. Mater. Interfaces*, 2018, **10**, 11125–11134.
- 111 C. L. Manzanares Palenzuela, F. Novotný, P. Krupička, Z. Sofer and M. Pumera, *Anal. Chem.*, , DOI:10.1021/acs.analchem.8b00083.
- 112 S. R. Das, Q. Nian, A. A. Cargill, J. A. Hondred, S. Ding, M. Saei, G. J. Cheng and J. C. Claussen, *Nanoscale*, , DOI:10.1039/c6nr04310k.
- 113 J. Kudr, L. Zhao, E. P. Nguyen, H. Arola, T. K. Nevanen, V. Adam, O. Zitka and A. Merkoçi, *Biosens. Bioelectron.*, , DOI:10.1016/j.bios.2020.112109.
- 114 E. Bihar, S. Wustoni, A. M. Pappa, K. N. Salama, D. Baran and S. Inal, *npj Flex. Electron.*, , DOI:10.1038/s41528-018-0044-y.
- 115 H. Shamkhalichenar and J.-W. Choi, *J. Electrochem. Soc.*, , DOI:10.1149/2.0161705jes.
- 116 P. J. Lamas-Ardisana, P. Casuso, I. Fernandez-Gauna, G. Martínez-Paredes, E. Jubete, L. Añorga, G. Cabañero and H. J. Grande, *Electrochem. commun.*, , DOI:10.1016/j.elecom.2016.11.015.

CHAPTER FIVE: FUTURE WORK-INTEGRATION OF GRAPHENE ELECTRODES
WITH FLEXIBLE SILICON INTEGRATED CIRCUITS (Flex-ICs) FOR ION
SELECTIVITY STUDY

5.1 Introduction

5.1.1 Flexible Hybrid Electronics

The development of printed electronics has created a new, desired alternative to fabricate cost-effective devices.^{1,2} Multi-functional inks are directly printed on flexible substrates to fabricate devices such as sensors, battery, display, transistors.³⁻⁷ However, these devices are limited in resolution by the materials and printing process. A flexible hybrid platform presents a viable solution to combine cost-effective printed electronics with high performing silicon-based electronics.^{8,9} Hybrid electronics combine soft and hard components; the soft part is the printed circuits, and the hard parts include silicon microchips, power generators, and communication devices. As mentioned earlier in the first chapter, four primary interconnection techniques are widely used: wire bonding, tape automated bonding, anisotropic conductive adhesives (ACA) for flip-chip bonding, and printing for direct bonding to Flex-IC pads.^{10,11} For this project, we are going to be focusing on the direct bonding technique that includes the following four steps (**Figure 5.1**): dispensing a non-conductive adhesive (NCA), placing the components with the contact part facing upward, and curing the NCA, IJP the circuit patterns, as well as the interconnects, and sintering.¹² There are two functions of the NCA, first to secure the hard components in place and create a mechanical bond between the hard components

and the flexible substrate. Second, to form a smooth ramp to IJP, the interconnects between the substrate and the pads on the hard components. This printing process allows one to streamline the assembly process, in turn reducing the packaging cost. The flexible hybrid platform's electrical performance and reliability test compared with other state-of-the-art designs showed high conformability, smaller in size, long battery life, and low cost.^{9,10,13} This platform provides a promising solution for future wearable electronic applications.

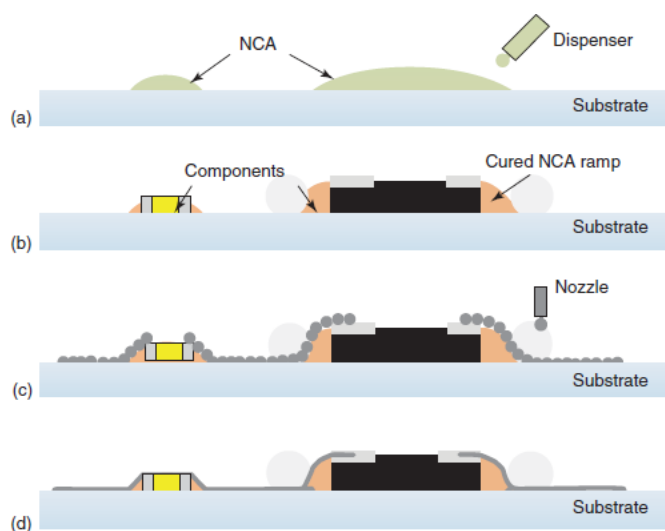


Figure 5.1 Direct Bonding Process

5.1.2 Ion-Selective Electrodes

Ion-selective electrodes (ISEs) are useful in electrochemical sensors for physiological and environmental analysis.^{14–16} Due to their operational simplicity, these are among the most used sensors (a billion tests)¹⁷, making them a reliable testing methodology for ion detection. Conventional coated-wire electrodes were first developed in 1971, comprising a layer of a suitable polymeric matrix substrate containing a dissolved electroactive species, coated on a conducting substrate.¹⁷ The next-generation fabrication method of ion-selective electrodes is with an internal solid contact.^{18,19} The

use of solid contact transducers has dramatically improved the potential stability compared to the coated wire electrodes. Much of the work concerning ionophore-based transduction is dedicated to achieving lower and lower detection limits, especially useful for trace analysis in the micro to the nano-molar range.¹⁷ The extraordinary properties of graphene are derived from the crystal structure, as mentioned in chapter one. They are well suited for electrochemical applications due to their large surface area, high surface electron mobility, and their capacity to promote electron transfer between heterogeneous phases.²⁰ Taking advantage of these characteristics, graphene would be ideal as a backbone structure in potentiometric electrodes to support the ion-selective membrane. This work aims to develop graphene based ISEs for lowering the detection limits and improving selectivity by optimizing materials and flexible hybrid manufacturing techniques.

5.2 Preliminary Results and Discussion

5.2.1 Construction of Ion-Selective Electrodes

A stable reference and counter electrodes are essential to accompany the working electrode part of the ISE. In chapter 4, we observed the electrochemical performance of fully printed graphene-based working electrodes with printed Ag/AgCl reference electrodes and printed platinum counter electrodes. Some common ISEs are based on solid crystalline, glass carbon, glass, ceramic, or liquid membranes²¹. The ion-selective membrane (ISM) comprises a polymer matrix with an organic backbone that remains sufficiently fluid at room temperature. Polyvinyl chloride (PVC) is the most common polymer matrix material due to its low cost, thermal, chemical, and mechanical stability.¹⁹ Moreover, tetrahydrofuran (THF), a common organic solvent, the polymers

are diluted in solution. Another essential component of ISM is the ionophore itself. The analyte inside the ionophore membrane's double layer generates potential due to charge separation of the counter electrode ions in the aqueous phase. For our case, the ion-selective cocktail solution consists of an ionophore, a plasticizer used as a viscous liquid with a glass transition below room temperature. A lipophilic salt exchanger is also needed to increase ionic conductivity and maintain charge neutrality and selectivity of the membrane.

5.2.2 Ion Selective Study

Our Na⁺ selective ion cocktail membrane solution consists of sodium ionophore X, PVC as a polymer, Bis(2-ethylhexyl) sebacate (BEHS) as a plasticizer, and Sodium tetrakis[3,5 bis(trifluoromethyl)phenyl]borate, as a lipophilic salt. K⁺ selective ion cocktail membrane solution consists of a neutral ionophore, valinomycin, which selectively complexes with potassium (K⁺) and potassium tetrakis 4-chlorophenyl borate, a typical salt exchanger, PVC, and BEHS as a plasticizer. Ion-selective membranes were then prepared by drop-casting 10 µl of the Na⁺-selective membrane cocktail and 4 µl of the K⁺-selective membrane cocktail onto IJP printed passes graphene electrodes and dried overnight. The PVC showed good mechanical adhesion to the graphene electrodes.

For the potentiometric performance, we measured the log a_{K⁺} dependence of the new electrodes with ISM coated layers by recording the potential with the standard addition method.²² **Figure 5.2a,b** illustrate the open circuit potentials of Na⁺ sensors in the electrolyte solutions with physiologically relevant concentrations of 10–160 mM Na⁺. The potassium ion activity's linear range is compared to the Nernstian slope sensitivity value of 59 mV/decade a_{K⁺}.

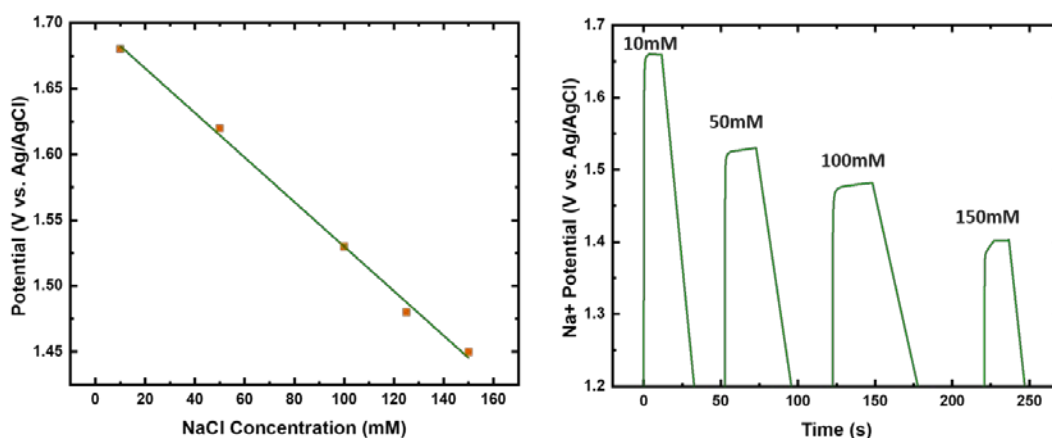


Figure 5.2 Potentiometric Response a) Potential response with varying NaCl concentration and b) timed response of ISM on graphene electrodes

While our Na⁺ selectivity studies correctly demonstrate the Nernstian response for an ideal ion-specific membrane, it does not include the deviation from Nernstian behavior associated with interfering ion complexation, which ultimately gives rise to the detection limit. We hope to incorporate this with K⁺ and other ions to fully predict the response of ion-specific membranes, enabling us to modify parameters or optimize performance.

5.2.3 Ion Selective Electrode Integrated With Flex Hybrid Platform

We will use the flexible hybrid platform to integrate with the printed ion-selective electrode mentioned above for proof-of-concept. The Flex ICs from ASI are needed for analog to digital converters, signal processing, communication, and amplifier requirements.¹¹ The first component we hope to integrate with the printed circuits on the flexible polyamide is the 8-channel analog to digital converter with a die size 2.4 mm by 2.4 mm, a pad opening of 160 μ m by 160 μ m, and chip thickness of 0.06 mm. The resolution of the inkjet printer, in the best-case scenario, is about 25 μ m, an optimal solution for printing on the pad opening of the die. To employ the NCA integration

platform, two ink-substrate-surfaces are involved, the polyamide and the NCA ramp. To optimize the inkjet printing conditions, surface roughness, and surface energy are characterized.

Furthermore, drop spacing and drop size are tailored to achieve optimal line resolution. UV-curing thermoset and thermoplastic NCA can be formulated by tuning the viscosity down to 8-10 cP using a diluting solvent. The die thickness is only about 0.06 mm, so instead of dispensing the NCA onto the polyamide substrate, an adaptation of IJP to precisely deposit discrete droplets of NCA adhesive. A digital and non-contact manner at relatively high speed would be favorable for roll-to-roll manufacturing. Stylus profilometer will be used to characterize the thickness on the NCA printed layers to secure the Flex IC chip in place. Lastly, the silver lines will be printed on the Kapton, NCA ramp, and the pads to integrate the printed ISEs (**Figure 5.3**).

Electrical performance and the bending test will be employed to analyze the stability of the interconnects. Other components, such as the flexible Bluetooth chip, will be integrated using the same NCA process. This study aims to read out the potential with varying concentrations of ionic solutions similar to the data seen in **Figure 5.2**.

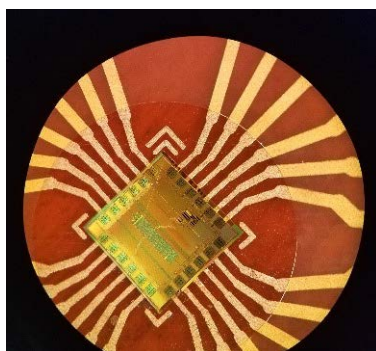


Figure 5.3 Example of Flex ICs with IJP silver interconnects²³.

5.3 Conclusion

The developments of fully printed graphene-based electrodes for ion-selectivity, integrated with a flexible hybrid platform, offers a new possibility for cost-effective manufacturing of large-scale flexible devices. The inkjet printing of silver interconnects on flexible substrates is well suited to streamline the assembly process for such devices. While fully printed devices are still in the early stages, silicon-based electronics efficiently provides high performance and data processing capabilities. The integration of both with a flexible hybrid platform shows great potential for wearable electronics applications. Herein, we investigate our preliminary data on developing a proof-of-concept integrated system for ion selectivity. Further work is needed to observe the stability, selectivity, and sensitivity of the integrated sensor device.

5.4 References

1. Seifert, T. *et al.* Additive manufacturing technologies compared: Morphology of deposits of silver ink using inkjet and aerosol jet printing. *Ind. Eng. Chem. Res.* **54**, 769–779 (2015).
2. Gibson, I., Rosen, D. W. W. D. W. & Stucker, B. *Additive manufacturing technologies: Rapid prototyping to direct digital manufacturing. Additive Manufacturing Technologies: Rapid Prototyping to Direct Digital Manufacturing* **54**, (2010).
3. Cummins, G. & Desmulliez, M. P. Y. Inkjet printing of conductive materials: A review. *Circuit World* (2012). doi:10.1108/03056121211280413
4. McManus, D. *et al.* Water-based and biocompatible 2D crystal inks for all-inkjet-printed heterostructures. *Nat. Nanotechnol.* (2017). doi:10.1038/nnano.2016.281
5. Yang, W. & Wang, C. Graphene and the related conductive inks for flexible electronics. *J. Mater. Chem. C* (2016). doi:10.1039/C6TC01625A

6. Lin, Z. *et al.* Preparation of water-based carbon nanotube inks and application in the inkjet printing of carbon nanotube gas sensors. *J. Electron. Packag. Trans. ASME* (2013). doi:10.1115/1.4023758
7. Worsley, R. *et al.* All-2D Material Inkjet-Printed Capacitors: Toward Fully Printed Integrated Circuits. *ACS Nano* (2019). doi:10.1021/acsnano.8b06464
8. Khan, Y. *et al.* A New Frontier of Printed Electronics: Flexible Hybrid Electronics. *Advanced Materials* (2020). doi:10.1002/adma.201905279
9. Tong, G., Jia, Z. & Chang, J. Flexible Hybrid Electronics: Review and Challenges. in *Proceedings - IEEE International Symposium on Circuits and Systems* (2018). doi:10.1109/ISCAS.2018.8351806
10. Mäntysalo, M. *et al.* System integration of smart packages using printed electronics. in *Proceedings - Electronic Components and Technology Conference* (2012). doi:10.1109/ECTC.2012.6248957
11. FleX-ICs - American Semiconductor, Inc. Available at: <https://www.americansemi.com/flex-ics.html>. (Accessed: 26th September 2020)
12. Zheng, L.-R., Tenhunen, H. & Zou, Z. *Smart Electronic Systems. Smart Electronic Systems* (2018). doi:10.1002/9783527691685
13. Khan, Y. *et al.* Flexible hybrid electronics: direct interfacing of soft and hard electronics for wearable health monitoring. *Adv. Funct. Mater.* **26**, 8764–8775 (2016).
14. Salvo, P. *et al.* Graphene-based devices for measuring pH. *Sensors and Actuators, B: Chemical* (2018). doi:10.1016/j.snb.2017.10.037
15. Maccà, C. Response time of ion-selective electrodes: Current usage versus IUPAC recommendations. *Analytica Chimica Acta* (2004). doi:10.1016/j.aca.2004.03.010
16. Buck, R. P. & Lindner, E. Recommendations for nomenclature of ion-selective electrodes (IUPAC recommendations 1994). *Pure Appl. Chem.* (1994). doi:10.1351/pac199466122527
17. Pretsch, E. The new wave of ion-selective electrodes. *TrAC - Trends Anal. Chem.* (2007). doi:10.1016/j.trac.2006.10.006

18. Bobacka, J. Conducting polymer-based solid-state ion-selective electrodes. *Electroanalysis* (2006). doi:10.1002/elan.200503384
19. Dimeski, G., Badrick, T. & John, A. S. Ion Selective Electrodes (ISEs) and interferences-A review. *Clinica Chimica Acta* (2010). doi:10.1016/j.cca.2009.12.005
20. He, Q. *et al.* Enabling Inkjet Printed Graphene for Ion Selective Electrodes with Postprint Thermal Annealing. *ACS Appl. Mater. Interfaces* (2017). doi:10.1021/acsami.7b00092
21. Pungor, E., Tóth, K. & Nagy, G. Ion-Selective Electrodes. *Mikrochim. Acta* (1978). doi:10.1007/BF01201607
22. Sriprachuabwong, C. *et al.* Enhancing electrochemical sensitivity of screen printed carbon electrode by inkjet printed graphene-PEDOT/PSS Layers. in *ECTI-CON 2011 - 8th Electrical Engineering/ Electronics, Computer, Telecommunications and Information Technology (ECTI) Association of Thailand - Conference 2011* 54–57 (2011). doi:10.1109/ECTICON.2011.5947769
23. Rodriguez, A., Estrada, D., Subbaraman, H. & Wilson, D. Anisotropic Conductive Adhesives on Flexible Hybrid Electronics. *Idaho Conf. Undergrad. Res.* (2018).

CHAPTER SIX: SUMMARY

This dissertation focuses on developing printed graphene-based devices by optimizing the ink rheology, observing surface morphology, and tuning additive manufacturing printing parameters. For its unique electrical and mechanical properties, graphene material was chosen, and the additive manufacturing printing process was employed and characterized. A highly concentrated graphene ink was developed and adapted for AJP and IJP to print reliable and repeatable graphene patterns on varying substrates. We optimized our graphene printed patterns by tuning the AJP and IJP printing parameters, pre-and-post substrate modification, and sintering/annealing conditions, characterized by height profiles, electrical conductance, sheet resistance, and surface morphology with varying printed passes.

First, we used the AJP process to print graphene interconnects on three different substrates with different thermal conductivities to study the power dissipation and electrical breakdown. Our studies indicate that power dissipation in AJP graphene is dominated by the graphene interconnect morphology for high thermal conductivity substrates. They can be limited by the substrate properties in low thermal conductivity polymer substrates typically used for flexible and wearable electronics applications. Further studies are needed to investigate the high thermal resistance of the graphene interconnects, which is likely due to several factors: the porosity of the printed interconnects and the high thermal resistance between graphene layers disorder of the constituent graphene nanoflakes that make up the interconnect.

Second, we used the IJP process to print graphene electrodes on flexible polyamide to study the electrochemical performance. Our graphene electrodes are bare without functionalization or adding conductive polymers or metal particles, yet they still outperform nearly all other similar reports in the literature. The cyclic voltammetry measurements proved that electrodes with 25 IJP printed passes of MLG exhibit excellent kinetics compared to other carbon-based materials. Furthermore, we report cyclical bending tests for full inkjet-printed graphene electrochemical sensors. After 1000 bend cycles, we noticed a negligible change in the peak to peak separation for a 14.5 mm radius of curvature and an ~10% change for a 7.5mm radius of curvature. Moreover, we developed a platinum nanoparticle-based ink compatible with inkjet printing and show that a full printed 3-electrode system performs as well as our full inkjet-printed graphene working electrode with bulk reference and counter electrodes

Lastly, developing a sensor's proof-of-concept with Flex ICs integrates with the printed ion-selective electrode using the NCA process. Inkjet printing of the NCA and the silver interconnects would allow us to streamline the process optimal for roll-to-roll manufacturing of flexible hybrid sensors. Further work is needed to investigate the electrical and bending stability of the sensor.